

Unclassified

SECURITY CLASSIFICATION OF THIS PAGE

AD-A274 967

Form Approved  
OMB No. 0704-0188

REPORT C			
1a. REPORT SECURITY CLASSIFICATION Unclassified		3. DISTRIBUTION/AVAILABILITY OF REPORT Approved for public release; Distribution unlimited	
2a. SECURITY CLASSIFICATION AUTHORITY ELECTE IAN 27 1994		5. MONITORING ORGANIZATION REPORT NUMBER(S) AFOSR-TR- 5	
2b. DECLASSIFICATION/DOWNGRADING SCHEDULE		6a. NAME OF PERFORMING ORGANIZATION University of Oslo	
4. PERFORMING ORGANIZATION REPORT NUMBER A		6b. OFFICE SYMBOL (if applicable)	
6c. ADDRESS (City, State, and ZIP Code) Faculty of Science, P0 Box 1032 Blindern N-0316 OSLO, NORWAY		7a. NAME OF MONITORING ORGANIZATION Air Force Office of Scientific Research	
8a. NAME OF FUNDING/SPONSORING ORGANIZATION AFOSR		8b. OFFICE SYMBOL (if applicable) NL	
8c. ADDRESS (City, State, and ZIP Code) Building 410 Bolling AFB D C 20332-6448		9. PROCUREMENT INSTRUMENT IDENTIFICATION NUMBER F49620-92-J-0510	
10. SOURCE OF FUNDING NUMBERS			
PROGRAM ELEMENT NO.	PROJECT NO.	TASK NO.	WORK UNIT ACCESSION NO.
6 1102F	2309	AS	
11. TITLE (Include Security Classification) Eurasian Seismic Surveillance - 2D FD Seismic Synthetics and Event Discrimination			
12. PERSONAL AUTHOR(S) Bent O. Ruud, Eystein S. Husebye			
13a. TYPE OF REPORT First Annual Technical	13b. TIME COVERED FROM 1 Oct 92 TO 30 Sep 93	14. DATE OF REPORT (Year, Month, Day) 1993 December 22	15. PAGE COUNT
16. SUPPLEMENTARY NOTATION			
17. COSATI CODES		18. SUBJECT TERMS (Continue on reverse if necessary and identify by block number) Seismic event classification, Real-time magnitude estimation, Crustal structure of Iberia, 2D FD synthetics including topography, Fennoscandian seismicity	
19. ABSTRACT (Continue on reverse if necessary and identify by block number) In addition to the paper included in the First Scientific Report submitted to AFOSR (19. May 1993) two other studies have been completed in the reporting period. The first of these (Tavainen and Husebye, 1994) deals with spatial and temporal patterns in Fennoscandian seismicity essentially amounting to an exercise in monitoring mining and other explosions. We demonstrate that there exist a very consistent diurnal/weekly and spatial patterns for the numerous explosion events included in local seismological bulletins. The other study (Hestholm and Ruud, 1994) presents a numerical 2D finite difference (FD) algorithm for including free surface topography in synthetic seismogram analysis. The realism of this method is demonstrated through displays of snapshots and synthetic seismograms of a shallow explosion for models without and with topography included. (continue on next page)			
20. DISTRIBUTION/AVAILABILITY OF ABSTRACT <input checked="" type="checkbox"/> UNCLASSIFIED/UNLIMITED <input type="checkbox"/> SAME AS RPT <input type="checkbox"/> DTIC USERS		21. ABSTRACT SECURITY CLASSIFICATION Unclassified	
22a. NAME OF RESPONSIBLE INDIVIDUAL Dr. Stanley K. Dickinson		22b. TELEPHONE (Include Area Code) (202) 767-5021	22c. OFFICE SYMBOL AFOSR/NL

Previous editions are obsolete.

SECURITY CLASSIFICATION OF THIS PAGE

Unclassified

94-02692

94 1 26 144

**UNCLASSIFIED**  
**SECURITY CLASSIFICATION OF THIS PAGE**

Regarding ongoing research, most efforts have been devoted to 2D FD synthetics for simulating seismic wave propagation in a complex lithosphere. In practice model set-up for FD computations have proved cumbersome so we are elaborating on automating structural model generation. The new approach is tied to using an optical scanner for reading a figure of the multilayered crustal model.

Event magnitude is an versatile parameter in many seismological studies not at least in the context of nuclear test ban monitoring. For simulating network signal detection capabilities the noise level at individual stations are needed which in practice appears difficult to obtain. Ideally, we would prefer to have such noise level estimates available on-line to measure the 'on-line threshold monitoring' performance. Most signal detections in use are of the STA/LTA type where the short-term-average (STA) is in fact an a RMS trace estimate. Initial test attempting to relate STAs to maximum amplitude used in local magnitude formulas shows that error less than 0.1 magnitude unit should be feasible.

The new Sonseca (ESLA) seismic array near Toledo, Spain, has recently become operational. For its operation, crustal structure models are of some importance. Using Pn and Sn travel time observations from the Iberian seismograph network we have derived a 2D map of subMoho P- and S-velocity variations for this area. The central parts of the region appears to be rather homogeneous while the largest anomalies are to the south. Crustal thickness variations are pronounced ranging from about 20 to 40 km.

Finally, a comprehensive study aimed at seismic event classification at local and regional distances has been started. Preparatory efforts here comprise software development and selection of a comprehensive data base. The research strategy is aimed at examining the discriminative potential of any part of the seismic records as bracketed by the group velocity interval 8.5 to 2.5 km/sec. Special attention would be given to focal depth estimation through inversion of relatively low-frequency recordings for small events at local and regional distances.

**Unclassified**  
**SECURITY CLASSIFICATION OF THIS PAGE**

## Contents

<b>1 Overview</b>	<b>2</b>
1.1 Objectives . . . . .	2
1.2 Summary of ongoing research . . . . .	2
1.3 Summaries of studies completed . . . . .	3
1.4 Outline of the report . . . . .	3
<b>2 Ongoing research activities</b>	<b>5</b>
2.1 Seismic event classification . . . . .	5
2.2 Real-Time Magnitude Estimation . . . . .	8
2.3 Crustal structure of Iberia . . . . .	12
2.4 Crustal modelling for 2D synthetics . . . . .	20
<b>3 Studies completed</b>	<b>24</b>
3.1 Spatial and temporal patterns of the Fennoscandian seismicity - an exercise in explosion monitoring . . . . .	24
3.2 2D finite difference elastic wave modeling including surface topography . . . . .	25
3.3 Seismic wave propagation in complex crust - upper mantle media using 2D finite difference synthetics . . . . .	26
<b>4 Future work plans</b>	<b>27</b>
<b>5 Appendix A</b>	<b>A-1</b>
<b>6 Appendix B</b>	<b>B-1</b>

DTIC QUALITY INSPECTED 8

Accession For	
NTIS	CRA&I
DTIC	TAB
Unannounced	<input checked="" type="checkbox"/>
Justification	
By _____	
Distribution /	
Availability Copies	
Dist	Avail. for Special
A-1	

# 1 Overview

## 1.1 Objectives

- Foster a better understanding of seismic wave propagation in complex lithospheric media.
- Principal modelling tool is 2D finite difference (FD) synthetics for models also including surface topography.
- Corroborating synthetics through analysis of array and network data.
- Use 'synthetic' knowledge in design of event classification schemes.
- Seismic network performance.

Note, a basic element in research is curiosity which in practice will imply a certain flexibility regarding adherence to objectives.

## 1.2 Summary of ongoing research

Most efforts have been devoted to 2D FD synthetics for simulating seismic wave propagation in a complex lithosphere. The FD scheme used is tied to the numerical solution of the elastodynamic wave equation. Spatial partial differentiation is achieved through cost-optimized, dispersion-bounded, high-order finite difference operators on a staggered grid. For time stepping, a leap-frog technique is used. For the numerical dispersion relations, the stability limit and bandwidth introduced by the discretization, the reader is referred to Sguazzero, Kindelan and Kamel (1989).

Recently we have demonstrated the usefulness of this approach by computing synthetic seismograms for a set of progressively complex lithosphere models (Hestholm, Husebye and Ruud, 1994). In practice, model set-up for FD computations have proved cumbersome so we are elaborating on automating structural model generation. The new approach is tied to using a scanner for reading a published multilayered crustal model. For any model point proper layer assignment is performed automatically and hence a corresponding specification of physical parameters like velocity and density. The computed synthetics are SEG-Y formatted and thus can easily be processed using standard software packages like the ProMAX.

Event magnitude is a versatile parameter in many seismological studies not at least in the context of nuclear test ban monitoring. For simulating network signal detection capabilities the noise level at individual stations are needed which in practice appears to be difficult to obtain. Ideally, we would prefer to have such noise level estimates available on-line to measure the 'on-line threshold monitoring' performance (Ringdal and Kværna, 1992). To achieve this we are exploring the usefulness of a random vibration theory formula, namely (Cartwright and Longnet-Higgins, 1956).

$$A_{\max} = f(N) A_{\text{rms}} \quad (1)$$

where  $A_{\max}$  is max amplitude;  $f(N)$  where  $N$  is the number of extrema with the RMS-window and  $A_{\text{rms}}$  is amplitude root-mean-square. Most signal detections in use are of the STA/LTA type where the short-term-average (STA) is in fact an a (RMS) trace estimate. Initial test results from real recordings indicate that the above formula is valid; error estimates amount to  $\pm 0.1$  magnitude unit. In other word, on-line magnitude estimation should be feasible.

The new Sonseca (ESLA) seismic array near Toledo, Spain, has become operational. For its operation, crustal structure models are of some importance for slowness-vector calibration and related purposes. Using Pn and Sn travel time observations from the Iberian seismograph network with supplementary observations from stations in France, Algeria and Morocco we have derived a 2D map of subMoho P- and S-velocity variations for Iberia and adjacent areas. The central parts of the region appears to be rather homogeneous while the largest anomalies are found in the Betics and the Alboran Sea to the south. Crustal thickness variations are also pronounced in this area ranging from c. 20 to 40 km.

Finally, a comprehensive study aimed at seismic event classification at local and regional distances. Preparatory efforts here comprise software development and selection of a comprehensive data base; we opted for the NORESS and ARCESS events used by Lacoss et al. (1992). The research strategy is aimed at examining the discriminative potential of any part of the seismic records as bracketed by the group velocity interval 8.5 to 2.5 km/sec. Special attention would be given to focal depth estimation through inversion of relatively low-frequency recordings for small events at local and regional distances. Various schemes for suppression of propagating noise on 3 component recordings are now under considerations; if successful we experiment with wave form inversion for accurate estimation of focal depths.

### 1.3 Summaries of studies completed

In addition to the paper (Hestholm et al, 1994) included in the First Scientific Report submitted to AFOSR (19. May 1993) two other studies have been completed in the reporting period: Tarvainen and Husebye (1994) and Hestholm and Ruud (1994). The first of these reports deals with spatial and temporal patterns in Fennoscandian seismicity essentially amounting to an exercise in monitoring mining and other explosions. We demonstrate that there exist a very consistent diurnal/weekly and spatial patterns for the numerous explosion events included in local seismological bulletins. The seismological epicenter locations are clearly inferior to these made by a skilled analyst and tied to waveform stationarity for a given mine.

The other study (Hestholm and Ruud, 1994) presents a numerical 2D finite difference (FD) algorithm for including free surface topography in synthetic seismogram analysis. The realism of this report is also demonstrated through displays of snapshots of near surface effects for models without and with topography included.

### 1.4 Outline of the report

The First Technical Report under Contract AFOSR Grant F49620-92-5-0510 is divided in 2 parts; in Section 2 we give details on ongoing research while in Section 3 we present abstracts of studies completed and also discuss some implications of the results obtained here. The completed text of these 2 reports are given in Appendix A and B.

## References

- Cartwright, D.E., and Longuet-Higgins, M.S., 1956. The statistical distribution of the maxima of a random function, *Proc. Roy. Soc. London, Ser. A* 237, 212-223.
- Hestholm, S.O., Husebye, E.S., and Ruud, B.O., 1994. Seismic wave propagation in complex crust - upper mantle media using 2D finite difference synthetics, *Geophys. J. Int.*, in press.
- Hestholm, S.O. and Ruud, B.O., 1994. 2D finite difference elastic wave modeling including surface topography, *Geophysical Prospecting*, in press.
- Lacoss, R., Cunningham, R., Curtis, S., and Seibert, M., 1991. Artificial neural networks for seismic interpretation, *Technical Report, ESD-TR-91-170*, MIT Lincoln Laboratory, Lexington, MA.
- Ringdal, F., and Kværna, T., 1989. A multi-channel processing approach to real time network detection, and threshold monitoring, *Bull. Seism. Soc. Am.*, 79, 1927-1940.
- Sguazzeri, P., Kindeland, M., and Kamel, A., 1989. Dispersion-Bounded Numerical Integration of the Elastodynamic Equations, *Proceedings of the ICOSAHOM Conference, Como, Italy, June, 1989*, pp. 165-172. North Holland Publishing Company, The Netherlands.
- Tarvainen, M. and Husebye, E.S., 1994. Spatial and temporal patterns of the Fennoscandian seismicity - an exercise in explosion monitoring, m/s submitted for publication.

## 2 Ongoing research activities

Here we give details on ongoing research activities some of which are scheduled for completion at 15. February 1994 i.e., the deadline for contributions for the proceedings of the WORKSHOP ON PLANNING AND PROCEDURES FOR GSETT-3 held in Erice, Italy 11-13 November 1993. As is well known GSETT-3 is short for group of Scientific Expert Technical Test no. 3 which is an exercise in testing various aspects of a prototype global seismic monitoring system for a potential comprehensive nuclear test treaty (CTBT). The GSE reports to the UN Conference on Disarmament in Geneva.

### 2.1 Seismic event classification

In recent years there has been renewed interest in event classification of small local events which remain problematic. The many studies undertaken here reflect the renewed political interest in a comprehensive test ban treaty effectively prohibiting any test of nuclear weapons. Most promising discriminant at local distances appears to be the spectral ratio of Pn/Lg-phases in the frequency band 2-5 Hz. Physically the explanation is that earthquakes source excitation is relative effective in generating shear waves. Since up to now most nuclear testing are confined to a few sites, a fair amount of classification research is tied to discriminating between earthquakes and chemical explosions stemming from mining and quarry blasting activities. In comparison to nuclear tests the chemical explosions are truly numerous so the challenge is naturally to be able to differentiate between the 3 major types of seismic sources, namely earthquakes (EQ), nuclear explosions (NE) and chemical explosions (CE). For convenience the explosions are referred to as EX unless we need to distinguish between NE and CE. A distinct signal attribute of CE is the so called spectral scalloping effect caused by the commonly used technique of ripple firing typical of large chemical explosions (Hedlin et al, 1990).

The recent trend in seismic event classification research is to introduce a multitude of potential discriminants and then use non-statistical techniques like artificial neural networks (ANN) schemes to ensure optimum performances. A possible drawback with the ANN approach is that the learning set has to be large (say 50 events each for the EQ and EX populations) and also that there is no easy assessment of the relative merits of the individual discriminants. In contrast, statistical approaches like those based on pattern recognition schemes (Tjøstheim, 1982; Tsvang et al, 1993) function well for relative small event populations and also enable us to estimate the relative significance of individual discriminants. The latter technique can be extended to handle one-sided event populations that is explosions only or earthquakes only. For strong events, recorded by many stations in the teleseismic window, seismic event classification is not problematic and even traditional mb:Ms and complexity discriminants are very efficient.

#### *Seismic Discriminant Features*

Numerous studies on seismic event classification during the last decade have been based on spectral characteristics of crust and upper mantle phases like Pn, Pg, Lg, Rg etc. or on their spectral ratios in a multitude of frequency bands. This in turn reflect extensive observational experiences that explosions and earthquakes produce different spectral amplitudes for the same direct phase at comparable distance ranges and wave paths (Pulli and Dysart, 1992). A potential drawback with this class of discriminants is that the direct wave phases can be strongly affected

by a particular source-receiver path thus making it difficult to separate source and propagation effects. In the extreme a certain discriminant may fail when the EXs and the EQs are not closely located. A related problem is that late P-coda waves, direct Sn, Lg and surface waves are mixed together and the isolation of separate phases are not trivial. In this context, Lg-coda waves exhibit a distinct advantage as a characteristic feature here is that their amplitude decay with distance reflects the average crustal properties of the region encompassing the source and the receivers (e.g., see Su et al. 1991). In other words we can separate source and path effects on the coda waves. Likewise, the spectral scalloping effect stemming from ripple firing in mining operations appears to be most distinctive in the coda (Hedlin et al., 1990).

#### *Data Analysis Strategy*

The data at hand for classification analysis stem from array and 3-component (3C) station recordings from events at local and regional distance ranges. This in turn would entail that a flexible analysis strategy should be implemented simply because signal and coda durations are distance dependent. Another problem is that of introducing corrections for geometrical spreading and attenuation both of which appear to vary considerably from one region to another and also within a given region. Such corrections, often ignored in many event classification studies, should be introduced as in case of the powerful Pn/Lg discriminant both the geometrical spreading and attenuation are different for these two phases. Linear event scaling would also be important except for spectral ratio type of discriminants because we undertake a comparison of event with different magnitudes. With array data at hand we want to incorporate measures to facilitate assessment of the relative merits of such recording systems vis-a-vis modern 3C stations. Finally, to retain flexibility we decided from the very onset to perform our analysis on sonogram data (signal power as a function of time and frequency averaged over the array elements) with the added advantage of reducing the storage requirements of the original time domain recordings.

We recognize the following principal part of any local/regional seismic record; Preceeding noise, Pn, Pg, P-coda, Sn, Lg and Lg-coda. The noise is of duration 30 to 60 sec depending of available record length. The body wave phases are of length 3.2 to 6.4 sec and distance dependent. The P-coda is the segment between Pn/Pg-end and Sn/Sg-start. The Lg is taken to start a sec prior to given start time or alternatively to the equivalent group velocity onset time of 3.6 km/sec. Lg ends at the 'group velocity' time of 3.2 km/sec. The Lg-coda ends at an equivalent group velocity of 2.0 km/sec. We will experiment with a coda subdivision in 3 segments that is of group velocity lengths of 3.2-2.8; 2.8-2.4 and 2.4-2.0 km/sec respectively. The basic spectrum analysis is performed via the Fast Fourier Transform (FFT) for data windows of unit length 3.2 sec (128 samples) with Hanning type tapering. The spectrum is updated at 1.6 sec intervals, and additional smoothing is introduced by stacking of spectrum segments.

#### *Study Summary*

So far most of our efforts have been tied to software development and getting access to a large data base of seismic array events. It is not quite trivial to use these excellent CSS-generated data bases but practical advises from R. Lacoss (Lincoln Lab.) proved very helpful. Adapting to a new computer environment in Bergen have also taken time. Anyway, we are now in the position to start large scale discriminant feature extraction from a large number of local and regional events

as recorded by the NORESS and ARCESS arrays.

*Anton Dainty*  
(Phillips Laboratory)

*Bent O. Røud*

*Eystein S. Husebye*

## References

- Blandford, R., 1993. Discrimination of Earthquakes and Explosions at Regional Distances Using Complexity, AFTAC-TR-93-044, Air Force Technical Applications Center, Patrick Air Force Base, Florida.
- Hedlin, M.A., Minster, J.B. and Orcutt, J.A., 1990. An automatic means to discriminate between earthquakes and quarry blasts. Bull. Seism. Soc. Am., 80, 2143 - 2160.
- Pulli, J. and Dysart, P., 1992. Analysis and testing of high-frequency regional seismic discriminants, Phillips Laboratory Report PL-TR-92-2125, pp 58.
- Su, F., Aki, K. and Biswas, N.N., 1991. Discriminating quarry blasts from earthquakes using coda waves. Bull. Seism. Soc. Am., 81, 162 - 172.
- Tjøstheim, D., 1981. Multidimensional discrimination techniques - theory and application, in Identification of Seismic Sources - Earthquakes or Underground Explosions, pp 663 - 694, eds. Husebye, E.S., Mykkeltveit, S., D. Reidel Publ., Dordrecht, The Netherlands.
- Tsvang, S.L., Pinsky, V.I., and Husebye, E.S., 1993. Enhanced seismic source discrimination using NORESS recordings from Eurasian events. Geophys. J. Int., 112, 1 - 14.

## 2.2 Real-Time Magnitude Estimation

The problem of estimating the size of an earthquake (EQ) has intrigued seismologists for many years and still does. As a first and subsequently widely accepted substitute for EQ energy release, Richter introduced his magnitude scale for Californian events in 1935. Over the years, a large number of magnitude scales has been introduced for a variety of seismic phases and different tectonic provinces (e.g., see Bath 1981.). All these magnitude scales are basically similar, namely of the form;

$$M = \log\left(\frac{A}{T}\right) + g(\Delta, f) + c \quad (1)$$

where  $M$  is magnitude,  $A$  is peak ground displacement for the seismic phase in question,  $g(\Delta, f)$  incorporates geometrical spreading and inelastic attenuation terms and  $c$  represents the station correction. The term  $T$  is the corresponding signal period.

The event magnitude parameter is coupled to the seismic moment  $M_0$  (Aki, 1967) through the formula of the form;

$$\log M_0 = 1.03M - 17.1 \quad (2)$$

This formula is taken from Sereno et. al. (1988) and  $M$  relates to  $Lg$  phases for local/regional events. Although the magnitude parameter is less clearly related to the earthquake size than the moment, the magnitude is popular due to its versatility and computational ease. Recently, noise level has become an important parameter for estimating network surveillance capabilities, say in the context of a comprehensive nuclear test ban treaty. In this study we focus on an approach to estimate event magnitude in near real-time and start with a brief description of current seismic signal detectors. Obviously, parameters extracted during this operation have to serve as a basis for magnitude estimation.

The most popular signal detectors in use are the so-called sliding window STA/LTA type which is a comparison of short and long term trace amplitude ( $a_i$ ) averages (e.g., Ruud and Husebye, 1992). Common STA definitions are of the forms;

$$STA(abs) = \sum_{i=1}^n |a_i| \quad (3)$$

$$STA(rms) = \left[ \frac{1}{n} \sum_{i=1}^n a_i^2 \right]^{\frac{1}{2}} \quad (4)$$

When the STA/LTA ratio exceeds a present threshold, the presence of a seismic signal is declared. Our preference is for the RMS related STA-LTA definitions since signal RMS is related to the signal power spectrum via the Parseval's theorem, namely;

$$\sum_{-\infty}^{\infty} a^2(t) = \frac{1}{2\pi} \int_{-\pi}^{\pi} A^2(\omega) d\omega \quad (5)$$

By extensive analysis of observational data Ringdal and Kværna (1989) have established empirical relationships between STA and event magnitudes. We want to pursue another approach, namely to attempt relating the STA(RMS) to maximum ground motion amplitude of a given P/S/Lg - phase and this conform with the original Richter (1935) magnitude definition. This problem is rather similar to a one dealt with in seismic hazard analysis, namely how to generate realistic

ground motion spectra using random vibration theory (RVT) which may be particularly appropriate if the waveforms have a random character (Boore, 1983). From the RVT results of Cartwright and Longuet-Higgins (1956) we have

$$E(A_{max}) = A_{rms} f(N) \quad (6)$$

where  $E(A_{max})$  is the expected value of  $A_{max}$  and  $N$  is the number of extremes in the  $A_{rms}$  trace window. When  $N$  is large,  $f(N)$  can be approximated by;

$$f(N) \approx (2 \ln N)^{\frac{1}{2}} \quad (7)$$

When  $N$  becomes small, say between 2 and 5, a better approximation may be;

$$f(N) \approx (2 \ln N)^{\frac{1}{2}} + \gamma(2 \ln N)^{-\frac{1}{2}} \quad (8)$$

where  $\gamma$  is Euler's constant and equals to 0.5772... The Eq(4) and Eq(6) establish a relationship between maximum trace amplitude and the trace RMS value. If we adopt the RMS-variance of the STA-definition in Eq(3), then an estimate of maximum signal/phase amplitude would be at hand in near real-time. For the conversion to event magnitude we need an epicenter distance estimate which in case of arrays may be tied to the 'best' beam location. Since the STA parameter also is available for the non-detection state, that is for the pure noise portions of the recordings, the corresponding maximum amplitude estimates provide a measure of the lower magnitude threshold for seismic event detection. We can also determine the corresponding error in the magnitude estimate by a simple derivation of Eq(1);

$$dM = \frac{1}{\ln(10)} \frac{dA}{A} \quad (9)$$

where  $dA$  is the derivative of the  $A(max)$  value.

In RVT theory, derivation of Eqs(5 - 7), the time series is presumed stationary and individual samples to be independent. This is hardly the case for seismic recordings, so we have simply started to test validity of Eqs(5 - 7) using real seismic recordings. The aim of such an experiment is shown in Fig. 2.2.1; the following comments apply. There is clearly a simple linear relationship between maximum trace amplitude and the corresponding RMS value for the entire seismic recordings. The scattering is moderate given that the RMS or STA window length is at least twice the dominant signal frequency. In case of band filtered records (for noise suppression), the center frequency of the pass band is a good measure of the dominant signal frequency. The number of extremes within the RMS window at least for bandpass filtered records is also very stable. The corresponding magnitude errors according to Eq(8) seldom exceed  $\pm 0.1$  units which is considered fully acceptable. For shorter windows, the  $A_{max}/STA(RMS)$  relation still holds but scattering increases. We conclude in the basis of present experience with analysis of real recording that near real-time event magnitude estimate can be possible.

We are now undertaking works on incorporating the 'on-line magnitude' concept in the automatic analysis of seismic network recordings. In example, Ruud and Husebye (1993) have recently demonstrated that the 3C signal detector could reliably pick phase onset times while correct phase identification could occasionally be problematic. We expect that on-line magnitude estimates for a specific event location would contribute towards better phase identifications. In a threshold monitoring context we could have an attempt to on-line estimation of seismic network event detection

capability using on-line noise magnitude estimates from globally distributed station and arrays (e.g., Sereno et. al., 1988, Kværna and Ringdal, 1992).

C. Deniz Mendi

Eystein S. Husebye

## References

- Aki, K., 1967. Scaling law of seismic spectrums, *J. Geophys. Res.*, **73**, 1217-1231.
- Boore, D.M., 1983. Stochastic simulation of high-frequency ground motions based on seismological models of the radiated spectra, *Bull. Seism. Soc. Am.*, **73**, 1865-1894.
- Båth, M., 1981. Local magnitude: recent research and current trends, *Earth Sci. Rev.*, **17**, 315-398.
- Cartwright, D.E., and Longuet-Higgins, M.S., 1956. The statistical distribution of the maxima of a random function, *Proc. Roy. Soc. London, Ser. A* **237**, 212-223.
- Ringdal, F., and Kværna, T., 1989. A multi-channel processing approach to real time network detection, and threshold monitoring, *Bull. Seism. Soc. Am.*, **79**, 1927-1940.
- Ringdal F., and Kværna, T., 1992. Continuous seismic threshold monitoring, *Geophys. J. Int.*, **111**, 505-514.
- Ruud, B.O., and Husebye, E.S., 1992. A new three-component detector and automatic single station bulletin production, *Bull. Seism. Soc. Am.*, **82**, 221-237.
- Ruud, B.O., Lindholm, C.D., and Husebye, E.S., 1993. An exercise in automating seismic record analysis and network bulletin production, *Bull. Seism. Soc. Am.*, **83**, 660-679.
- Sereno, T.J., Bratt, S.R., and Bache, T.C., 1988. Simultaneous inversion of regional wave spectra for attenuation and seismic moment in Scandinavia, *J. Geophys. Res.*, **93**, 2019-2035.

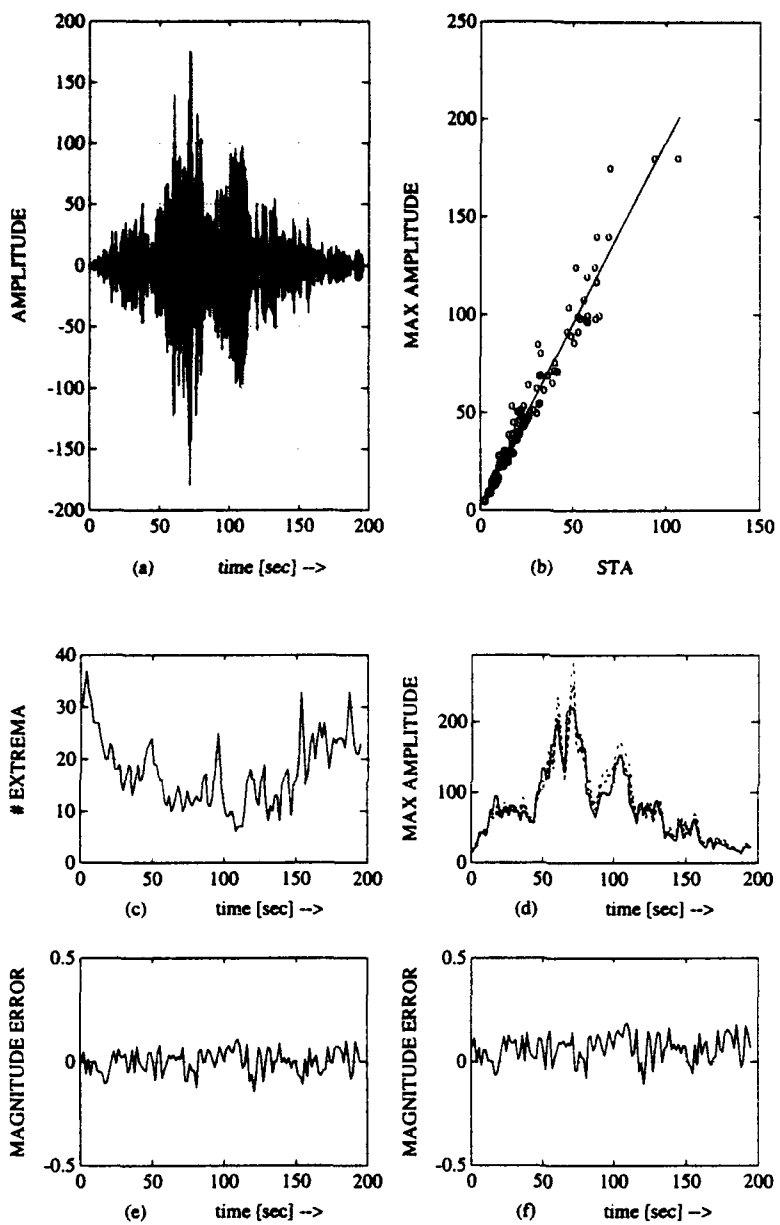


Figure 2.2.1: (a) shows a sample event whose frequency bandwidth is between  $0.75 - 1.5\text{Hz}$ . (b) The relation between the RMS (STA) values and the max amplitudes for a sliding window is illustrated and the linear line which fits best in the sense of residual error is also depicted. The STA window length is 3.2 sec and the sampling frequency of the signal equals to  $25\text{Hz}$ . (c) shows the number of extremes, and (d) the corresponding maximum amplitude evaluations are depicted; *i*) solid line is the original maximum amplitude, *ii*) dashed line represents RVT, whereas *iii*) dotted line is the evaluations for asymptotic expressions. The magnitude estimation error for (e) the RVT, and (f) the asymptotic expressions are depicted.

### 2.3 Crustal structure of Iberia

The regional array Sonseca (ESLA) near Toledo, Spain is now operational, and in this context we have taken the opportunity to examine the crustal structure of the Iberian Peninsula in terms of Pn and Sn velocity distributions as derived from tomographic inversions of local bulletin data. A brief description of this work is given below; we start with a few words on the evolution of Iberia.

The geodynamic evolution of the Iberian peninsula and the western Mediterranean is undoubtedly complex (Dewey et al., 1989; Platt and Vissers, 1989), involving both compressional tectonics related to the convergence of the African and Eurasian plates during the Eocene, as evidenced by the Pyrenees and the Betic Cordillera, and subsequent extensional tectonics, as evidenced by the creation of the Valencia Trough and the Alboran Sea. It is expected that the evolution of some of these major tectonic features may be reflected in the deeper lithospheric structure.

Extensive seismic and seismological studies of the Iberian lithosphere have been undertaken over the last few years. Several long-range seismic refraction profiles have been carried out traversing the peninsula and at sea, providing details of crustal thickness and velocities, both at its Hercynian core (e.g. Medialdea et al., 1986; Cordoba et al., 1988; Surinach and Vegas, 1988, ILIHA DSS Group, 1993) and in areas such as the Betic Cordillera and Alboran Sea which have special tectonic significance (e.g. Medialdea et al., 1986, Banda et al., 1993) (Fig. 2.3.1). Additional information can also be obtained using data collected by dense seismograph networks; arrival times of Pn and Sn phases recorded by these networks can be analysed using tomographic techniques to obtain estimates of sub-Moho P- and S-velocities.

In this study we derive estimates of the Pn and Sn velocity distribution beneath the Iberian peninsula by carrying out tomographic inversion on a subset of earthquake arrival time data routinely collected by the Spanish National Seismograph Network (Fig. 2.3.1b). The tomographic inversion algorithm used is a least square conjugate gradient (CGLS) technique described in detail by Spakman and Nolet (1988) and Blanco and Spakman (1993). In the inversion we allow for known variation in crustal thickness and include the hypocentral parameters as unknowns. This permits further event relocation using the velocity estimates found in the inversion (e.g., see Bannister et al., 1991).

We use a two-layered model for the lithosphere, the upper layer of which is taken to represent the crust. The initial model of the crustal thickness, shown in Fig. 2.3.2, was primarily based on results from seismic refraction profiling (e.g. see Badal et al., 1993) supplemented with results derived from surface wave dispersion studies (e.g. see Badal et al., 1992). The Iberian crust has a relatively uniform thickness, 30-34 km, but is notably thicker in the Pyrenees (Surinach et al., 1993) and the Betics (Banda et al., 1993). The crust thins rapidly towards the Alboran Sea; Paulssen and Visser (1993) give a thickness of only 20 km in the coastal area around Malaga.

Forward modelling of the seismic travel times was initially carried out using ray-tracing through a starting model involving no lateral velocity variation, only crustal thickness variations. Critically refracted Pn and Sn phases are modelled travelling just beneath Moho in the upper mantle. Both model layers are sub-divided into blocks of constant velocity and size  $0.5^\circ \times 0.5^\circ$  in latitude and longitude. Ray paths along great circles may appear slightly curved relative to the chosen grid system. Variation in crustal thickness immediately beneath a seismograph station or event was allowed for by varying the thickness of the upper layer (the crust) but keeping the (local) Moho interface horizontal.

The rays were traced as straight lines between the hypocentre and the station in both the upper (crust) and lower (sub-Moho) layers. Angles of incidence at the layer boundaries were taken into account using the respective block velocities. The effect of a local potentially slanting Moho was ignored. Sub-Moho ray paths were assumed to be horizontal, although differences in the crustal thickness beneath the station and hypocentre were accounted for by introducing a length scaling factor. Initial model reference P and S velocities were 6.4 and 3.65 km/s in the crust and 8.0 and 4.57 km/s sub-Moho respectively. These Pn and Sn velocities were derived from regression analysis of the Pn and Sn travel time observations and thus reflect the velocity model used in routine hypocentre determinations for the Iberian network.

The use of tomographic row-action techniques prevents us from calculating formal resolution and standard errors for the estimated (unknown) parameters. As a substitute we inverted a synthetic data set constructed by using the ray population from the actual data set while calculating travel times using artificial slowness anomalies. The synthetic model used consisted of alternating bodies with low (8.0 km/s) and high (8.40 km/s) sub-Moho velocity, with a background velocity of 8.2 km/s. The crust was presumed to be homogeneous and with an initial velocity of 6.40 km/s. As expected the velocity anomalies in the northern parts of Spain and in the eastern Pyrenees are not well resolved due to the poor ray-path sampling. In contrast the P-velocity reconstruction for the southern and western parts of Iberia appears adequate, as it does also for parts of the Ebro basin and the Pyrenees. The reconstructed velocity pattern smears seaward and in many coastal areas, except to the west of Lisbonne and in the Gulf of Cadiz where it appears that useful results may be obtainable. Similar resolution can be expected in the S-wave velocity because ray paths are similar.

The inversion method used here has some limitations, as noted above. One assumption is that all of the sub-Moho arrivals represent head waves, with no regard for distance. Synthetic modelling (e.g. Hestholm et al 1994) demonstrates that Pn energy may represent both sub-Moho head waves and turning waves within the upper mantle. It is difficult to differentiate between these two wave paths using only travel time observations and there is little knowledge of the P-wave velocity gradients within the upper mantle beneath the Iberian peninsula. The head-wave assumption should be reasonable given the relatively limited distance range involved for most of the data. It is difficult to get a quantitative idea of the degree to which this assumption may affect the inversion results.

Fig. 2.3.3a shows the Pn velocity distribution determined from inversion of the Pn arrival time data set. The Pn velocities vary between 7.7 km/s (light grey) and 8.3 km/s (dark grey). The striking feature is the low (7.7-7.8 km/s) velocity feature in the Alboran Sea, to the west of Gibraltar Strait, and to the south of Portugal in the Atlantic. This feature is presumably related to the Neogene extension of the Alboran Sea region. There is also a high velocity anomaly beneath the Sierra Nevada Ranges (Betics). The sensitivity modelling shows that the ray path coverage in these areas is adequate for good resolution.

The Pn velocity beneath the Iberian Massif and central Spain is relatively constant at around 8.0-8.1 km/s. This velocity is similar to that found in refraction studies of the region (e.g. Banda et al., 1981). For northwest Spain we observe slightly lower Pn velocities, around 7.9-8.0 km/s, close to that observed from several seismic refraction/wide-angle profiles carried out close to the Atlantic coastline in that region (Cordoba et al., 1988).

Shear wave (Sn) velocities estimated from the tomographic inversion are shown in Fig. 2.3.3b,

with light grey shades representing slow velocities and dark grey shades representing high shear wave velocities. Low Sn velocities, of around 4.50 km/s, are observed both in the Alboran Sea and, onland, beneath Gibraltar, as well as beneath Tagus Basin and Central System. High Sn velocities, of around 4.65 km/s, are observed close to the Guadalquivir Basin and the central part of the Betic Cordillera. Little velocity variation is observed across most of the Iberian Massif. In a detailed study of velocity dispersion of surface waves across the Iberian peninsula Badal et al (1992) found only small lateral variations in shear wave velocities over most of the peninsula. They did however find significant effects associated with the root of the Betic Cordillera, with low shear wave velocities at around 50 km depth, but high velocities (relative to the Iberian Massif) near the Moho. It is clear that the shear wave velocity distribution is quite complex beneath the Betic Cordillera.

In summary, Pn and Sn velocity anomalies have been derived for the Iberian Peninsula which correlate with some of the tectonic units of the region. Low Pn velocities are clearly related to the Alboran Sea region and the area west of Gibraltar Strait. High Pn velocities are mainly related to parts of the Hercinian Massif and the Betic Cordillera. Low Sn velocities are associated with the Alboran Sea. Our results, obtained from tomographic inversion, are complementary to results obtained from a variety of previous studies of the crust and mantle beneath the Iberian peninsula (e.g. Mezcua and Udias, 1991, Badal et al. 1992, Payo et al. 1972 a,b, Banda et al., 1993, Plomerova et al. 1993, and Blanco and Spakman, 1993).

S.C. Bannister  
(Wellington)

G. Payo  
(Toledo)

E.S. Husebye

## References

- Aki, K. and Lee, W.H.K., 1976. Determination of three-dimensional velocity anomalies under a seismic array using first P arrival times from local earthquakes (part 1). *J. Geophys. Res.*, 81, 4381-4399.
- Badal, S., Corchete, V., Payo, G., Seron, F.J., Canas, J.A., Pujades, L., 1992. Deep structure of the Iberian Peninsula determined by Rayleigh wave velocity inversion, *Geophys. J. Int.*, 108, 71-88.
- Badal, S., Gallart, J., and Paulssen, H., (eds) 1993. Seismic studies of the Iberian Peninsula, *Tectonophysics*, 221, 1-34.
- Banda, E., Surinach, E., Aparicio, A., Sierra, J., and Ruiz de la Parte, E., 1981. Crust and upper mantle structure of the central Iberian Meseta (Spain), *Geophys. J. R. astr. Soc.*, 67, 779-789.
- Banda, E., Gallart, J., Garcia-Duenas, V., Danobeitia, J.J. and Makris, J., 1993. Lateral variation of the crust in the Iberian peninsula: new evidence from the Betic Cordillera, *Tectonophysics*,

221, 53-66.

Bannister, S.C., Ruud, B.O., and Husebye, E.S., 1991. Tomographic estimates of sub-Moho seismic velocities in Fennoscandia and structural implications. *Tectonophysics*, 189, 37-53.

Blanco, M.J. and Spakman, W., 1993. The P-wave velocity structure of the mantle below the Iberian Peninsula: evidence for subducted lithosphere below southern Spain. *Tectonophysics*, 221, 13-34.

Cordoba, D., Banda, E. and Ansorge, J., 1988. P-wave velocity-depth distribution in the Hercynian crust of NW Spain, *Phys. Earth Planet. Int.*, 51, 235-248.

Dewey, J.F., Helman, M.L., Turco, E., Hotton, D.W.H. and Knott, D.S., 1989. Kinematics of the western Mediterranean, in *Alpine Tectonics*, pp. 2654-283, eds. Coward, M.P., Dietrich, D. and Park, R.G., Geological Society of London Special Publ. 45.

Hestholm, S.O., Husebye, E.S., and Ruud, B.O., 1994. Visualizing seismic wave propagation in complex crust - upper mantle media using 2D finite difference synthetics, *Geophys. J. Int.*, in press.

ILIHA DSS Group, 1993. A deep seismic sounding investigation of lithospheric heterogeneity and anisotropy beneath the Iberian Peninsula, *Tectonophysics*, 221, 35-51.

Medialdea, T., Surinach, E., Vegas, R., Banda, E. and Ansorge, J., 1986. Crustal structure under the western end of the Betic Cordillera (Spain), *Ann. Geophys.*, 4(B4), 457-464.

Mezcua, J. and Udias, A., 1991. Seismicity, seismotectonics and seismic risk of the Ibero-Maghrebian Region, Monografia no. 8, IGH, Instituto Geografico Nacional, Madrid, Spain, 3-15.

Paulissen, H. and Visser, J., 1993. The crustal structure in Iberia inferred from P-wave coda, *Tectonophysics*, 221, 111-124.

Payo, G., 1972a. P-wave residuals at some Iberic stations and deep structure of south-western Europe, *Geophys. J.R. Astron. Soc.*, 26, 481-497.

Payo, G., 1972b. Crust-mantle velocities in the Iberian Peninsula and tectonic implications of the seismicity in this area, *Geophys. J.R. Astron. Soc.*, 30, 85-99.

Platt, J.P. and Vissers, R.L.M., 1989. Extensional collapse of thickened continental lithosphere: a working hypothesis for the Alboran Sea and Gibraltar arc, *Geology*, 17, 540-543.

Plomerova, J., Payo, G. and Babuska, V., 1993. Teleseismic P-residual study in the Iberian Peninsula, *Tectonophysics*, 221, 1-12.

Smith, W.H.F., and P. Wessel, 1990. Gridding with continuous curvature splines in tension, *Geophysics*, 55, 293-305.

- Spakman, W. and Nolet, G., 1988. Imaging algorithms, accuracy and resolution in delay time tomography. In: N.J. Vlaar et al (eds.), Mathematical Geophysics; A survey of recent developments in seismology and geodynamics, Reidel, Dordrecht, 155-188.
- Surinack, E. and Vegas, R., 1988. Lateral inhomogeneities of the Hercynian crust in central Spain, *Phys. Earth Planet. Int.*, 51, 226-234.
- Surinack, E., Marthelot, J.-M., Gallart, J., Daignieres, M. and Him, A., 1993. Seismic images and evolution of the Iberian crust in the Pyrenees, *Tectonophysics*, 221, 67-80.
- Wessel, P., and W.H.F. Smith, 1991. Free software helps map and display data, *EOS Trans.AGU*, 72, 441, 445-446.

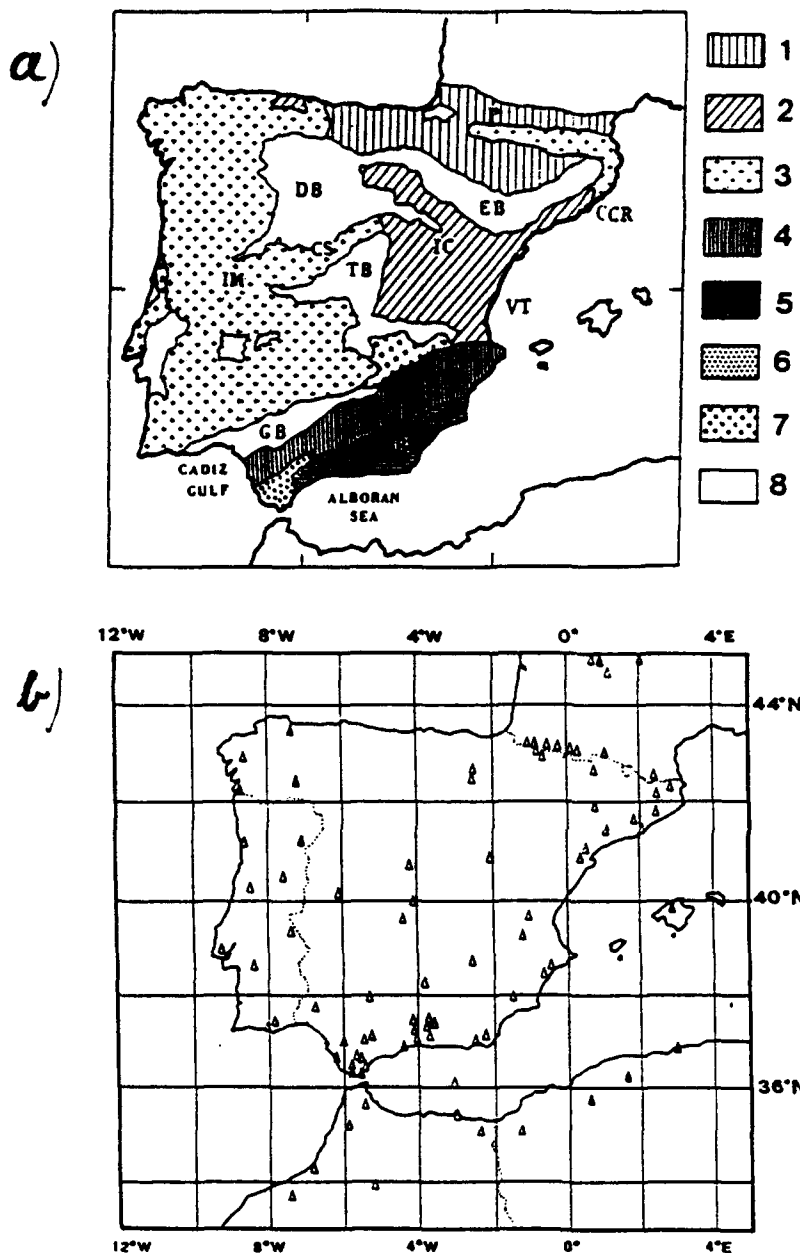


Figure 2.3.1: (a) Tectonic provinces comprising the Iberian continental area. Symbols are the following: 1. Deformed Mesozoic cover of the Pyrenees, 2. Mesozoic area, 3. Hercynian basement, 4. Mesozoic external units of the Betics, 5. Mesozoic and Paleozoic internal units of the Betics, 6. Intermediate Flysch of the Gibraltar arc, 7. Undeformed Mesozoic cover, 8. Tertiary basins. IM, Iberian Massif. P, Pyrenees. CCR, Catalan Coastal Range. IC, Iberian Cordillera. CS, Central System. B, Betics. DB, Duero Basin. TB, Tajo Basin. GB, Guadalquivir Basin. EB, Ebro Basin. VT, Valencia Trough. (b) Seismograph stations that reported readings used in the analysis. The Sonseca (ESLA) array is located at 39.67°N, 3.96°W.

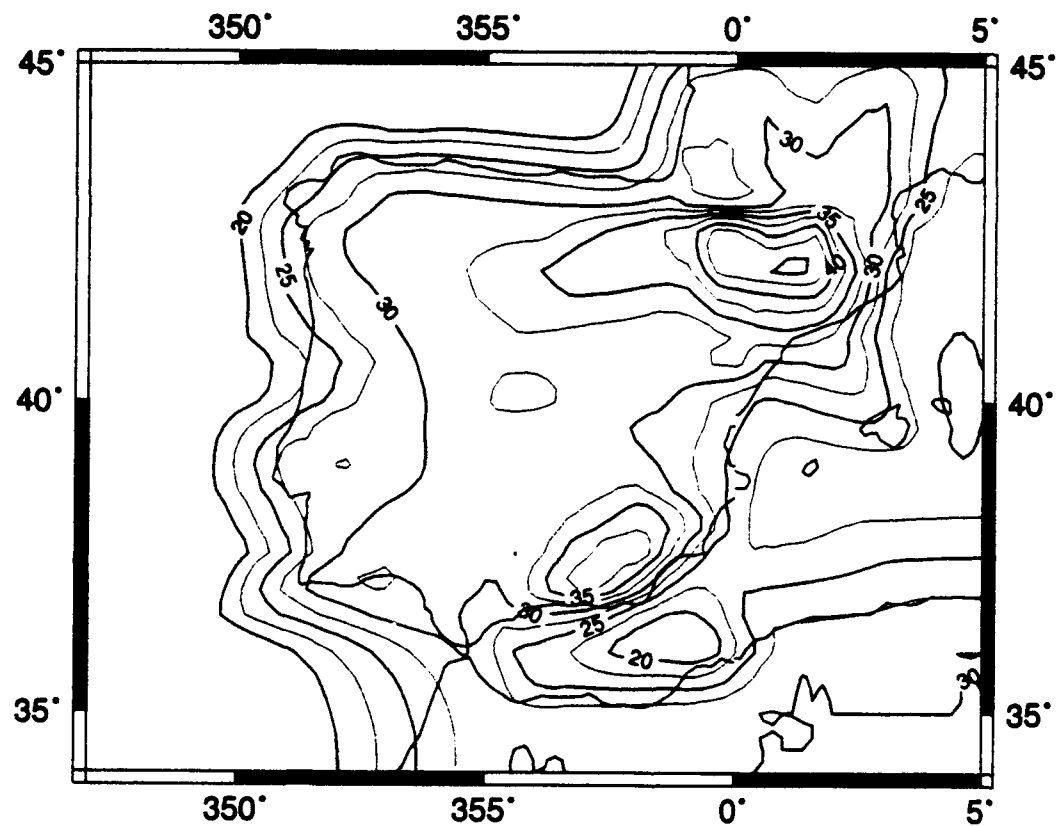


Figure 2.3.2: A model of Moho depth (in km) beneath the Iberian peninsula, gridded using GMT software (Smith and Wessel, 1990).

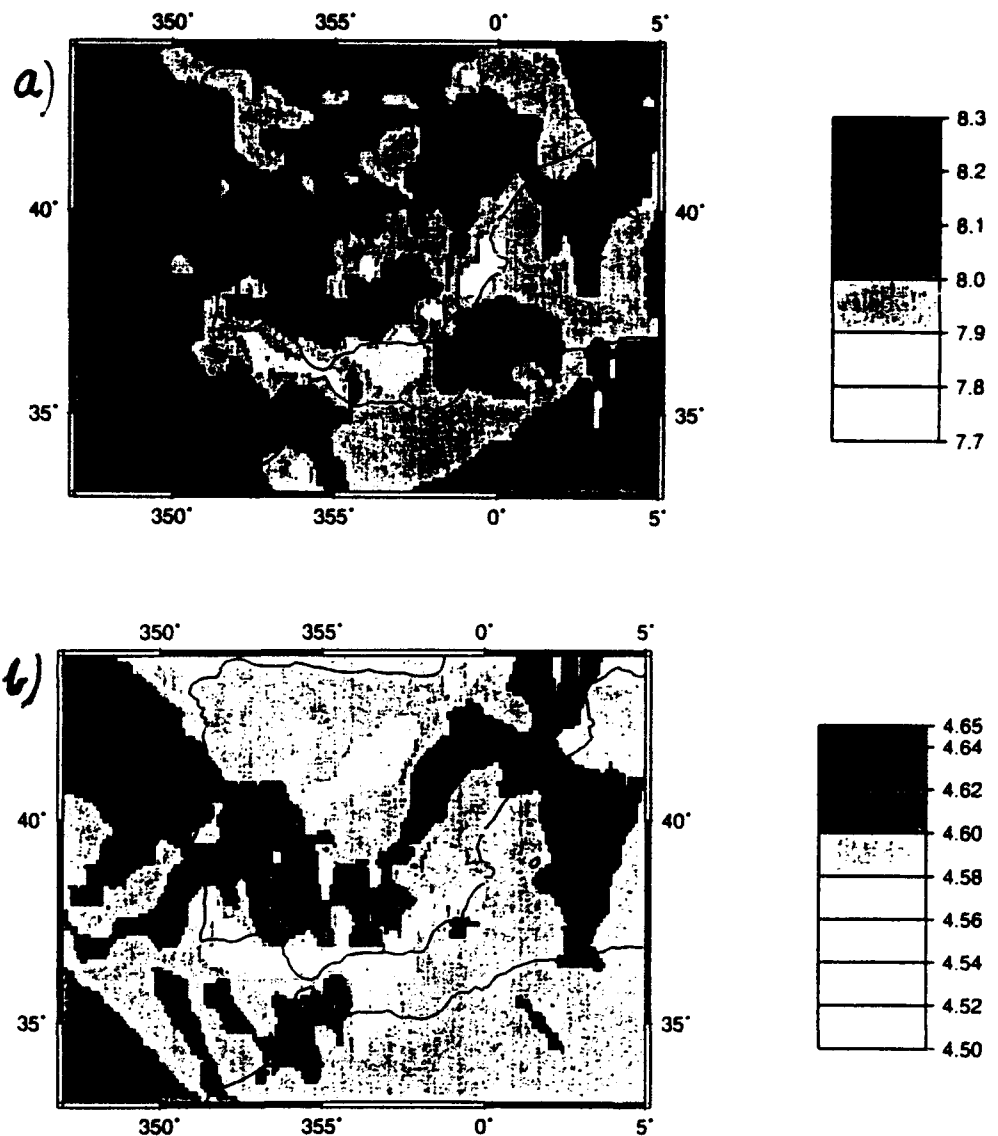


Figure 2.3.3: (a) Pn velocity distribution determined from inversion of the observed Pn arrival time data. Dark grey-scale represents high velocities, light shades represent low velocities, in km/s. (b) Sn velocity distribution.

## 2.4 Crustal modelling for 2D synthetics

Structural models used in synthetic seismogram analysis are often very simple in order to avoid awkward and computationally clumsy mathematical representations. On the other hand complex models could be generated from simple ones by introducing random perturbations in physical parameters like velocity and density or randomizing the topography of the free surface. Hestholm et al (1994) among others have used von Karman functions of various orders for simulating heterogeneous lithosphere models for 2D finite difference (FD) synthetic seismogram experiments. The results here are encouraging in the sense that models incorporating small scale velocity perturbations produce realistic seismograms including prominent coda wave features which are notoriously lacking for multilayered, homogeneous lithosphere models. In general, ray synthetics are not obviously related to prominent features in the wavefield recordings. We want to test the validity of this statement by computing synthetics for such multilayer crustal models including options for introducing perturbations of physical parameters as mentioned above. In other context we want to simulate wave propagation across prominent tectonic features like the Viking Graben in the North Sea which acts as a barrier for Lg-waves. The problem in common here is to generate the proper structural models in a simple manner. Our approach here is to avoid manual digitalization to the extent possible, hence our preference for using a optical scanner in combination with an interactive digitalization system. In addition we need a smart algorithm for automatically assigning grid point affiliations; we proceeded in the following manner.

- i. Figure, say taken from a publication, is prepared for the scanner like the MacIntoch canvas system with output (non-standard) in the form of x, y-coordinate values.
- ii. The output is modified in such a way that the model 'envelop' has a perfect rectangular form and that structural boundaries are vectorized being represented as a sequence of line segments. Scaling factors are incorporated and corrections introduced if horizontal and vertical scalings are different.
- iii. The next step in the analysis is to determine all closed face boundary curves which can be established from all boundary line segments at hand (step ii). For example, we may start in the lower right corner in Fig. 2.4.1 and proceed upwards; at the first line intersection we choose the leftmost anti-clockwise path, and so on until 'coming' back to the lower right corner. In this way we obtain all closed face boundary curves which in essence are envelopes for areal continuous structural elements constituting the lithosphere model. Note, if a structural element is completely embedded in a larger one, it is represented by two closed curves - anti-clockwise and clockwise respectively. Also, the rectangle encompassing the whole model is a closed curve in our representation. Note, since this process is automatic there is no formal structural element identification, except for a single 1 to N numbering of the closed curves determined.
- iv. The last and most tricky step was to introduce both a numerical element identification and in parallel tagging such a label to all the respective grid points contained within the proper closed boundary curve. Conventional mathematical geometry proved far to clumsy for solving this problem, but recalling a theorem from integral calculations in the complex number domain a simple solution was found. For each grid point, a horizontal branch line to the left was formed. Its intersections with the extremal curves ( $n_i$ ) would be even number for a point outside the close curve and an even number for a point inside. The identification

number (*IDENT*) of the structural element to which the grid point belongs would then be a sum of powers with base number of 2;

$$IDENT = \sum_{i=1}^N f(n_i)2^i \quad (1)$$

where *N* is the number of closed curves,  $f(n_i)$  is 0 for  $n_i$  even and 1 for  $n_i$  odd. Quite frankly, we were amazed over the very simple solution to the above rather tricky problem.

- v. The input file to the initial digitalization process contained a listing of physical parameters like velocity and density for each structural element/layer of the model. All this information is attached to a single point within each individual layer. When all the structural elements have been identified, it is easy to match the automatic layer labels (eq. 1) to the initial, deterministic ones.

The workings of the above digitalization procedure is demonstrated in Fig. 2.4.1. An added advantage with this approach is that input file errors in 2D FD model specifications are greatly reduced. The motivation for the above model digitalization venture was to compute synthetic seismograms for a large variety of lithosphere models. This implies that the subsequent analysis of synthetic recordings also must be handled in an efficient manner. Hence, the output seismograms are converted to SEG-Y formats and then subject to various kind of filtering, stacking, f-k, p-tau-analysis on a modern workstation like ProMAX. Also this task has been accomplished as demonstrated in Fig. 2.4.2.

Future plans using the above modelling system and subsequent waveform analysis tools, involve extended testing of deep crustal models derived from refraction and/or wideangle reflection profiling and to investigate barrier effects like the apparent blocking of the Lg-propagation across the Viking Graben in the North Sea.

*Yann Grondt*

*Eystein S. Husebye*

*Eirik B. Hanssen*

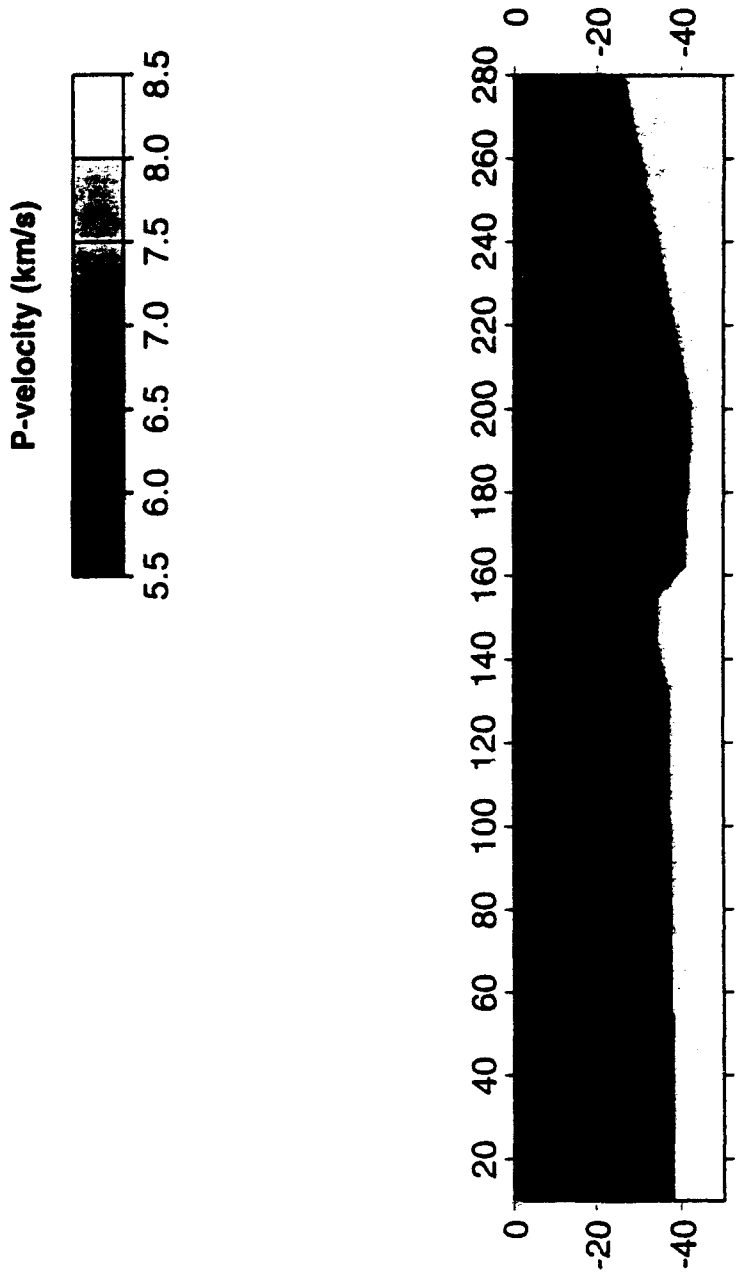
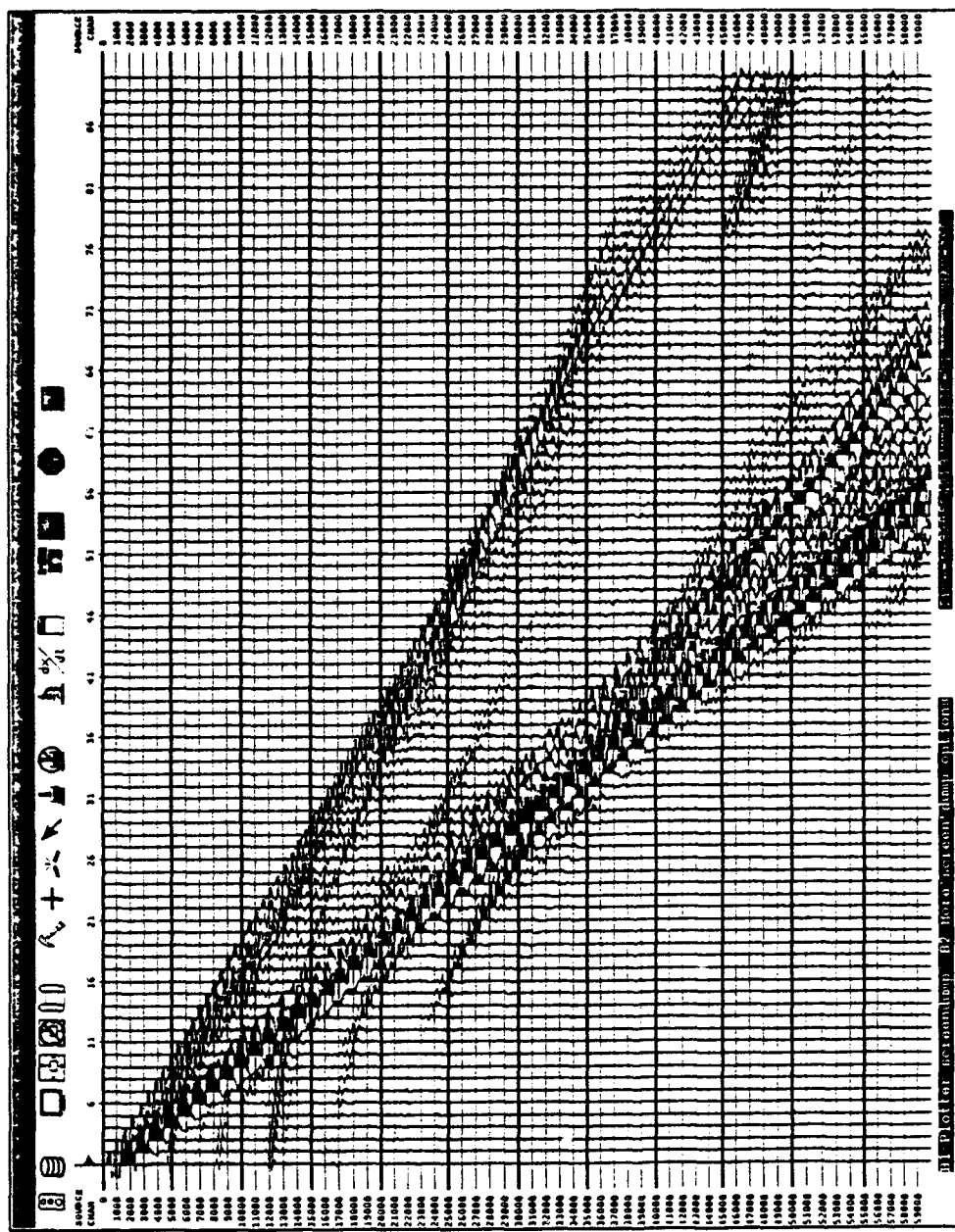


Figure 2.4.1: Model of P-wave velocity generated by the above procedure and used for 2D FD modelling. An explosion source was placed at 0.5 km depth at  $x=10$  km.



**Figure 2.4.2:** ProMAX screendump of synthetic seismograms generated for the model shown in Fig. 2.4.1. The receivers were placed with 3 km intervals in the range  $x=13$  to  $x=280$  km. Time axis is in msec.

### **3 Studies completed**

In this section we gives the abstracts for three papers recently completed with support from the present AFOSR Grant.

#### **3.1 Spatial and temporal patterns of the Fennoscandian seismicity – an exercise in explosion monitoring**

Matti Tarvainen, Institute of Seismology, P.O. Box 19, FIN-00014 University of Helsinki, Finland

Eystein S. Husebye, Institute of Solid Earth Physics, University of Bergen, Allégaten 41, N-5007 Bergen, Norway

##### **Abstract**

Fennoscandian stations and arrays detect daily numerous seismic event at local and regional distances. Almost all of these events stem from various kinds of explosions. Such explosion recordings are of little scientific value, but add considerably to the daily analyst workloads. Also in a test ban verification context is such recordings problematic because identification between chemical and nuclear explosions is not always obvious.

In this work we report on efforts to automate detection, location and classification of seismic recordings, stemming from local mining activities and other explosions. The first steps here are that of establishing a knowledge base on mining activities such as their locations, firing times, type of mining activity and which stations are most likely to report events from a given mining area. Using the comprehensive Helsinki Bulletin for 1991, the above mentioned parameters have been extracted from various parts of Fennoscandia and north-western Russia. Consistent diurnal, weekly and spatial patterns are typical for most of the seismic events included in the bulletin.

**Comments:** Mining and other kind of explosions account for 85 to 95% of the entries in the seismic bulletins for seismic stations, arrays and network operations in Fennoscandia. The costs and human efforts involved in proper analysis of these explosions are by no means modest, so the question arise whether this observational nuisance possibly could be handled in a more cost effective manner. For example, from Fig. 2 in the above study (Appendix A) we have that the explosion activity is concentrated to a few areas like the Estonian oil shale quarries, and Karelian and Kola mining operations. In other words, we try through cooperative efforts with Finnish and Russian scientists to ensure deployment of mobile seismograph equipments for a period of a few weeks within the mentioned mining areas. We would address the above cost efficiency problem through analysis of such data if available in the future.

### **3.2 2D finite difference elastic wave modeling including surface topography**

Stig O. Hestholm, IBM Bergen Environmental Sciences and Solution Centre, Thormølensgate 55, N-5008 Bergen, Norway

Bent O. Ruud, Institute of Solid Earth Physics, University of Bergen, Allégaten 41, N-5007 Bergen, Norway

#### **Abstract**

A 2D numerical finite difference algorithm accounting for surface topography is presented. Higher order, dispersion-bounded, cost-optimized finite difference operators are used in the interior of the numerical grid, while non-reflecting absorbing boundary conditions are used along the edges. A transfer from a curved to a rectangular grid achieves the modeling of the surface topography. Along the surface we use the free surface boundary conditions. To account for the surface topography is important for the complete modeling of the effects of wave propagation. Near-surface effects, such as scattering, are otherwise not modeled adequately. Even if other properties of the medium, for instance randomization, can improve numerical simulations, the inclusion of the surface topography make them more realistic.

**Comments:** Through studies of teleseismic events we have earlier found that scattering by surface topography is a major contributor to teleseismic P-coda. Also for regional and local events surface waves scattered by topography can be found in the low frequency part of the P- and S-coda. With the present method we are able to model such effects in 2D with little extra computational load compared to conventional FD methods. An extension to 3D is possible, but presently we are prohibited by limited computational capacity to do realistic 3D modelling.

### **3.3 Seismic wave propagation in complex crust – upper mantle media using 2D finite difference synthetics**

Stig O. Hestholm, IBM Bergen Environmental Sciences and Solution Centre, Thormølensgate 55, N-5008 Bergen, Norway

Eystein S. Husebye, Institute of Solid Earth Physics, University of Bergen, Allégaten 41, N-5007 Bergen, Norway

Bent O. Ruud, Institute of Solid Earth Physics, University of Bergen, Allégaten 41, N-5007 Bergen, Norway

#### **Abstract**

Synthetic seismogram analysis is considered an adequate tool for aiding in a better understanding of seismic wave propagation in the lithosphere. Our finite difference (FD) scheme has been used for computing synthetic seismograms for 2D crust/upper mantle models of size  $150 \times 400$  km $^2$  and with options for a free surface with topography. The research strategy was to introduce successively more complex lithosphere models for generating the synthetics; the reference model was a homogeneous lithosphere. The extent of interface scattering is visualized through displays of synthetic waveforms and snapshots for models with a corrugated Moho only and free surface topography only. The latter seems to dominate and in the form of P-to-Rg and S-to-Rg conversions at the surface. Lithosphere randomizations were introduced through von Karman functions of order 0.3, with RMS velocity fluctuations of 3-4 per cent and correlation distances (horizontal and vertical) at 2.5 or 10 km. In case of a medium with only sub-Moho heterogeneities, those with horizontal anisotropy ( $a_x = 10$  km;  $a_z = 2.5$  km) produced relatively strong Pn and Sn phases. The respective codas were dominated as in most of our experiments by P-to-S and S-to-S scattering wavelets excluding Rg-scattering at a free surface with topography. For a medium with crustal heterogeneities, the deformations of the P and S wavetrains with distance were clearly demonstrated. For full-scale heterogeneous lithosphere models, characteristics features of the synthetics were quantitatively similar to observational records of local events. Dominant attributes were a pronounced P coda consisting mainly of P and Rg-scattered wavelets, and a relatively strong S coda consisting mainly of P-to-S and S-to-S scattered wavelets. The P and S waveforms are severely deformed pointing towards the futility of reliably picking many secondary arrivals in local event recordings. Most of the scattering wavelets are confined to the crustal waveguide and to surface waves since coda excitations for sensors at a depth of 100 km were weak and besides consisted mainly of S wavelets. This implies that a strong teleseismic P coda does not reflect scattering within the crust in the source region but preferably a complex source function. Observational results from analysis of NORESS and ARCESS local event recordings are also presented. Clearly the lithosphere is not isotropically inhomogeneous. The essence of our 2D FD synthetic seismogram experiments is that a simple lithosphere model, being moderately heterogeneous, gives rise to complex seismograms which are grossly similar to the observational recordings. In contrast, complex models derived from profiling surveys (but lacking the fine scale random variations) give simple, 'ray tracing' like synthetics, not very similar to observational records.

#### **4 Future work plans**

The focus would be on seismic event classification and network monitoring capabilities. In the former case we would also explore the usefulness of broadband 3C seismometer recordings and to what extent SNR enhancement can be gained through optimum, adaptive filtering schemes. A motivating factor here is that inversion of low-frequency waveform data provide stable estimates of source parameters including focal depths.

The near on-line magnitude estimation scheme may prove helpful in automating seismic network operations. The availability of amplitude information is likely to improve phase identification for non-array stations and besides almost instantaneously provide estimates of test ban monitoring capabilities on local, regional and global levels.

Most of our knowledge bearing on crustal structures and compositions stem from refraction and wide-angle reflection surveys. A basic assumption here is that scattering and coda excitation mechanisms are ignored. We are planning to reexamine published results derived from such surveys in Iberia and Kola for a start by computing 2D FD synthetics using the original crustal models in comparison to similar models being subjected to random perturbations of the velocity and density parameters. Likewise, with the software tools at hand we would also examine the structural peculiarities acting as barriers to Lg-wave propagation say across the North Sea.

# **SPATIAL AND TEMPORAL PATTERNS OF THE FENNOSCANDIAN SEISMICITY - AN EXERCISE IN EXPLOSION MONITORING**

Matti Tarvainen  
Institute of Seismology,  
P.O. Box 19,  
FIN-00014 University of Helsinki,  
Finland

Eystein S. Husebye  
Institute of Solid Earth Physics,  
University of Bergen,  
Allégaten 41,  
N-5007 Bergen,  
Norway

## **ABSTRACT**

Fennoscandian stations and arrays detect daily numerous seismic events at local and regional distances. Almost all of these events stem from various kinds of explosions. Such explosion recordings are of little scientific value, but add considerably to the daily analyst workloads. Also in a test ban treaty verification context such recordings are problematic because identification between chemical and nuclear explosions is not always obvious.

In this work we report on efforts to automate detection, location and classification of seismic recordings, stemming from local mining activities and other explosions. The first steps here are that of establishing a knowledge base on mining activities such as their locations, firing times, type of mining activity and which stations are most likely to report events from a given mining area. Using the comprehensive Helsinki Bulletin for 1991, the above mentioned parameters have been extracted from various parts of Fennoscandia and north-western Russia. Consistent diurnal, weekly and spatial patterns are typical for most of the seismic events included in the bulletin.

## INTRODUCTION

The many recordings stemming from numerous quarry blasts, mining explosions and other man-made seismic events are a nuisance in seismograph network operations as their analyses add considerably to the daily workload of the analyst. In a nuclear test ban context an additional problem is that event classification is an important task and it is not always simple to distinguish between earthquakes and explosions. In recent years considerable progress has taken place in the field. Elaborate schemes based on so-called neural network techniques have been proved useful (Dowla et al. 1990; see also Tsvang et al. 1993). An alternative to such schemes is to look for distinct patterns and in particular whether signal attributes of associated seismic recordings are site specific. For example, Rivière-Barbier and Grant (1991) report that several Fennoscandian mines have prominent and consistent seismic signatures, although variability between even closely spaced mines (a few kilometers), could be large. The idea of using recording signatures for fast reliable event location and source type identification is not new in observational seismology and in fact is daily practiced in many observatories (e.g. see Vesalanen 1944). Simply, a skilled analyst can easily differentiate between many mining areas just by a quick glance on the relevant wave forms. An illustrative example here is that the Institute of Seismology, University of Helsinki, more than two decades ago introduced a template system of explosion master events to ease the daily analysis workload. Essential elements were à priori knowledge of specific mining activities and which explosions produced distinct and easily recognizable recording signals. The tabulation of this coding system, including the location of mining operation is given in Table 1. In practice, an analyst wave form recognition would suffice for assuming an explosion location for the event recordings in question. There is now a desire to change this well-proven but essential manual system in a view of the upgrading of the national Fennoscandian networks to digital recording and the general need for operational cost efficiency.

A recent approach to a non-analyst handling of the mining explosion problem is the evolutionary intelligent monitoring system (*IMS*) developed for automatic multiarrays data processing analysis (Bache et al. 1990, Bratt et al. 1990). Here satellite imagery information has been incorporated, providing information on mine locations (including quarries) and other types of large scale construction works. Such information has proved very useful in seismic bulletin work, since seismic epicenter locations at their best are accurate to the nearest 5-10 kilometers. This "spotting" method provides accurate epicenter solutions, which often are superior to those derived from conventional traveltimes observations. The mining and quarry sites obtained from satellite imagery pictures and

those of the old manual template system, as used at the Institute of Seismology, Helsinki, are shown in Figure 1a - the sites coincide well with each other. The stations in Fennoscandian network, which contributed data to this study is shown in Figure 1b.

In this paper the aim is to track the Fennoscandian mining and other explosion activity both in time and space on the basis of available bulletin data for the year 1991. The distribution of those events is shown in Fig. 2. Also, this is the first step in a larger research strategy, to discriminate and locate automatically and accurately regional seismic events from digital Fennoscandian seismograph stations.

## 2. OBSERVATIONAL DATA AND DOMINANT MINING AREAS

The data used in this study are event listings from Finnish seismological bulletins and from the so-called Nordic Seismological Data Base. The latter may be considered a regional bulletin as these event listings represent a merging of reports from the seismological observatories in Helsinki (Finland), NORSAR (Kjeller, Norway), Bergen (Norway) and the Russian Academy of Sciences, Kola Branch (Apatity). The Nordic data base at present is seemingly somewhat incomplete as numerous weak events detected and automatically located by the NORESS and ARCESS arrays are often missing. The epicenter solutions from these arrays are seemingly not officially released unless checked by the local analysts. Rather comprehensive listings for ARCESS and NORESS arrays are given by Rivière-Barbier (1993a, 1993b). Anyway, for the year 1991 altogether 4446 event reports were found in Helsinki bulletins (Uski et al. 1992), within the geographical region as defined in Fig. 2. Before plotting the events listings were prescreened for removing earthquakes and duplicate events. The latter are defined as events with an origin time difference less than 30 s and epicenter locations within 50 km of each other, but different reporting agencies. In the figure, the most striking feature is the numerous explosions in the Estonian oil shale quarries, from which 1419 events were reported in 1991. Other, prominent mining areas are Kiruna-Malmberget (northern Sweden), Russian Karelia, and the Kola district (NW Russia). Explosion activity at west-coast of Norway (Bergen) is tied to road and construction works, and hence has a more dispersed epicenter pattern. The prominent explosion areas were subject to more detailed analysis, presented below.

## **2.1. KIRUNA-MALMBERGET NORTHERN SWEDEN (Figures 3 - 6)**

The high columns in Figure 3 coincide with the Malmberget mine. There is also high mining activity in Kiruna. The explosion activity is relatively high and the shooting times are mainly in the afternoon and late evenings (Fig. 4). These are two distinct shooting intervals (Fig. 4), which may reflect different shooting practice at different mines. To see, if we could resolve this problem, the explosion locations were plotted for specific time intervals (Fig. 5). The majority of events occurring in afternoons can be connected to the Malmberget and Aitik mines while very early morning events are evidently explosions in the Kiruna mine.

The Kiruna-Malmberget mining operations are unique in the sense that reportings from the Swedish seismograph stations are lacking as shown in Fig. 6. This does not reflect poor station performances but instead a general lack of economical resources for daily analyst analysis of local (mining) seismic events. The mentioned non-reportings of the NORESS and ARCESS arrays are also obvious from the figure. In other words, the local event reporting practice between Nordic seismological observatories still vary considerably. As a rule of thumb the stations closest to seismic source areas should report many more events than far away stations, say along the west coast of Norway where besides the background noise is relatively high. So far, we have not tried to establish sort of seismic recording attributes (Joswig and Schulte-Theis 1993) differentiating between the various mining operations in the Kiruna-Malmberget, because the incomplete bulletin data are not convenient for doing so. However, the importance of this issue is obvious from Fig. 5.; the conventional epicenter locations are not always close to the known mining locations.

## **2.2 THE RUSSIAN KARELIA AND ADJACENT AREAS (Figures 7 -10)**

The mining activity here is large as demonstrated in Figure 7 and 8, where also Estonian oil shale quarry explosions are included. The seismic activity has been subject to special studies, e.g. Tarvainen (1992) concluded that on the basis of event locations tied to nearby 3-component station recordings it was impossible to separate individual mining operations (see also Bache et al. 1990). Mines identified via SPOT satellite images were found to be close to the epicenters (Fig. 8).

The diurnal shooting pattern for this area is rather distinct with a strong concentration in the afternoon hours on working days (Fig. 9). Explosion charges appear to be small since

the reporting frequency map in Figure 10 is dominated by Finnish stations (Helsinki agency). A few reports stem from Norwegian arrays and Russian stations.

### **2.3. KOLA PENINSULA AND ADJACENT AREAS (Figures 11-13)**

The seismic event locations reflect the diverse and extensive mining activities taking place in this area (Fig. 11). Again, there is a good diurnal clustering of events in the afternoon and there is an increased amount of explosions in weekends (Fig. 12).

Recordings of the Kola events stem mainly from the Finnish stations and the Helsinki Data Center (Fig. 13). More extensive studies of the Kola Peninsula seismicity are presented by Kremenetskaya (1991), Kremenetskaya and Trjapitsin (1992), and lately by Mykkeltveit (1993).

### **2.4. WESTERN NORWAY EXPLOSIONS (Figures 14-16)**

There is no mining operation in the area shown in Figure 14, but road and construction related explosions are numerous. 192 events occurred around Bergen out of which 46 were listed as earthquakes. This explains partly the dispersion of epicenters, but also, because there is no analyzed template system in use at the Bergen Observatory. The diurnal and weekly distribution of origin times is also relatively dispersed (Fig. 15), even though clear concentration at 15 hours on working days is clear. Most of the nocturnal events are earthquakes. The main part of detecting stations is located in western Norway (Fig. 16).

## **3. DISCUSSION**

The seismicity in Fennoscandia is very moderate with two or three earthquakes a week, equivalent to a few percents of our explosion data base for 1991. Even if teleseismic events are taken into account, the dominance of local explosions prevails, contributing 80-95% of the total event recording population at every station in this region. If all event records were subject to the same careful screening, about 90 per cent of the analyst workload would be tied to local explosion recordings of little or no scientific value. In practice such work allocations are not feasible over extended periods

of times at most seismological observatories. However, as most of the explosion epicenters are located in northern and eastern Fennoscandia, the excellent bulletin work performed at the Helsinki Data Center has in practice proved to be most beneficial for similar work at the other Nordic seismological centers. All event records from the stations in the coastal areas of Norway (Bergen Observatory) are carefully analyzed, but the number of recorded events is low due to a combination of high noise levels and also, relatively high signal attenuation for travel paths beneath the Caledonian mountain range. NORESS and ARCESS produced automatic bulletins in 1991, but their event listings were, as mentioned, only occasionally included in the Nordic bulletins.

The major outcome of our study of the Fennoscandian seismicity for 1991 is that the event population is completely dominated by numerous mining, quarry and other explosions. Such industrial operations are often stationary in space, and as demonstrated exhibit well defined temporal patterns. The former feature is not always obvious from the bulletin data as illustrated in Fig. 5 for the Kiruna-Malmberget mining district. Note, that most of these event locations, do not stem from the national Finnish bulletins, but from readings of stations in northern Norway. Anyway, the issues of incorporating well-established seismicity information and stationary signal attributes are of particular importance for automatic seismic network operations. The observational data at hand are often less voluminous and less reliable than those extracted through analyst inspections of station records (Ruud and Husebye 1992, Ruud et al. 1993). As mentioned above, formal epicenter solutions could be unreliable when based on P-arrival times only due to odd network configurations. The kind of seismicity information to be incorporated will naturally be spatial and temporal characteristics of mining operations. For example, being confident that given event recordings stem from a specific mine, the coordinates of that mine should replace the formal, seismic epicenter solution.

Another seismicity parameter of interest is station detectability, that is which stations are most likely to record explosions from a specific mine. Unfortunately, the bulletin listings are as mentioned incomplete on this account, so we only plotted the event reporting frequency for those stations and agencies, for which data were available (Figs. 6, 10, 13 and 16). Notice that the dominance of reportings from Helsinki, reflects the extensive usage of the template system in Finland and does not refer to a particular station. This kind of information would be useful for detecting phase association errors; for example western Norway stations are unlikely to detect mining explosions in the Kola and Karelian areas. Moreover, most of the Fennoscandian mining explosions are small magnitude ( $M_L < 2$ ) events and seldom recorded beyond distances of a 4-500 km (Figs. 6, 10, 13 and 16; Ruud and Husebye 1992).

To use signal attributes in automatic seismic network operations require waveform stationarity for a given station for a specific mine. This appears often to be the case in Fennoscandia so the challenge here is to mimic analyst template operation numerically. The mentioned elaborated IMS-system (Bache et al. 1990, Bratt et al. 1990, Bache et al. 1993) has provisions for implementing such features and also learning abilities useful solutions to the above kind of "artificial intelligence" (AI) problems have proved difficult in practice. Anyway, basic requirements here are compilation of reference events for every station in the network, and that the initial of epicenter location is accurate (Rivière-Barbier and Grant 1993). Besides, no network can be operated fully automatic in terms of producing high-quality bulletins, simply because signal attributes for weak events would be unreliable due to noise contamination.

#### 4. SUMMARY REMARKS

We have in this study examined the seismic aspect of the mining activities and other in Fennoscandia, which are characterized by clear temporal and spatial patterns. Analysts in Helsinki have taken full advantage of such knowledge so as to significantly ease the daily work load.

With digital seismograph networks being deployed in various parts of the region the challenge is to teach our computers to locate reliably, and identify the many thousands of explosions being recorded annually. This would require much painstaking work, since surprisingly little detailed information is available on many mining operations in particular in north-western Russia, but also elsewhere (short term construction works). However, we feel confident that this kind of problem can be solved using robust "grid search" techniques for incorporating *a priori* seismicity knowledge of the kinds dealt with here. The difficult problem is to mimic numerically the analyst's ability to quickly recognize mine specific waveforms. This implies that signal attributes are spatially stationary, which is often the case (Rivière-Barbier and Grant, 1993).

Observationally seismology has progressed tremendously over the last decade in terms of station design and deployment, digital recording, satellite communication and advanced data center facilities in various countries. A paradox in this context is the scant attention paid to the pressing problem of automatic signal analysis and bulletin production. With a few exceptions too small efforts are invested in this most essential aspect of network operation and earthquake monitoring.

## **ACKNOWLEDGMENTS**

We are grateful to the analysts Maija Franssila, Liisa Mustila, Eva Pelkonen and Merja Raime of the Institute of Seismology, University of Helsinki, Finland for the tedious analysis work and to Ms. Marja Uski for taking care of the Nordic database at the Institute of Seismology and making it available for this study. We express our gratitude to Dr. F. Rivière-Barbier (CSS; Washington D. C) for sharing her Fennoscandian mining locations with us and a reprint of her 1993 reports. The work reported here was financially supported by the Air Force office of Scientific Research, USAF under the Grant F49620-92-5-0510 (E.S.H) and Contract F49620-89-C-0038 (E.S.H) and the Finnish Academy of Sciences and Letters Väisälän rahasto (M.T.). We also acknowledge many useful comments from an anonymous reviewer.

## REFERENCES

- Bache, T., S. T. Bratt, J. Wang, R. M. Fung, C. Kobryn and J. W. Given, (1990). The intelligent monitoring system. Bull. Seism. Soc. Am. **80**, 1833-1851.
- Bache, T. C., S. R. Bratt, H. J. Swanger, G. W. Beall and F. K. Dashiell, (1993). Knowledge-based interpretation of seismic data in the intelligent monitoring system. Bull. Seism. Soc. Am. **83**, 1507-1526.
- Bratt, S., H. J. Swanger, R. J. Stead, F. Ryall and T. C. Bache, (1990). Initial results from the intelligent monitoring system. Bull. Seism. Soc. Am. **80**, 1852-1873.
- Dowla, F., S. Taylor and R. Anderson, (1990). Seismic discrimination with artificial neural networks preliminary results with regional spectral data. Bull. Seism. Soc. Am. **80**, 1346-1373.
- Joswig, M. and M. Schulte-Theis, (1993). Master-event correlations of weak local earthquakes by dynamic waveform matching. Geophys. J. Int. **113**, 562-574.
- Kremenetskaya, E. O., (1991). Contemporary seismicity of the NW part of the USSR, Semiann. Tech. Summ., 1 April - 30 September 1991, NORSAR Sci. Rep. 1-91/92, Kjeller, Norway
- Kremenetskaya, E. O. and V. M. Trjapitsin, (1992). Induced seismicity if the Khibiny Massif (Kola Peninsula), Semiann. Tech. Summ., 1 April - 30 September 1991, NORSAR Sci. Rep. 1-91/92, Kjeller, Norway
- Mykkeltveit, S., (1993). Mining explosions in the Khibiny Massif (Kola Peninsula of Russia) recorded at the Apatity three-component station, RNF/NORSAR Tech. Rep., Kjeller, Norway; pp. 27.
- Rivière-Barbier, F. and L. T. Grant, (1991). Cluster analysis of closely spaced mining blasts as a method of event location. Presented at the AGU 1991 fall meeting, San Fransisco, California, USA, 9-13 December 1991.
- Rivière-Barbier, F., (1993a). Constructing a reference event list for ARCESS: Sci. Rep. No. C93-03, Center for Seismic Studies, Arlington, Va., USA; 196 pp.
- Rivière-Barbier, F., (1993b). Constructing a reference event list for NORESS: Sci. Rep. No. C93-06, Center for Seismic Studies, Arlington, Va., USA; 88 pp.
- Rivière-Barbier, F. and L.T. Grant, (1993) Identification and location of closely spaced mining events. Bull. Seism. Soc. Am. **83**, 1527-1546.
- Ruud, B. O. and E. S. Husebye, (1992). A new three-component station detector and automatic single station bulletin production. Bull. Seism. Soc. Am. **82**, 221-237.

- Ruud, B. O., C. D. Lindholm and Husebye, E.S., (1993). An exercise in automating seismic record analysis and network bulletin production, Bull. Seism. Soc. Am. 83, 660-679.
- Tarvainen, M., (1992). Monitoring and analyzing regional seismic events using a network of three-component stations. Geophysica 27(1-2), 63-78.
- Tsvang, S.L., V.I. Pinsky and E.S. Husebye, (1993). Enhanced seismic source discrimination using NORESS recordings from Eurasian events, Geophys. J. Int. 112, 1-14.
- United States Delegation, (1992). Location calibration of mining explosions preliminary results, GSE/US/73, Geneva, March 1992.
- Uski, M., E. Pelkonen, M. Franssila and M. Raime, (1992). Seismic events in northern Europe (Helsinki Bulletin). Institute of Seismology, University of Helsinki, Report series R, Yliopistopaino (University of Helsinki Press).
- Vesanen, E., (1944). Über die typenanalytische Auswertung der Seismogramme, Ph. D. Thesis, Annales Academiæ Scientiarum Fennicæ, Helsinki; 244 pp.

**Table 1**

The Helsinki analyst template system; latitude and longitude of the operation. If known, the corresponding name of the mine is given.

<b>Mines and explosion sites in Estonia and Russian Karelia</b>					
Latitude	Longitude	Name of mine	Latitude	Longitude	Name of mine
59.24	24.33		59.41	24.59	
59.5	25.0		59.33	27.27	
59.33	27.07		59.27	27.73	
59.24	27.83		59.31	27.63	
59.3	27.5		59.37	28.53	
59.45	26.49		60.0	29.9	
60.02	29.74		59.6	30.0	
59.37	28.43		59.36	28.37	
61.01	29.04		60.90	29.35	
60.8	29.3		60.95	29.18	
61.1	30.3		61.5	30.4	
61.4	31.6		60.7	29.0	
61.4	34.3		61.9	30.6	
61.14	29.87		62.2	34.3	

64.68	30.66	Kostamuksha open pit	60.6	29.2	
60.7	28.7		60.8	29.5	

### Norwegian mines

Latitude	Longitude	Name of mine	Latitude	Longitude	Name of mine
58.30	6.40	Titania	69.6	29.9	Bjørnavatnet

### Mining sites on Kola Peninsula and adjacent areas

Latitude	Longitude	Name of mine	Latitude	Longitude	Name of mine
67.67	33.74	Kirovsk	67.63	33.84	Rasvumschorr
67.64	34.02	Koashva	67.64	33.88	Tsentralnju
69.4	33.18	Zapoljarnju	68.16	33.18	Olenogorsk
67.6	34.2		69.6	32.2	
67.7	31.4		67.56	30.44	Kovdor
69.3	34.4		69.2	34.7	
68.87	33.03	Murmansk	69.23	33.17	

### Mines in Northern Sweden

Latitude	Longitude	Name of mine	Latitude	Longitude	Name of mine
67.18	20.67	Malmberget	67.12	20.90	Aitik

67.8	20.2	Kiruna	67.7	21.0	Svappavaara
------	------	--------	------	------	-------------

**Mines and explosions sites in Finland**

Latitude	Longitude	Name of mine	Latitude	Longitude	Name of mine
60.17	23.84	Mustio	61.33	23.03	Stormi
60.30	22.29	Parainen	61.9	21.5	Otamo
61.6	21.7	Kritiskeri	62.07	27.41	Ankele
63.12	27.72	Siilinjärvi	64.12	28.06	Lahnaslampi
64.1	24.7	Perkköö	62.83	29.25	Horsmanaho
63.66	26.05	Pyhäsalmi	62.8	22.9	Törnävä
63.16	27.99	Nilsia	63.0	26.8	Talluskanava
55.78	24.70	Elijärvi	63.85	25.05	Hitura
61.64	24.26	Orivesi	61.94	29.03	Ruokojärvi

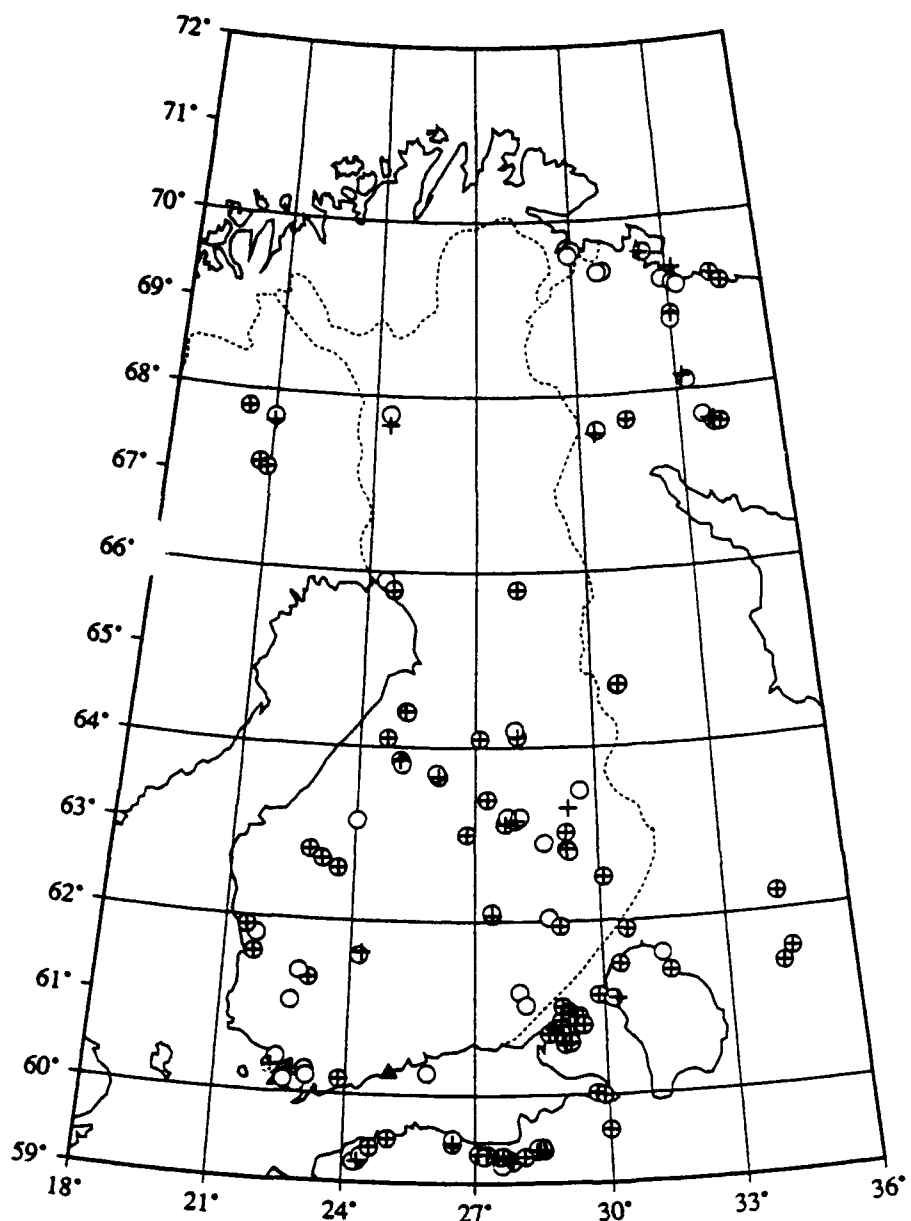


Fig. 1a .The mining sites in Fennoscandia according to the analyst template system in use at the Institute of Seismology, University of Helsinki (circles) and intelligent monitoring system (IMS) based on satellite imagery (crosses; F. Rivière-Barbier 1993a). These locations overlap nicely. The triangle shows the location of Helsinki data center.

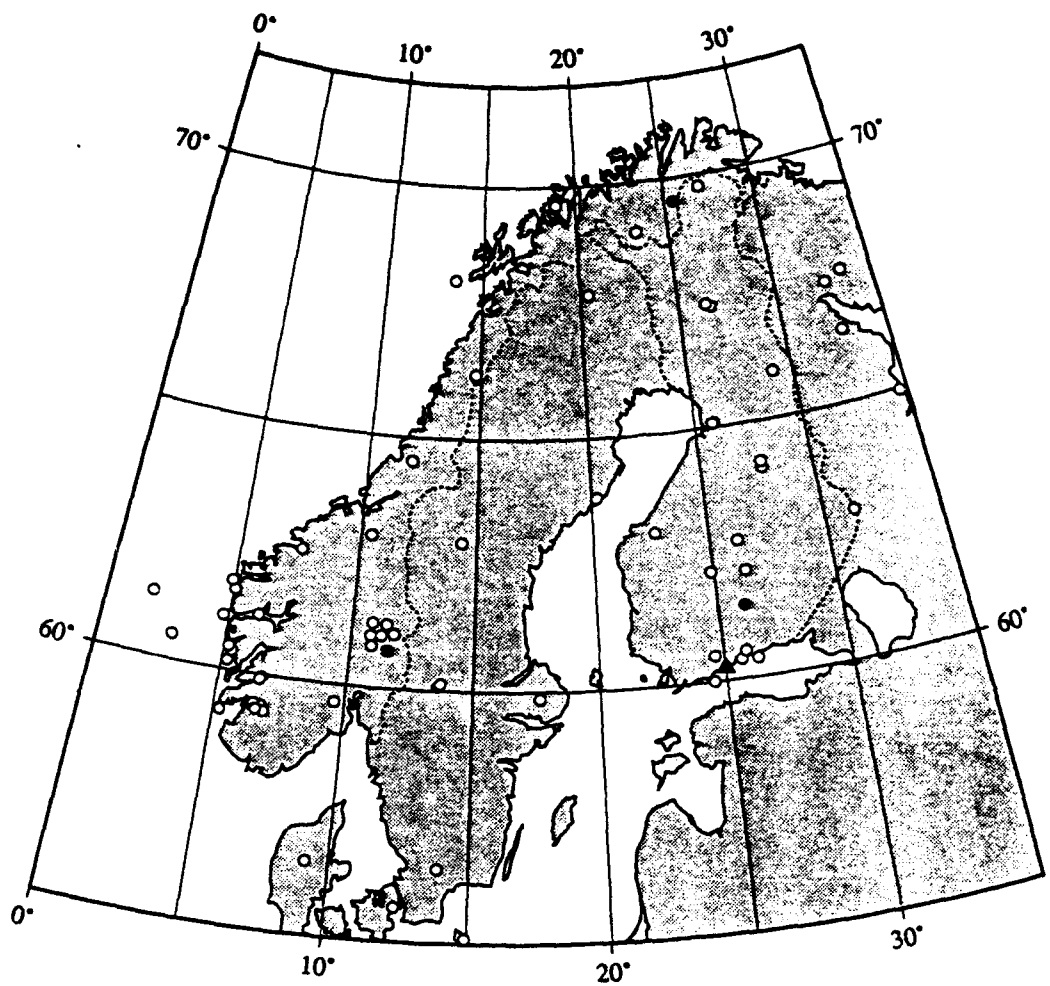


Fig. 1b. Fennoscandian seismograph stations reporting events in this study. The Helsinki data center is shown by a triangle.

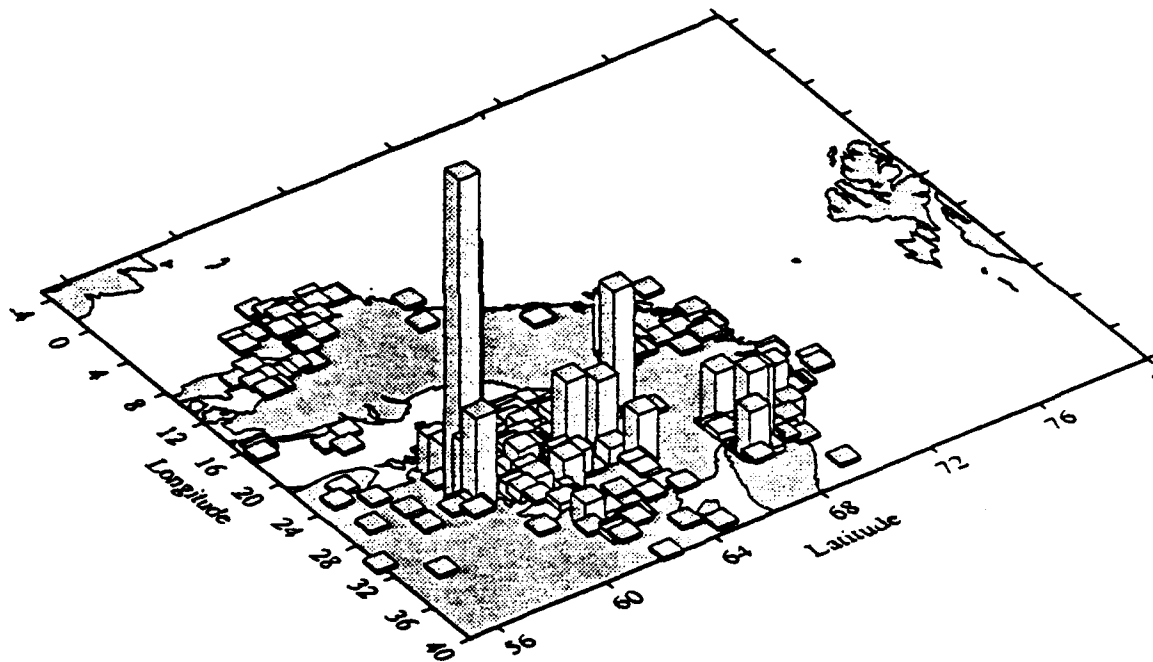


Fig. 2. Seismic events of presumed explosion origin in Fennoscandia in 1991 according to the Nordic Bulletin issued by the Finnish National Data Center (FNDC). The size of a column is  $1^\circ \times 1^\circ$ . The highest activity is on the Estonian coast, where many oil shale quarries are located. The highest column in the area represents 145 events. The total number of explosions for the Estonian mining operations was 1419 in 1991. Also, in northern Sweden, western Norway, Russian Karelia and Kola the explosion activities are high. Most events in Finland stem from mines, quarries and construction work sites.

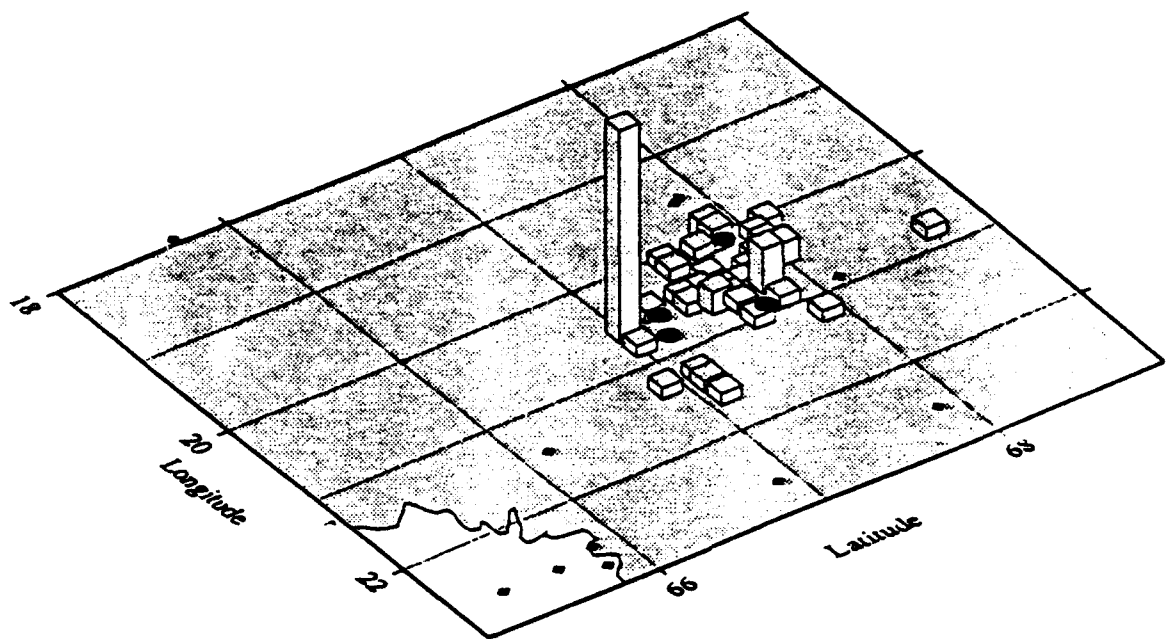
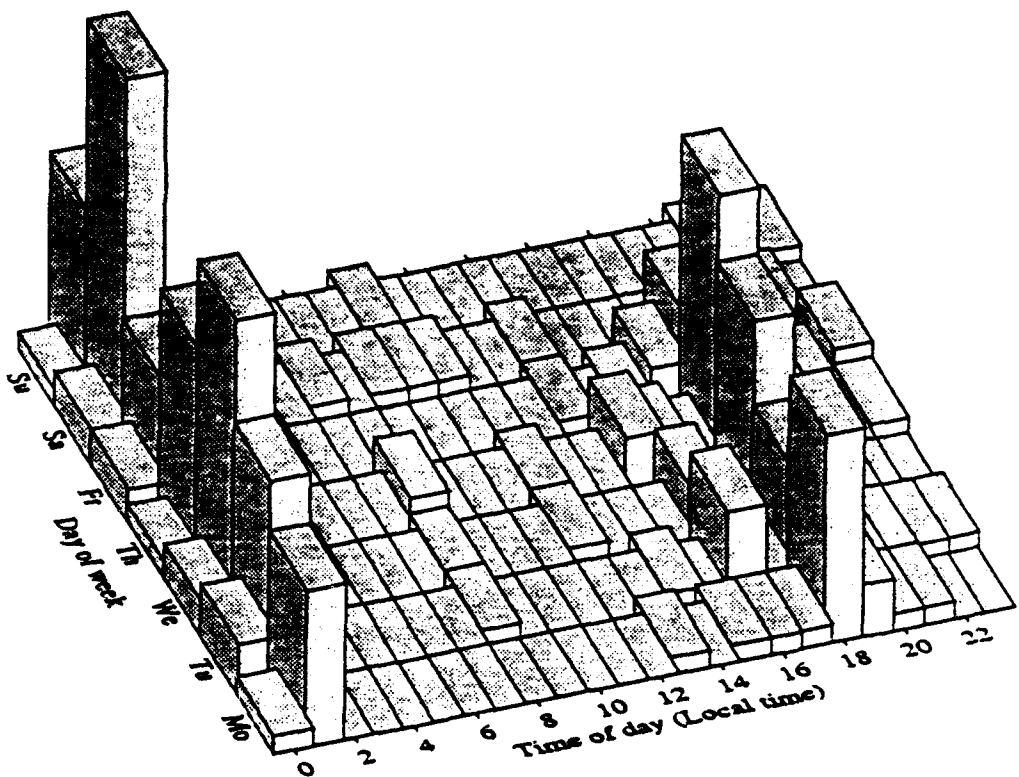
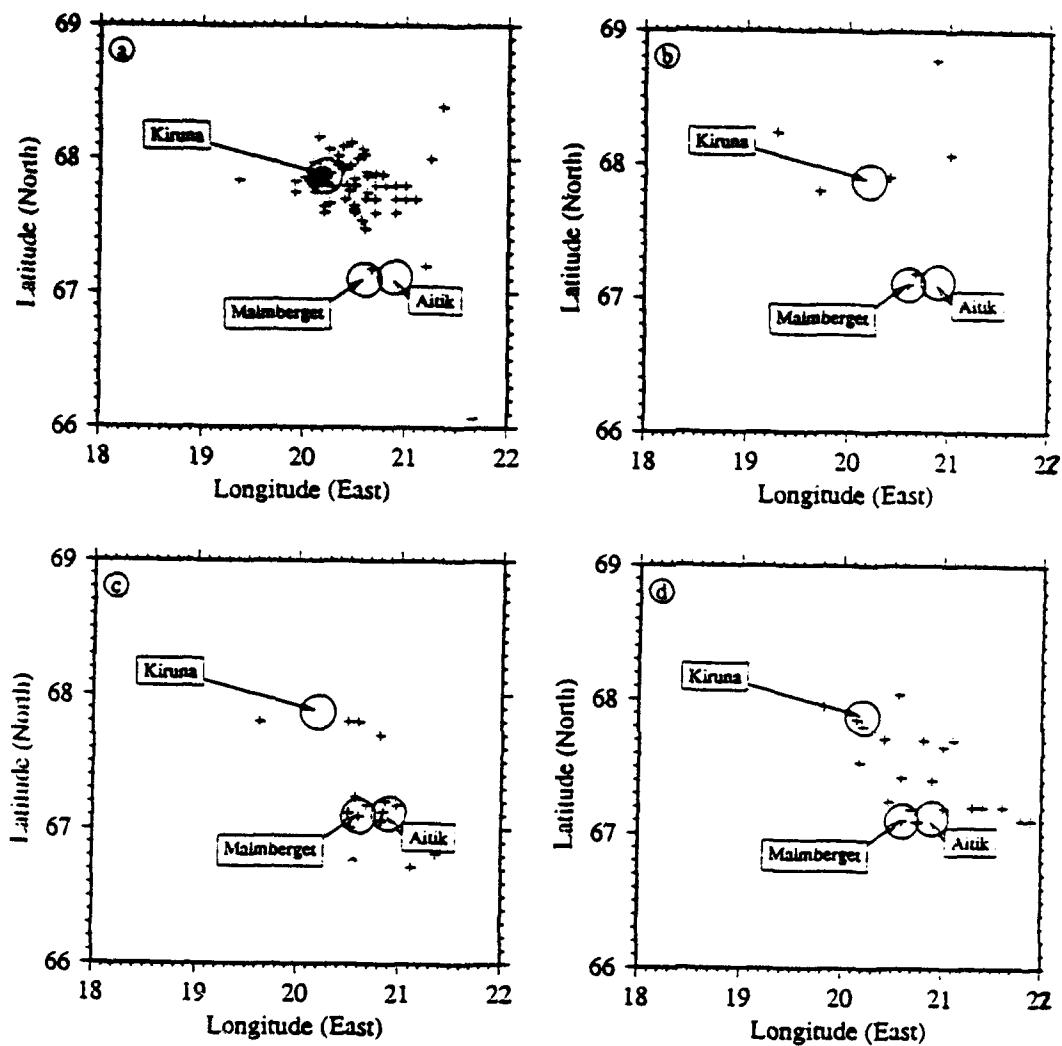


Fig. 3. Events in Kiruna-Malmberget region northern Sweden, in 1991. The mine sites are shown by black dots. The black diamonds signify small earthquakes. The column size is  $0.1^\circ \times 0.1^\circ$  and the highest column represents 26 events. The total number of events in the area was 212 including 11 earthquakes.



**Fig. 4.** Daily and weekly distribution of seismic events in northern Sweden. The majority of events occurs on working days early in the morning (local time). Daytime saving time from spring to early autumn is taken into account. Afternoon is the time of mining explosions in Aitik and Malmberget. The Kiruna mining explosions occur daily (peak on Saturday mornings). The highest column is equivalent to 22 events.



**Fig. 5. Distribution of explosions in northern Sweden for different diurnal time intervals . The day is divided into four intervals of six hours. The shooting practice in the Kiruna mine (Fig 5a) is clearly different from that in the other mines of the area.**

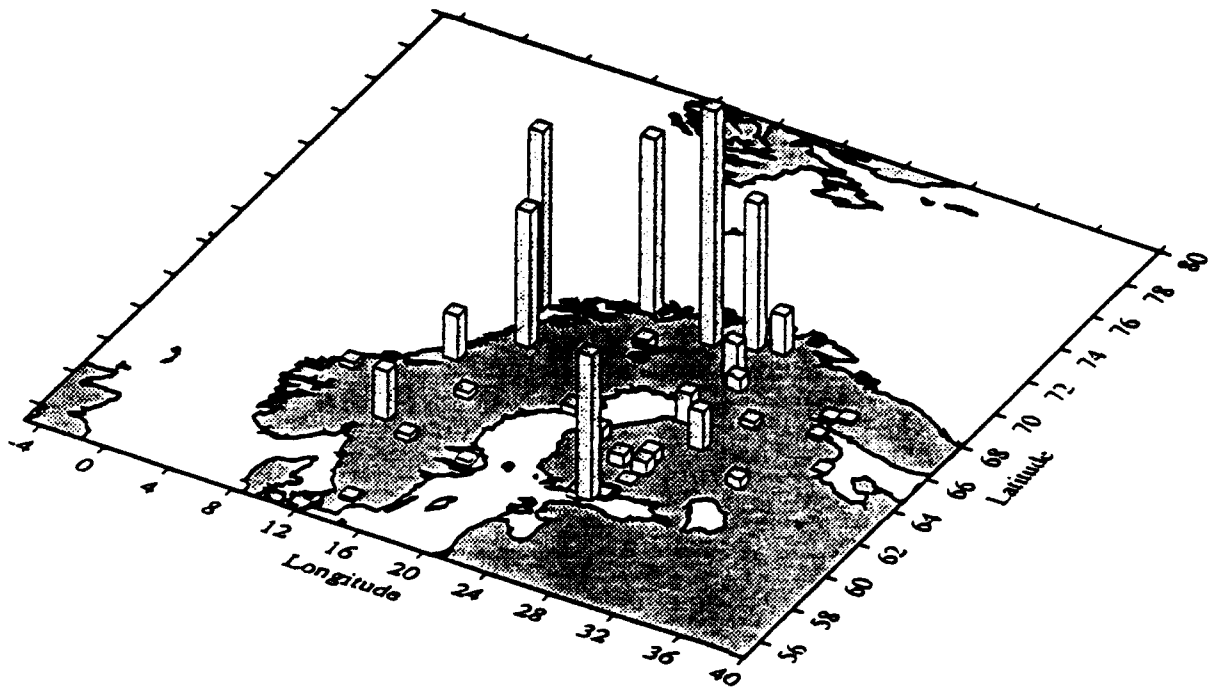


Fig. 6. Event reporting frequencies for agencies and stations in Fennoscandia and Russia of explosions in northern Sweden. The Helsinki Data Center and stations in northern Norway had the highest reporting rates of the events, but without identifying individual detecting stations. The mine locations are plotted as black dots.

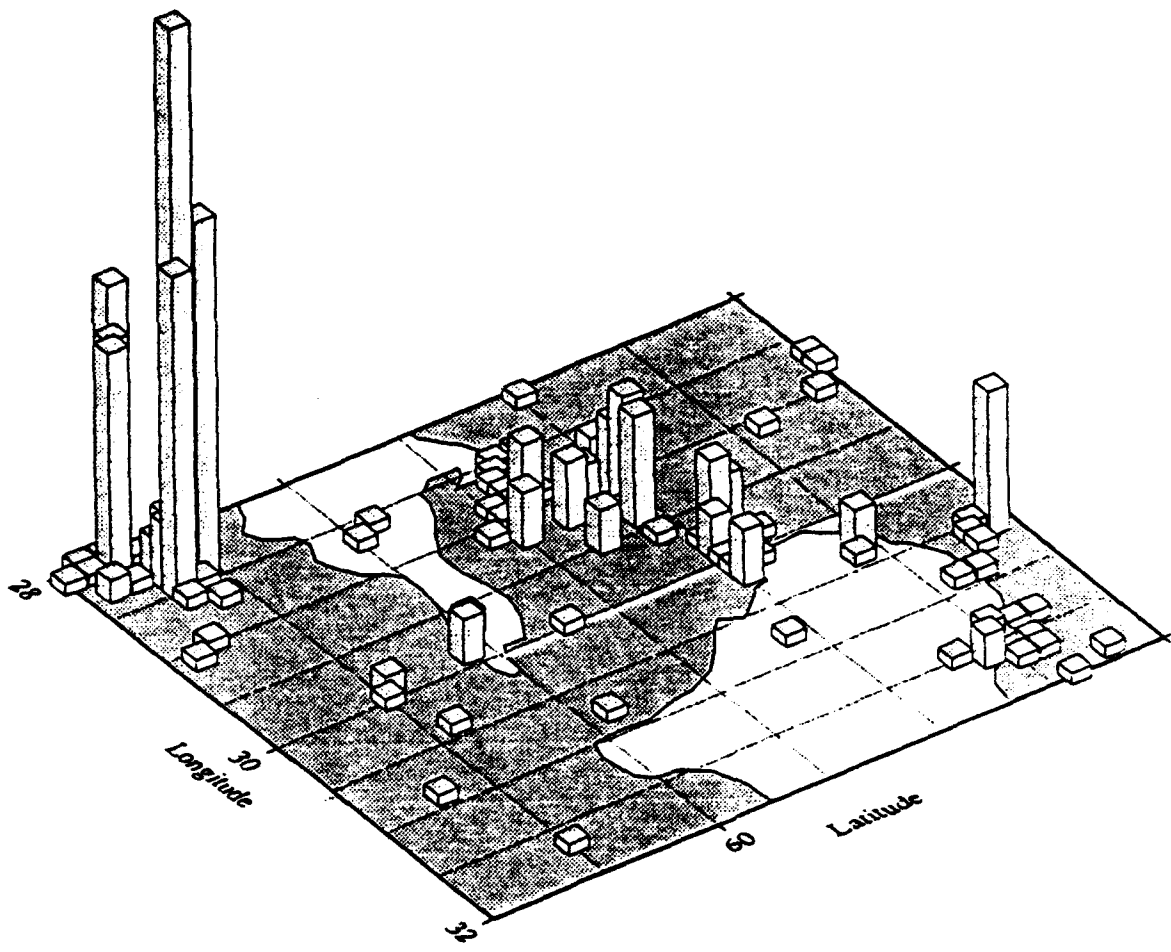


Fig. 7. Events in Russian Karelia in 1991 and adjacent areas. The column size is  $0.1^\circ \times 0.1^\circ$ . The sites of highest activities match well with mining locations seen on satellite imagery data (GSE/US/73). The outstanding feature is the many explosions in the oil shale mines in eastern Estonia, which for purpose of comparison were included. The highest column here represents 51 events. The number of events within the mapping area was 488.

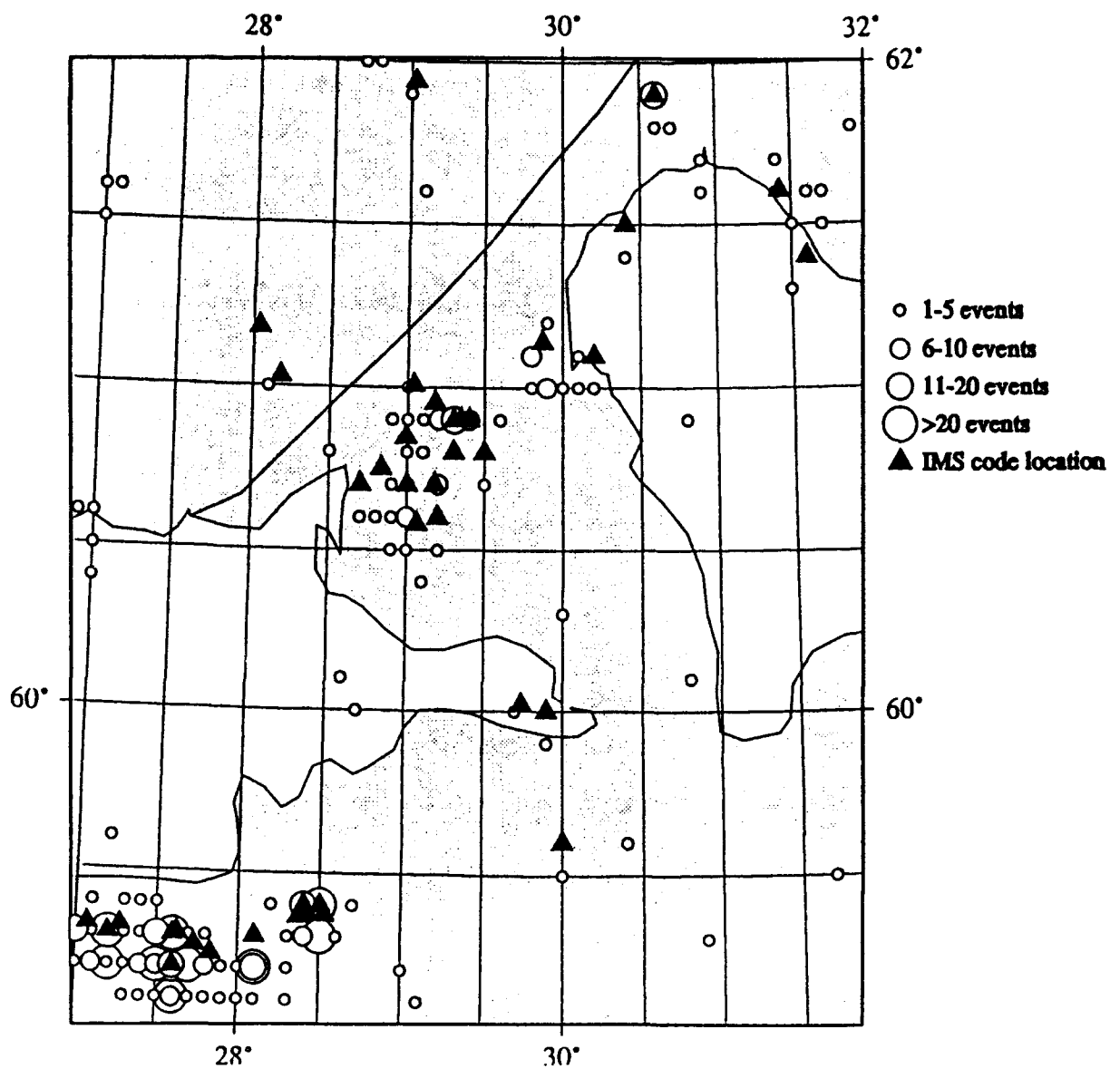


Fig. 8. The events of Fig. 7 shown together with SPOT located mining sites.

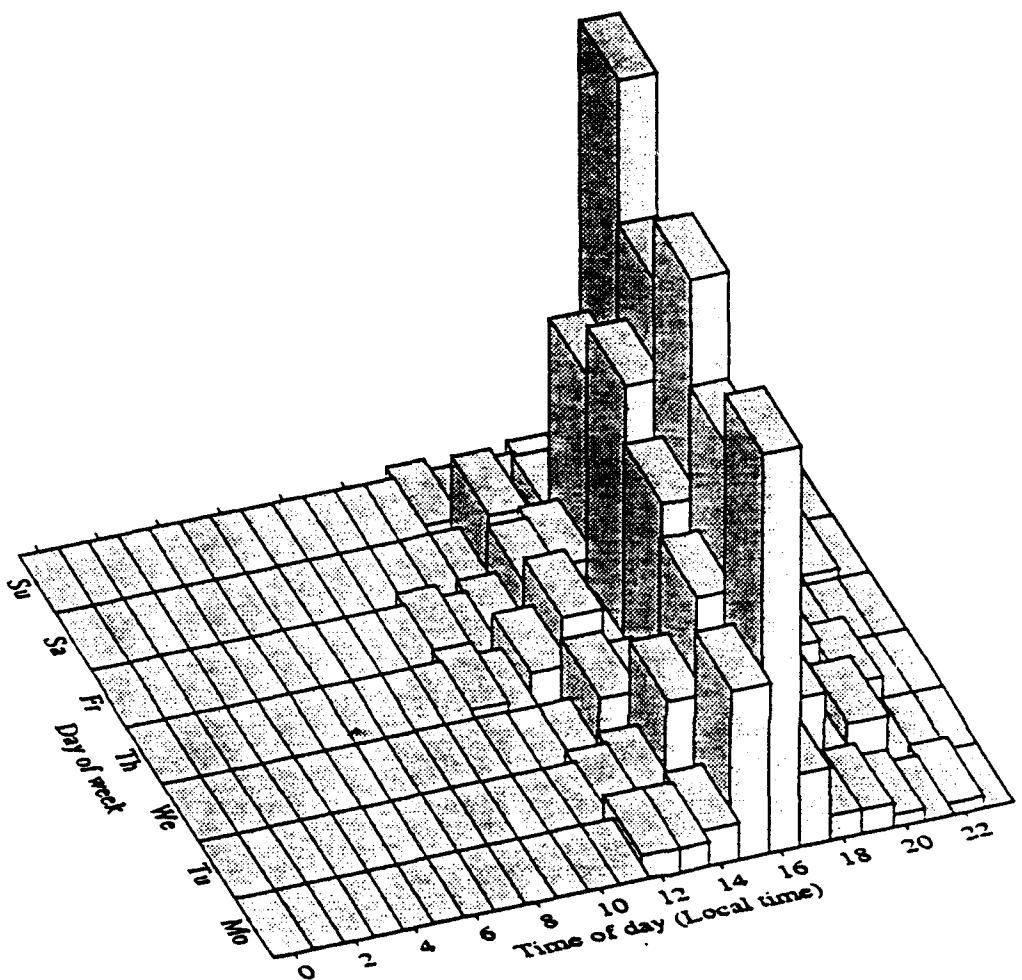


Fig. 9. Diurnal and weekly distribution of seismic events in the Russian Karelia and adjacent areas. They are evidently mining and other industrial explosions with shooting during prime working hours and afternoons. The activity is slightly higher on Fridays.

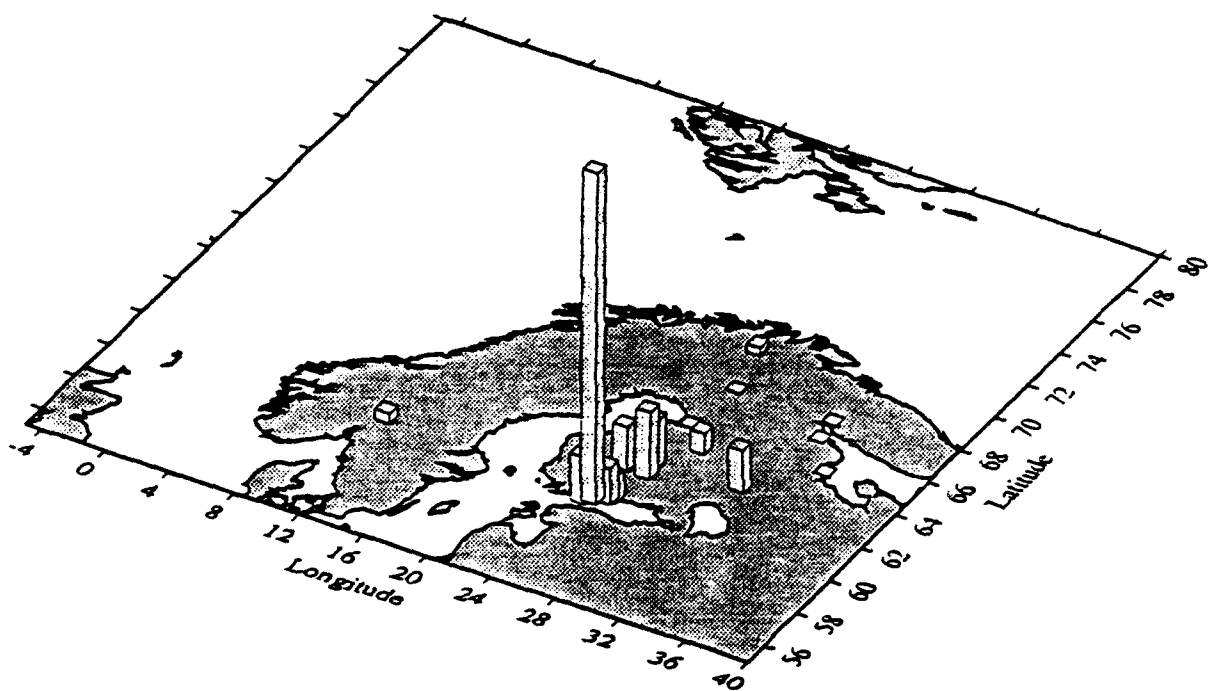


Fig. 10. Event reporting frequencies for agencies/stations of explosions in Russian Karelia. The Finnish stations, most of which are within 300 km exhibited the best monitoring capabilities. The column height at the Helsinki Data Center represents 416 events, which is close to 86% of all the events in the area in 1991.

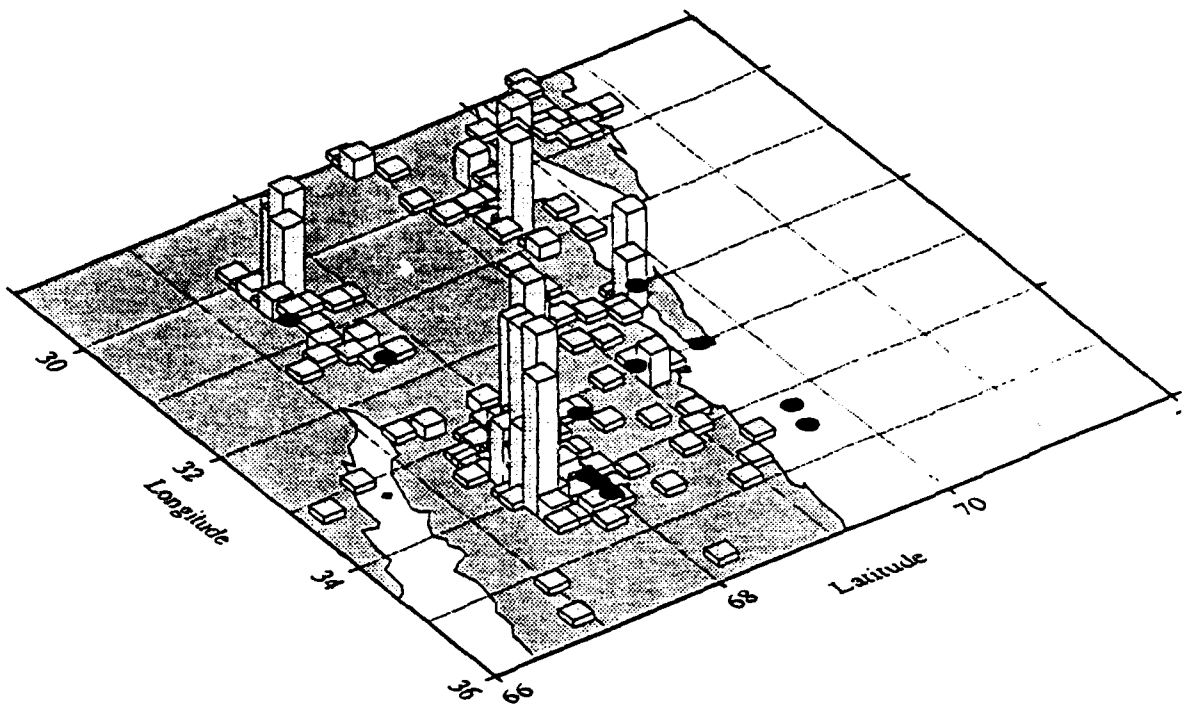


Fig. 11. Events on Kola Peninsula and adjacent areas. See Fig. 3 for symbols. The highest concentrations occurred near known mining sites (black dots). The total number of events in the area was 780 for the year 1991. The highest column represents 38 events. The few occurring earthquakes are marked by black diamonds.

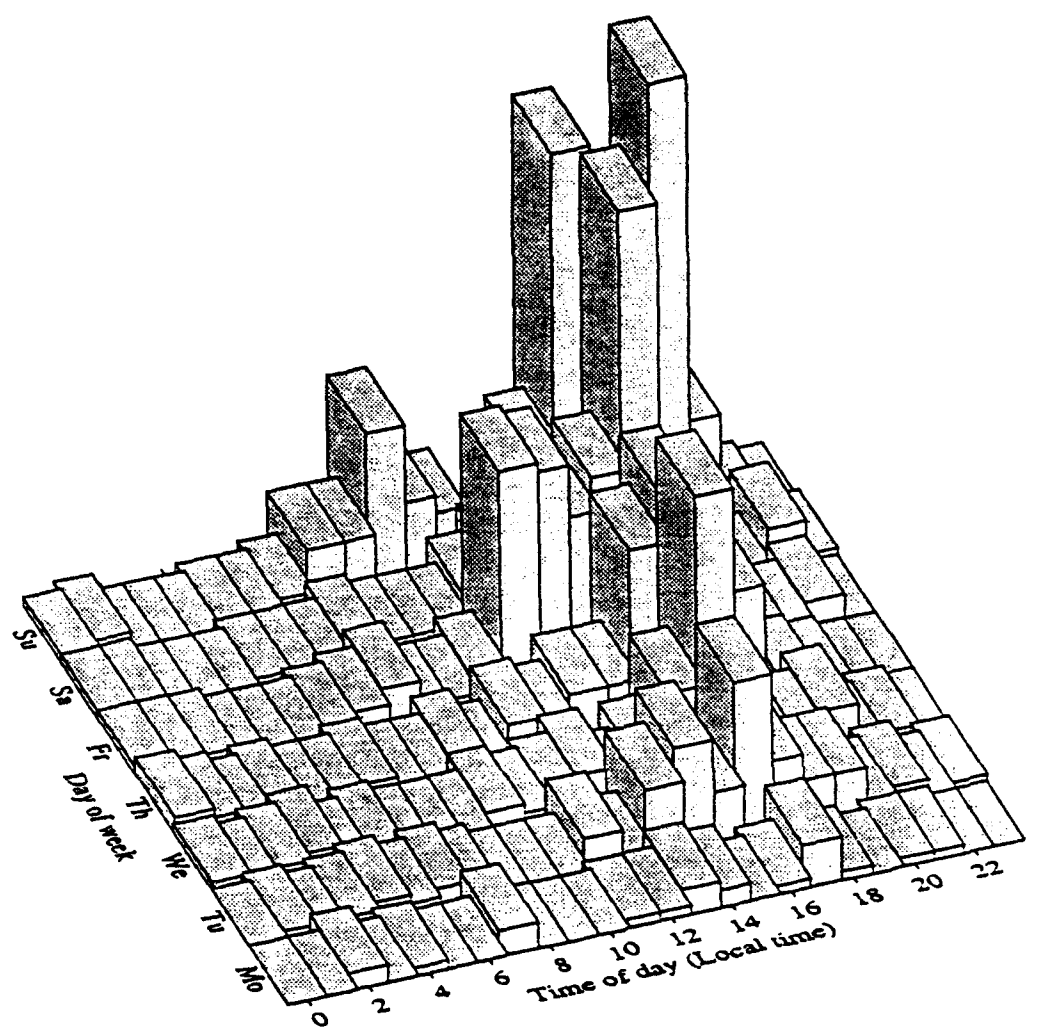


Fig. 12. Diurnal and weekly distribution of seismic events in Kola and adjacent areas for 1991. The majority of events occurred during working hours (afternoon) with strongly increased activity during weekends.

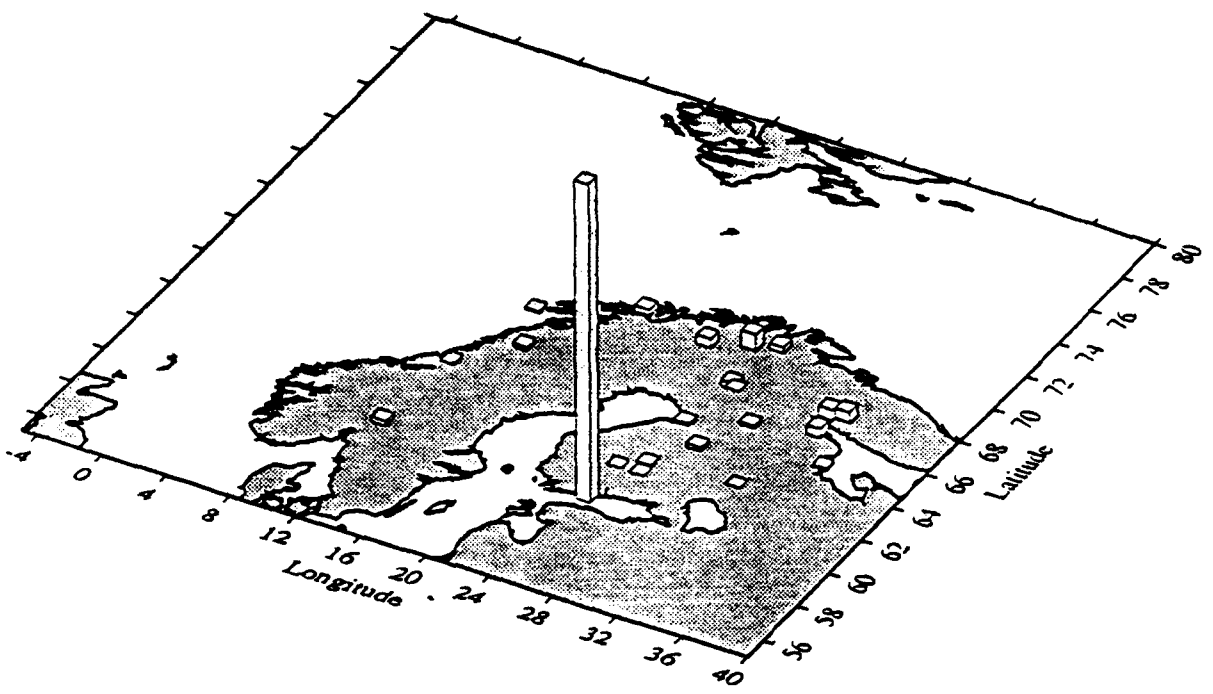
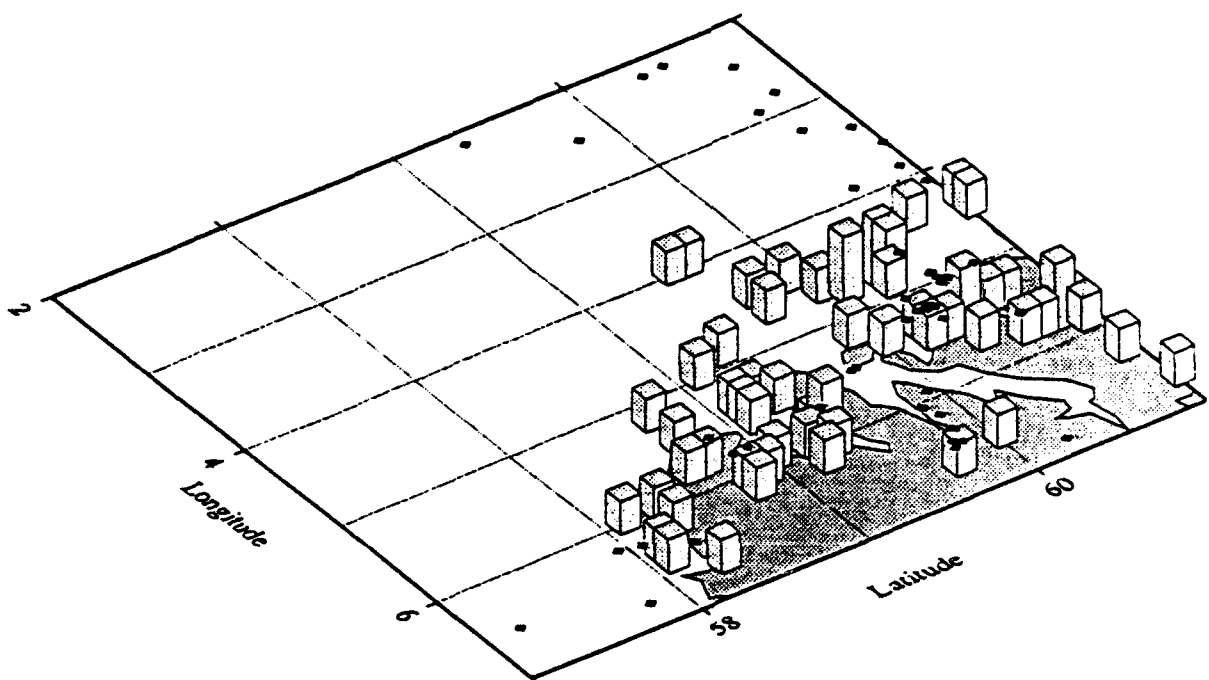


Fig. 13. Event reporting frequencies for agencies and stations of explosions on Kola Peninsula. The column height at Helsinki represents 470 events.



**Fig. 14.** Western Norway events in 1991, see Fig. 3 for symbols. The most active zone was around Bergen, (the highest column represents only 7 events). There different kinds of construction works took place. The area contributed 192 events in 1991, out of which 46 probably were listed as earthquakes.

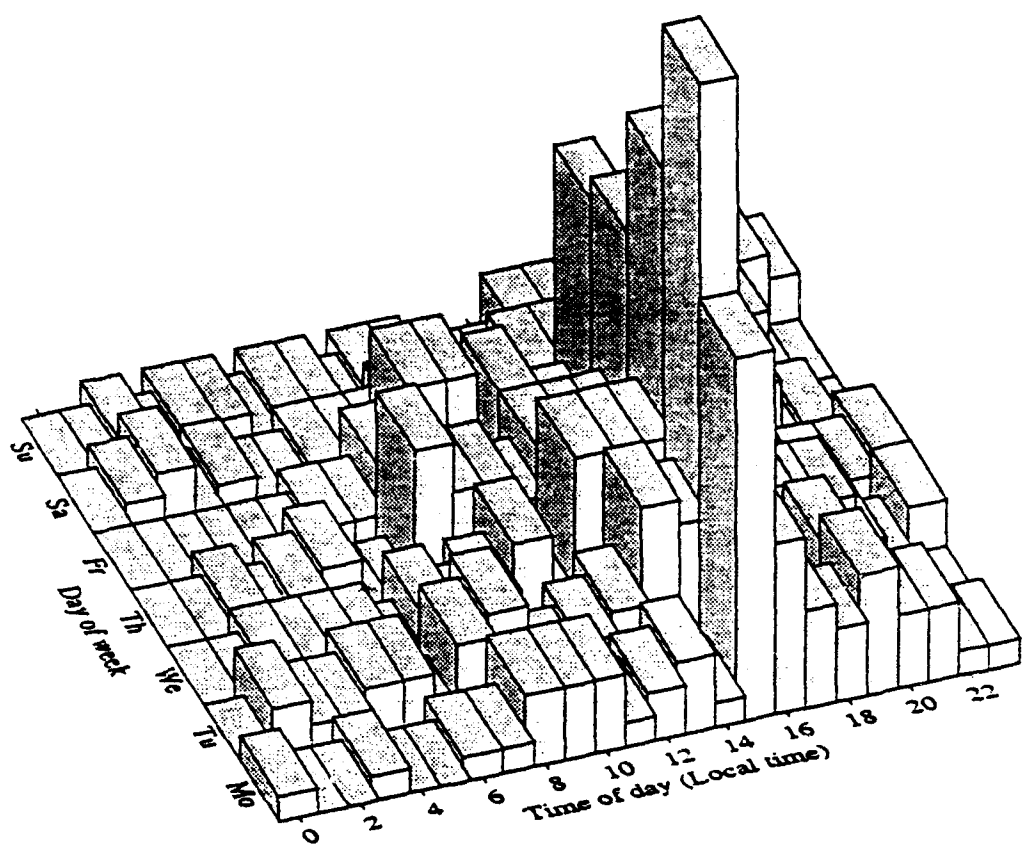


Fig. 15. Diurnal and weekly distribution of seismic events in western Norway. The highest activity is during working hours. Typically, there is less activity during weekends. The relatively large number of earthquakes (46 out of 191 events) explains the dispersion in the diurnal distribution.

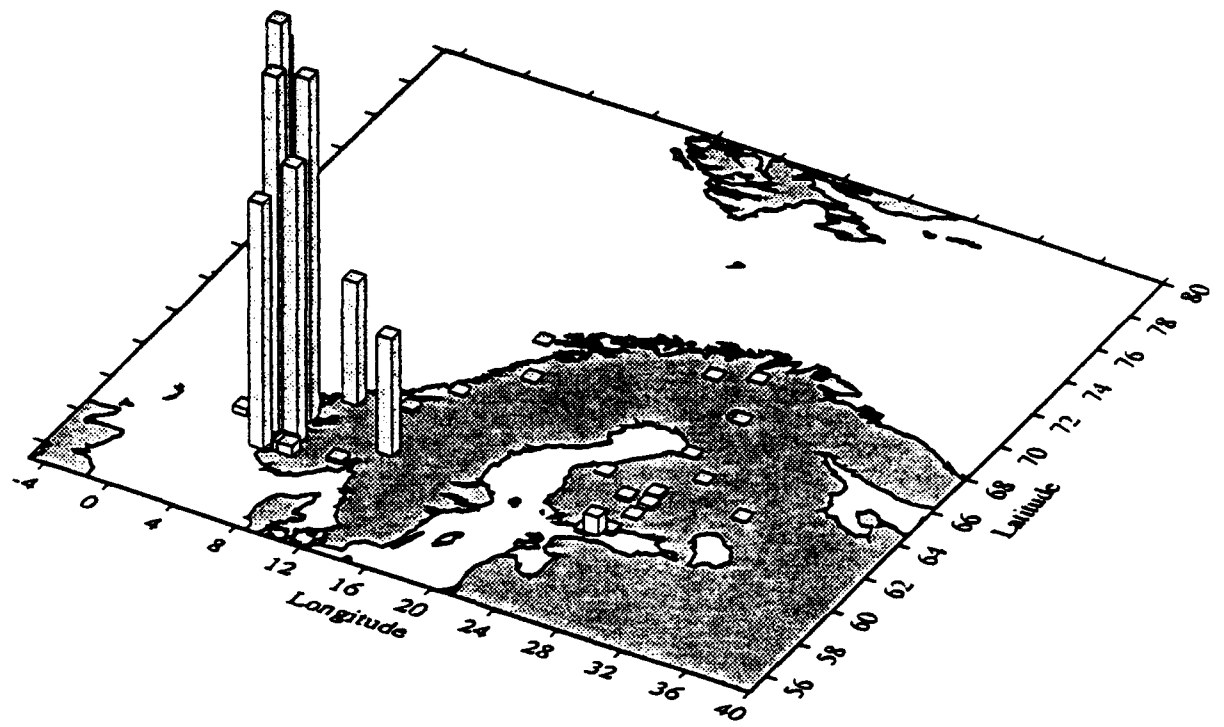


Fig. 16. Event reporting frequencies for agencies and stations of explosions and earthquakes in western Norway. The western Norwegian network reported mainly Norwegian coastal events, with the highest column for the station ASK accounting for 241 events. Some events, reported also in Finland and western Russia, were evidently earthquakes.

# 2D Finite Difference Elastic Wave Modeling including Surface Topography

Stig O. Hestholm\*, Bent O. Ruud#.

\**IBM Bergen Environmental Sciences and Solutions Centre,  
Thormøhlens gate 55, N-5008 Bergen, Norway.*

#*Institute of Solid Earth Physics, Bergen University,  
Allégaten 41, N-5007 Bergen, Norway.*

## Abstract

A 2D numerical finite difference algorithm accounting for surface topography is presented. Higher order, dispersion-bounded, cost-optimized finite difference operators are used in the interior of the numerical grid, while non-reflecting absorbing boundary conditions are used along the edges. A transfer from a curved to a rectangular grid achieves the modeling of the surface topography. Along the surface we use the free surface boundary conditions. To account for the surface topography is important for the complete modeling of the effects of wave propagation. Near-surface effects, such as scattering, are otherwise not modeled adequately. Even if other properties of the medium, for instance randomization, can improve numerical simulations, the inclusion of the surface topography make them more realistic.

## Introduction

Including topography at the free surface of an elastic medium leads to improved modeling of near-surface effects, especially those in the high frequency part of the wave field. Experimentation with other medium characteristics can partly

contribute to the same effects. Nevertheless, without including the topography in the medium model, the results of these experiments may be unreliable with regard to near-surface effects.

In recent years, finite difference methods have gained popularity among geophysicists as a flexible tool for modeling seismic wave propagation in various geological environments. Although most heterogeneous media can be effectively handled this way, the inclusion of topography at the surface of an elastic medium has proven to be a non-trivial problem in the synthetic calculations. Finite difference and finite element methods of lower order have often been used for the modeling of waves in the vicinity of surface topography. The difficulty with the finite difference modeling lies in adapting the grid required by the method on to the topography at the free surface. The finite element method is the more flexible in incorporating variable geometry, but it is more time consuming for the same order (Lysmer & Drake, 1972).

A cost-effective method well suited for handling different types of geometries, is the boundary element method e. g. see Mansur & Brebbia, 1981, 1982. This method applied in the elastic case can be found in Cruse & Rizzo (1968), Cruse (1968) and Hall & Robertson (1989) among others. For relatively simple structures in the interior of the medium (homogeneous or linearly varying), this method is advantageous in demanding less computer storage than other methods. The reason is that calculations are only kept track of along the boundaries. The boundaries can also have complex shapes, as long as they consist of closed curves. Nevertheless, full matrices have to be inverted.

A procedure for modeling free surface topography with lower order finite differences was given by Jih, McLaughlin & Der (1988). This work classified different types of slopes and abrupt changes of slopes, and prescribed a procedure for handling each of them by implementing the free surface conditions. To the contrary of Jih et. al. (1988), Tessmer, Kosloff & Behle (1992) assume a smooth surface,

i. e. the first derivative of the topography function exists. A stretched (or curved) coordinate system is initially applied, and its upper boundary coincides with the topography. A transformation onto a rectangular coordinate system is done in order to perform the computations, using the Chebyshev method and the Fourier method for spatial differentiation. The present work applies this transformation from a curved to a rectangular system, while using higher order, dispersion-bounded, cost-optimized finite difference operators (Sguazzer, Kindelan & Kamel, 1989) for discretizing the spatial derivatives. An additional coordinate transformation has to be done locally at each point on the surface, so that the vertical coordinate coincides with the normal vector before the implementation of the free surface boundary conditions. The discretization of these are done by lower order, central, staggered finite differences (Fornberg, 1988, a).

Although the method of Tessmer et. al. (1992) for incorporating topography at the free surface cannot be used directly in our context of finite difference methods, it proved instructive for our modification of the boundary conditions. The present work concentrates on the theory behind our procedure for modeling elastic waves. In forthcoming works results and analyses will be presented, as well as comparisons with a long range of real measurements.

The following sections present the basic equations together with their discretization onto a staggered grid (Sguazzer et. al., 1989, Levander, 1988). The equations for the curved system transferred onto the rectangular grid, where the computations are done, will be presented. Then the free boundary conditions resulting from the rotated coordinate systems at the surface are given. Next, we indicate how the numerical discretization is achieved. Finally, we present a few numerical examples with a random topography and realistic medium P-velocity models. These are illustrative of the importance of near-surface effects for the high-frequency part of the wave field.

## Elastic Wave Modeling Formulation

The basic equations governing wave propagation in a continuous elastic medium are the momentum conservation and the stress-strain relation. Using the velocity-stress formulation (Achenbach, 1975), these are given by

$$\rho \frac{\partial}{\partial t} v_j = f_j + \frac{\partial}{\partial x_l} \sigma_{jl}, \quad j, l = 1, \dots, J \quad (1)$$

$$\frac{\partial}{\partial t} \sigma_{jj} = \lambda \frac{\partial}{\partial x_l} v_l + 2\mu \frac{\partial}{\partial x_j} v_j, \quad j, l = 1, \dots, J \quad (2)$$

$$\frac{\partial}{\partial t} \sigma_{jl} = \mu \left( \frac{\partial}{\partial x_j} v_l + \frac{\partial}{\partial x_l} v_j \right), \quad j, l = 1, \dots, J, \quad j \neq l \quad (3)$$

where Einstein's summation convention is used.  $J$  is the dimension of the problem,  $\rho$  is density, and  $\lambda$  and  $\mu$  are Lamé's parameters.  $f_j$  are body forces and  $v_j$  and  $\sigma_{jl}$  are velocities and stresses respectively.

According to Tessmer et. al. (1992) and Fornberg (1988, b), a 2D transformation of a rectangular  $(\xi, \eta)$ -coordinate system into a curved  $(x, z)$ -coordinate system is a computational convenient way of introducing the surface topography. The rectangular  $(\xi, \eta)$ -system is limited by  $\xi = 0$ ,  $\xi = \xi_{max}$ ,  $\eta = 0$  and  $\eta = \eta_{max}$  (see Fig. 1). The  $(x, z)$ -system is curved or *stretched* in such a way that the  $x$ -axis coincides with the topography at the top of the system, where stretching is at its maximum. Below the surface the undulations of the  $x$ -axis decrease linearly with depth. At the bottom of the system, the  $x$ -axis is plane (see Fig. 2). When the positive direction along the vertical axis in both systems is upwards, the mapping from the  $(\xi, \eta)$ -system to the  $(x, z)$ -system can be given by

$$x(\xi, \eta) = \xi, \quad (4)$$

$$z(\xi, \eta) = \frac{\eta}{\eta_{max}} z_0(\xi), \quad (5)$$

where  $z_0(\xi)$  is the topography function. Applying (4) and (5), we have, for a differentiable function  $f(x, z)$

$$\frac{\partial f}{\partial x} = \frac{\partial f}{\partial \xi} + \frac{\partial f}{\partial \eta} \frac{\partial \eta}{\partial x}, \quad (6)$$

$$\frac{\partial f}{\partial z} = \frac{\partial f}{\partial \eta} \frac{\partial \eta}{\partial z}. \quad (7)$$

From expressions (4) and (5) we get (see Appendix 1)

$$\frac{\partial \xi}{\partial x} = 1, \quad \frac{\partial \xi}{\partial z} = 0, \quad (8)$$

$$A(\xi, \eta) = \frac{\partial \eta}{\partial x} = -\frac{\eta}{z_0(\xi)} \frac{\partial z_0(\xi)}{\partial \xi}, \quad (9)$$

$$B(\xi) = \frac{\partial \eta}{\partial z} = \frac{\eta_{max}}{z_0(\xi)}. \quad (10)$$

Expanding eqs. (1)–(3) by the chain rule and setting the dimension  $J = 2$  leads to the equations in the medium (see Appendix 2)

$$\rho \frac{\partial u}{\partial t} = \frac{\partial \sigma_{xx}}{\partial \xi} + A(\xi, \eta) \frac{\partial \sigma_{xz}}{\partial \eta} + B(\xi) \frac{\partial \sigma_{xz}}{\partial \eta} + f_x, \quad (11)$$

$$\rho \frac{\partial w}{\partial t} = \frac{\partial \sigma_{zz}}{\partial \xi} + A(\xi, \eta) \frac{\partial \sigma_{zz}}{\partial \eta} + B(\xi) \frac{\partial \sigma_{zz}}{\partial \eta} + f_z, \quad (12)$$

$$\frac{\partial \sigma_{xx}}{\partial t} = (\lambda + 2\mu) \left( \frac{\partial u}{\partial \xi} + A(\xi, \eta) \frac{\partial u}{\partial \eta} \right) + \lambda B(\xi) \frac{\partial w}{\partial \eta}, \quad (13)$$

$$\frac{\partial \sigma_{zz}}{\partial t} = \lambda \left( \frac{\partial w}{\partial \xi} + A(\xi, \eta) \frac{\partial w}{\partial \eta} \right) + (\lambda + 2\mu) B(\xi) \frac{\partial w}{\partial \eta}, \quad (14)$$

$$\frac{\partial \sigma_{xz}}{\partial t} = \mu \left( \frac{\partial w}{\partial \xi} + A(\xi, \eta) \frac{\partial w}{\partial \eta} + B(\xi) \frac{\partial u}{\partial \eta} \right), \quad (15)$$

where  $\rho$  is the density and  $\lambda$  and  $\mu$  are Lamé's parameters.  $f_x$  and  $f_z$  are the components of the body forces, and  $u$  and  $w$  are the two components of the particle velocity.  $\sigma_{xx}$ ,  $\sigma_{zz}$  and  $\sigma_{xz}$  are the stress components.

## Free Surface Boundary Conditions

The free boundary conditions on the velocities at a locally horizontal surface read

$$\frac{\partial u}{\partial z} = -\frac{\partial w}{\partial x}, \quad (16)$$

$$\frac{\partial w}{\partial z} = -\frac{\lambda}{\lambda + 2\mu} \left( \frac{\partial u}{\partial x} \right), \quad (17)$$

with  $x$  and  $z$  the horizontal and vertical coordinates respectively.

In order to apply these conditions at a topography surface, one has to enforce them at each point on the surface of a rotated, local coordinate system  $(x', z')$ . The orientation of the system  $(x', z')$  is such that the  $z'$ -axis is normal to the surface at each point. After having imposed the conditions (16) and (17) in the  $(x', z')$ -system, they have to be rotated back to the  $(\xi, \eta)$ -system by the transformation

$$\vec{v} = \mathbf{A} \vec{v}', \quad (18)$$

where  $\vec{v}$  and  $\vec{v}'$  are the particle velocity vectors in the  $(\xi, \eta)$ - and the  $(x', z')$ -systems respectively.  $\mathbf{A}$  is the rotation matrix, given by

$$\mathbf{A} = \begin{pmatrix} \cos \phi & \sin \phi \\ -\sin \phi & \cos \phi \end{pmatrix}. \quad (19)$$

$\phi$  is the angle of rotation between the actual  $(x', z')$ -system and the  $(\xi, \eta)$ -system. We also have the relation  $\tan \phi = \partial z_0(\xi) / \partial \xi$ . Details from the calculations of the rotation are given in Appendix 3.

We arrive at the conditions for the free surface topography given in the computational  $(\xi, \eta)$ -system by

$$\frac{\partial u}{\partial \eta} = -\frac{\partial w}{\partial \xi}, \quad (20)$$

$$\begin{aligned} \left( 1 - \frac{\lambda}{\lambda + 2\mu} \left[ \frac{\partial z_0(\xi)}{\partial \xi} \right]^2 \right) \frac{\partial w}{\partial \eta} = \\ \left( \left[ \frac{\partial z_0(\xi)}{\partial \xi} \right]^2 - \frac{\lambda}{\lambda + 2\mu} \right) \frac{\partial u}{\partial \xi} + 2 \frac{\partial z_0(\xi)}{\partial \xi} \left( 1 + \frac{\lambda}{\lambda + 2\mu} \right) \frac{\partial w}{\partial \xi}. \end{aligned} \quad (21)$$

Note that in the case of a plane surface, i. e.  $z_0(\xi) = \text{constant}$ , the eqs. (20) and (21) coincide with eqs. (16) and (17).

## Numerical Discretization

Spatial partial differentiation is achieved by cost-optimized, dispersion-bounded, high-order finite difference operators on a staggered grid. For time stepping a leap-frog technique is used. For details on the numerical discretization of the elastic equations, the reader is referred to Sguazzero et. al. (1989). To avoid artificial reflections from the computational boundaries, the multiplication of velocities and stresses by exponentially decreasing terms near the edges works satisfactorily. For the numerical dispersion relations, the stability limit and bandwidth introduced by the discretization, the reader is referred to Sguazzero et. al. (1989).

The main difference in the discretization of eqs. (20) and (21) compared to that of eqs. (16) and (17) is that we now stagger the vertical velocity component  $w$  one half grid length downwards instead of one half grid length upwards. Modifications according to this change have to be taken into account in discretizing the eqs. (11)–(15) inside the medium. By doing this, we still get explicit expressions for the variables  $u$ ,  $w$ ,  $\sigma_{xx}$ ,  $\sigma_{zz}$  and  $\sigma_{xz}$  at each time step of the integration. Second order, central, uniform, staggered finite difference operators (Fornberg, 1988, a) are retained for discretizing the free boundary conditions eqs. (20) and (21). Approaching the free boundary from below, we apply successively lower order in the central, staggered finite difference operators used for discretizing the spatial derivatives. Experiments were also done with 8th order, non-centred finite difference operators according to Fornberg (1988, a) for discretization near the free surface, without getting stable results in time. A pictorial view of the definition of the particle velocities on the numerical grid is shown in Fig. 3. The staggered

definition of  $u$  and  $w$ , the horizontal and vertical velocity components respectively, is shown here.

Automatization of our procedure follows from the fact that the rotation of each local coordinate system is given in terms of derivatives. Our way of treating surface topography therefore becomes global. One does not need to consider each specific surface point in the procedure. As also the medium equations are solved numerically by the same procedure for the whole grid, our program is global with regard to the points of the elastic medium. The only distinction is made between the surface points and the points inside the medium.

Another superior property in our procedure is the application of the optimized finite difference operators due to Sguazzero et. al. (1989). One can choose a certain maximum error in the numerical group velocity inside the medium, where the operators are applied. In our runs, this maximum error is chosen to be 1.5 %. Given a chosen error for the numerical group velocity, together with a certain chosen order of the finite difference operator, one is also ensured that the computational cost of the resulting operator has been minimized.

## Numerical Examples

Results of numerical examples are shown in Figs. 4-14. The two particle velocity components, the divergence and curl are displayed in snapshots 10 seconds after a pressure wave has been initiated from a Gaussian point source with a central frequency of 2.5 Hz. The source is placed 75 km from the left edge of the grid and 2 km below the surface. The total size of the computational  $(\xi, \eta)$ -grid is 150 km times 400 km, with 751 grid points vertically and 2001 points horizontally. The grid length in each direction is 200 m. Distances of the snapshots are given in kilometers. In each snapshot, only the upper 40 km of a 100 km horizontal subsection is shown displaying the current wave front. A grey tone scale is given

for each variable. Here, divergences and curls are scaled up by a factor of  $10^3$  compared to the particle velocities.

The surface topography used in our runs (Fig. 4) is generated by a 1D realization of a von Kármán random medium (Charrette, 1991). The parameters are *order* = 1.0, *correlation distance* = 10 km and *standard deviation* (RMS) = 200 m. Distances in Fig. 4 are given in kilometers.

The parameters of a von Kármán random medium can be understood in the following way. The smoothest version of the medium is attained for *order* = 1.0, while the strongest variations (self-similarity) is attained for *order* = 0.0. The *correlation distance* is the longest distance for which two points of the function in question are highly correlated. Points separated by more than the correlation distance are close to uncorrelated. The *standard deviation* is the root mean square (RMS) of the maximum permitted variation from the average. Also, see Frankel & Clayton (1986).

Too abrupt changes in the topography over short distances leads to instability of our procedure. Computing the derivatives by higher order operators will then lead to difficulties, resulting in unwanted oscillations in the computations. An experimental measure for the stability limit of our procedure can be obtained for each type of topography by varying parameters characterizing its surface. For our von Kármán curve, experiments were done by varying the RMS, while keeping *order* = 1.0 and *correlation distance* = 10 km. The results lead to an approximate stability limit of 220 m as the upper bound for the RMS. As mentioned above, a value near this one (200 m) was chosen for our synthetics, in order to retain maximum variations in the topography.

For each of the two initial runs, a different type of medium model has been applied. Fig. 9 shows the first model, where the medium P-velocities are defined by different linear functions vertically. There is a constant low velocity layer at the upper 800 m, where the P-velocity is 4850 m/s. In the next 800 m below this,

the P-velocity increases linearly from 4850 m/s to 6150 m/s. Then, from depth 1.6 km to depth 35 km, there is a linear increase in the P-velocity from 6150 m/s to 7000 m/s. At depth 35 km, which signifies the Moho, we have a discontinuity in the medium P-velocity. From here it increases linearly from 8000 m/s to 8500 m/s, which is the P-velocity at the bottom of the grid, 150 km below the top. The snapshots in Figs. 5-8 have been generated using this model.

The medium model applied in the second run is displayed in Fig. 14. The same linear variations in the medium P-velocity as in Fig. 9 are applied, but additionally the value at each point has been randomized by a 2D von Kármán realization (Charrette, 1991). The parameters used for this randomization were *order* = 0.3, *horizontal correlation distance* = 10 km, *vertical correlation distance* = 2.5 km and RMS = 3 %. Thus, an apparent anisotropy has been included in the medium by letting the horizontal correlation distance be 4 times larger than the vertical one. The snapshots in Figs. 10-13 have been generated using this model. Here the waves have more irregular shapes. In each of the runs the medium shear velocity is defined by the P-velocity divided by  $\sqrt{3}$ , and the density is given as a linear function of the P-velocity.

In the runs of this paper no random velocity variations were applied in the upper 1600 m of the medium. Test runs with random velocity variations all the way up to the free surface were performed. These showed scattered surface waves of unrealistically strong amplitudes. The reason for this may partly be that no intrinsic attenuation is included in the modeling. Under real conditions attenuation is usually quite strong near the surface due to the presence of a weathering layer.

Snapshots from both runs reveal mode conversions, back-scattering and asymmetric P-to-P and P-to-S reflections. From this we deduce that free surface topography can cause these effects. Most often such effects are discussed only in terms of inter-crust heterogeneities. Likewise, the fundamental mode Rayleigh (Rg) wave propagation in the uppermost part of the crust is very sensitive to the

roughness of the local topography, as synthesized and discussed in Ruud, Husebye and Hestholm (1993).

In order to visualize effects of including surface topography, we present snapshots of the vertical velocity component for plane surfaces in Figs. 15 and 16. Fig. 15 shows this with the medium model of Fig. 9 applied, and Fig. 16 shows it with the medium model of Fig. 14 applied. It is interesting to note the differences from the corresponding snapshots of the vertical velocity component with added topography (Figs. 6 and 11). In Figs. 15 and 16 we note that the scattered surface waves, seen as a black/white banding near the surface in Figs. 6 and 11, are almost absent, particularly in the horizontal range from 50 to 90 km.

Fig. 17 display seismograms for all four runs. 40 seconds simulation time is used to include all significant wavelets emanating from a source with central frequency of 2.5 Hz at depth 2 km. In each case 6 receivers are located at the surface starting at 90 km to the right of the horizontal position of the source, with a spacing of 800 m between them. In section a) of Fig. 17 seismograms for a plane surface with the velocity model of Fig. 9 are shown (no topography or medium randomization). Here scattered waves are absent, and the following phases are clearly seen: Direct P-wave at about 14 seconds, P-wave reflection from the Moho at 17 seconds, a converted P-to-S reflection from the Moho at 23 seconds as well as surface waves in the interval 26 to 37 seconds. Here the wave with highest amplitude and lowest frequency is the fundamental mode Rg wave, while the surface waves with weaker amplitudes and higher frequencies represent higher order modes (Ruud et. al., 1993).

In the next sections of Fig. 17 we see how the recordings increasingly get disturbed by scattered waves. b) shows corresponding seismograms for a plane surface with the velocity model of Fig. 14 (no topography with medium randomization). Here the reflected P-wave from the Moho has an abnormally high amplitude on some sensors. This is probably due to an accidental focussing effect of the velocity

randomization. The two last sections of Fig. 17 (c) and d)) contain seismograms with the topography of Fig. 4 included. c) is for the velocity model of Fig. 9 (topography without medium randomization), and d) is for the velocity model of Fig. 14 (topography and medium randomization). In both cases the fundamental mode Rg wave is strongly disturbed, only the lowest frequency part can be recognized. Towards the end of the two sections (35 to 40 seconds) some strong coda waves can be observed. These are backscattered surface waves moving from right to left in the model. They are created by scattering of other waves at the free surface topography. In d) we do not see the same pattern as in b) from the accidental focussing effects due to velocity randomization. This is because the random models are two different realizations using the same statistical parameters.

The snapshots shown in Figs. 5-8, 10-13, 15 and 16 were arrived at after 4 hours and 20 minutes on the IBM 3090 / 600 S VF computer\* located at IBM Bergen Environmental Sciences and Solutions Centre, Bergen, Norway. This is the location for all numerical experiments performed for this work.

## Conclusions

The basic assumption of the calculations is that the topography function must be smooth, i. e. the first derivative of  $z_0(\xi)$  must exist. If the function varies too much over a certain region, Gibb's phenomenon will arise, and the resulting oscillations will destroy the simulation. The limit for this to occur is a matter of experimentation. Given that this stability condition is fulfilled, the above procedure is a powerful tool for the finite difference modeling of an elastic medium including free surface topography.

---

\* IBM 3090 is a trademark of International Business Machines Corporation.

## **Acknowledgements**

IBM Bergen Environmental Sciences & Solutions Centre is acknowledged for generous use of its IBM 3090/600S VF mainframe computer. B.O.R. acknowledges his support from the Air Force Office of Scientific Research, USAF, under Grant F49620-92-J-0510 and his research fellowship from the Royal Norwegian Council for Sciences and Humanities Research.

## References

- ACHENBACH, J. D. 1975. *Wave Propagation in Elastic Solids*, North Holland Publishing Company, The Netherlands.
- CHARRETTE III, E. E. 1991. *Elastic Wave Scattering in Laterally Inhomogeneous Media*, Thesis for the Degree of Doctor of Philosophy, Massachusetts Institute of Technology, January, 1991.
- CRUSE, T. A., and RIZZO, F. J. 1968. *A Direct Formulation and Numerical Solution of the General Transient Elastodynamic Problem. I*, Journal of Mathematical Analysis and Applications, 22, pp. 244-259.
- CRUSE, T. A. 1968. *A Direct Formulation and Numerical Solution of the General Transient Elastodynamic Problem. II*, Journal of Mathematical Analysis and Applications, 22, pp. 341-355.
- FORNBERG, B. 1988 a. *Generation of Finite Difference Formulas on Arbitrary Spaced Grids*, Mathematics of Computation, 51, pp. 699-706.
- FORNBERG, B. 1988 b. *The Pseudospectral Method: Accurate Representation of Interfaces in Elastic Wave Calculations*, Geophysics, 53, pp. 625-637.
- FRANKEL, A., and CLAYTON, R. 1986. *Finite Difference Simulations of Seismic Scattering: Implications for the Propagation of Short-Period Seismic Waves in the Crust and Models of Crustal Heterogeneity*, J. Geophys. Res., 91, pp. 6464-6489.
- HALL, W. S., and ROBERTSON, W. H. 1989. *Advanced Boundary Element Calculations for Elastic Wave Scattering*, Elastic Wave Propagation, pp. 459-464, Elsevier Science Publishers B. V. (North-Holland).
- JIH, R.-S., MCLAUGHLIN, K. L., DER, Z. A. 1988. *Free-Boundary Conditions of Arbitrary Polygonal Topography in a Two-Dimensional Explicit Elastic Finite-Difference Scheme*, Geophysics, 53, pp. 1045-1055.

- LEVANDER, A. R. 1988. *Fourth-Order Finite-Difference P-SV Seismograms*, Geophysics, 53, pp. 1425-1436.
- LYSMER, J., and DRAKE, L. A. 1972. *A Finite Element Method for Seismology*, Methods in Computational Physics, 11, pp. 181-216, ed. B. A. Bolt, Academic Press, New York.
- MANSUR, W. J., and BREBBIA, C. A. 1982. *Formulation of the Boundary Element Method for Transient Problems governed by the Scalar Wave Equation*, Appl. Math. Modelling, 6, pp. 307-311.
- MANSUR, W. J., and BREBBIA, C. A. 1982. *Numerical Implementation of the Boundary Element Method for Two Dimensional Transient Scalar Wave Propagation Problems*, Appl. Math. Modelling, 6, pp. 299-306.
- RUUD, B. O., HUSEBYE, E., and HESTHOLM, S. O. 1993. *Rg Observations from Four Continents: Inverse- and Forward-Modelling Experiments*, Geophys. J. Int., 114, pp. 465-472.
- SGUAZZERO, P., KINDELAN, M., and KAMEL, A. 1989. *Dispersion-Bounded Numerical Integration of the Elastodynamic Equations*, Proceedings of the ICOSAHOM Conference, Como, Italy, June, 1989, pp. 165-172. North Holland Publishing Company, The Netherlands.
- TESSMER, E., KOSLOFF, D., and BEHLE, A. 1992. *Elastic Wave Propagation Simulation in the Presence of Surface Topography*, Geophys. J. Int., 108, pp. 621-632.

## Appendix 1

For the equations in the medium we need  $\frac{\partial \xi}{\partial x}$ ,  $\frac{\partial \xi}{\partial z}$ ,  $\frac{\partial \eta}{\partial x}$  and  $\frac{\partial \eta}{\partial z}$ . They are found from

$$\begin{aligned} \frac{\partial x}{\partial \xi} \frac{\partial \xi}{\partial x} + \frac{\partial x}{\partial \eta} \frac{\partial \eta}{\partial x} &= 1, & \frac{\partial x}{\partial \xi} \frac{\partial \xi}{\partial z} + \frac{\partial x}{\partial \eta} \frac{\partial \eta}{\partial z} &= 0, \\ \frac{\partial z}{\partial \xi} \frac{\partial \xi}{\partial x} + \frac{\partial z}{\partial \eta} \frac{\partial \eta}{\partial x} &= 0, & \frac{\partial z}{\partial \xi} \frac{\partial \xi}{\partial z} + \frac{\partial z}{\partial \eta} \frac{\partial \eta}{\partial z} &= 1. \end{aligned}$$

This leads to

$$\begin{aligned} \frac{\partial \xi}{\partial x} &= \frac{\partial z}{\partial \eta}/J, & \frac{\partial \xi}{\partial z} &= -\frac{\partial x}{\partial \eta}/J, \\ \frac{\partial \eta}{\partial x} &= -\frac{\partial z}{\partial \xi}/J, & \frac{\partial \eta}{\partial z} &= \frac{\partial x}{\partial \xi}/J, \end{aligned}$$

with

$$J = \frac{\partial x}{\partial \xi} \frac{\partial z}{\partial \eta} - \frac{\partial x}{\partial \eta} \frac{\partial z}{\partial \xi}.$$

With our choice of mapping functions, eqs. (4) and (5), we get

$$\begin{aligned} \frac{\partial x}{\partial \xi} &= 1, & \frac{\partial x}{\partial \eta} &= 0, \\ \frac{\partial z}{\partial \xi} &= \frac{\eta}{\eta_{max}} \frac{\partial z_0(\xi)}{\partial \xi}, & \frac{\partial z}{\partial \eta} &= \frac{z_0(\xi)}{\eta_{max}} \end{aligned}$$

and

$$J = \frac{\partial z}{\partial \eta} = \frac{z_0(\xi)}{\eta_{max}}.$$

From this we get the expressions eqs. (8)–(10).

## Appendix 2

Applying the chain rule on eqs. (1)–(3) with the dimension  $J = 2$  leads to

$$\rho \frac{\partial u}{\partial t} = \frac{\partial \sigma_{xx}}{\partial \xi} \frac{\partial \xi}{\partial x} + \frac{\partial \sigma_{xz}}{\partial \eta} \frac{\partial \eta}{\partial x} + \frac{\partial \sigma_{zz}}{\partial \xi} \frac{\partial \xi}{\partial z} + \frac{\partial \sigma_{xz}}{\partial \eta} \frac{\partial \eta}{\partial z} + f_x,$$

$$\rho \frac{\partial w}{\partial t} = \frac{\partial \sigma_{xz}}{\partial \xi} \frac{\partial \xi}{\partial x} + \frac{\partial \sigma_{zz}}{\partial \eta} \frac{\partial \eta}{\partial x} + \frac{\partial \sigma_{zz}}{\partial \xi} \frac{\partial \xi}{\partial z} + \frac{\partial \sigma_{xz}}{\partial \eta} \frac{\partial \eta}{\partial z} + f_z,$$

$$\frac{\partial \sigma_{xx}}{\partial t} = (\lambda + 2\mu) \left( \frac{\partial u}{\partial \xi} \frac{\partial \xi}{\partial x} + \frac{\partial u}{\partial \eta} \frac{\partial \eta}{\partial x} \right) + \lambda \left( \frac{\partial w}{\partial \xi} \frac{\partial \xi}{\partial z} + \frac{\partial w}{\partial \eta} \frac{\partial \eta}{\partial z} \right),$$

$$\frac{\partial \sigma_{zz}}{\partial t} = \lambda \left( \frac{\partial u}{\partial \xi} \frac{\partial \xi}{\partial x} + \frac{\partial u}{\partial \eta} \frac{\partial \eta}{\partial x} \right) + (\lambda + 2\mu) \left( \frac{\partial w}{\partial \xi} \frac{\partial \xi}{\partial z} + \frac{\partial w}{\partial \eta} \frac{\partial \eta}{\partial z} \right),$$

$$\frac{\partial \sigma_{xz}}{\partial t} = \mu \left( \frac{\partial w}{\partial \xi} \frac{\partial \xi}{\partial x} + \frac{\partial w}{\partial \eta} \frac{\partial \eta}{\partial x} + \frac{\partial u}{\partial \xi} \frac{\partial \xi}{\partial z} + \frac{\partial u}{\partial \eta} \frac{\partial \eta}{\partial z} \right).$$

Substituting for  $\partial \xi / \partial x$ ,  $\partial \xi / \partial z$ ,  $\partial \eta / \partial x$  and  $\partial \eta / \partial z$  from eqs. (8)–(10), we get the medium equations eqs. (11)–(15).

## Appendix 3

Suppose a vector  $\vec{v}$  is given in a coordinate system with basis vectors  $\vec{i}$  and  $\vec{j}$ . This system is then rotated an angle  $\phi$  into a new coordinate system, with basis vectors  $\vec{i}'$  and  $\vec{j}'$ . In this new system the vector  $\vec{v}$  is denoted by  $\vec{v}'$ . We then have the connections

$$\begin{aligned} \vec{i}' &= \cos \phi \cdot \vec{i} + \sin \phi \cdot \vec{j} \\ \vec{j}' &= -\sin \phi \cdot \vec{i} + \cos \phi \cdot \vec{j} \end{aligned} \Big\} = \mathbf{A} \cdot \vec{I},$$

with  $\vec{I}$  being the vector  $(\vec{i}, \vec{j})$ . Correspondingly, we have

$$\begin{aligned} \vec{i} &= \cos \phi \cdot \vec{i}' - \sin \phi \cdot \vec{j}' \\ \vec{j} &= \sin \phi \cdot \vec{i}' + \cos \phi \cdot \vec{j}' \end{aligned} \Big\} = \mathbf{A}^{-1} \cdot \vec{I}',$$

with  $\vec{I}'$  being the vector  $(\vec{i}', \vec{j}')$  and  $\mathbf{A}^{-1}$  being the inverse of the rotation matrix.

The coordinate transformation for  $\vec{v}$  is described by  $\vec{v} = \mathbf{A}\vec{v}'$ . Hence,  $\vec{v}' = \mathbf{A}^{-1}\vec{v}$  or, with  $u'$  and  $w'$  the components of  $\vec{v}'$ , and  $u$  and  $w$  the components of  $\vec{v}$ ,

$$u' = \cos \phi \cdot u - \sin \phi \cdot w,$$

$$w' = \sin \phi \cdot u + \cos \phi \cdot w.$$

Applying the chain rule on a differentiable function  $f$ , we have

$$\begin{aligned}\frac{\partial f}{\partial x'} &= \frac{\partial f}{\partial \xi} \frac{\partial \xi}{\partial x'} + \frac{\partial f}{\partial \eta} \frac{\partial \eta}{\partial x'} \\ &= \frac{\partial f}{\partial \xi} \cos \phi + \frac{\partial f}{\partial \eta} \sin \phi, \\ \frac{\partial f}{\partial z'} &= \frac{\partial f}{\partial \xi} \frac{\partial \xi}{\partial z'} + \frac{\partial f}{\partial \eta} \frac{\partial \eta}{\partial z'} \\ &= \frac{\partial f}{\partial \xi} (-\sin \phi) + \frac{\partial f}{\partial \eta} \cos \phi.\end{aligned}$$

We have to enforce the free boundary conditions on the velocities into the  $(x', z')$ -system, where the  $z'$ -axis is normal to the surface at the local point, i. e.

$$\begin{aligned}\frac{\partial u'}{\partial z'} &= -\frac{\partial w'}{\partial x'}, \\ \frac{\partial w'}{\partial z'} &= -\frac{\lambda}{\lambda + 2\mu} \frac{\partial u'}{\partial x'}.\end{aligned}$$

If the chain rule is applied as above, we get

$$\begin{aligned}\frac{\partial u'}{\partial \xi} (-\sin \phi) + \frac{\partial u'}{\partial \eta} \cos \phi &= -\frac{\partial w'}{\partial \xi} \cos \phi - \frac{\partial w'}{\partial \eta} \sin \phi, \\ \frac{\partial w'}{\partial \xi} (-\sin \phi) + \frac{\partial w'}{\partial \eta} \cos \phi &= -\frac{\lambda}{\lambda + 2\mu} \left( \frac{\partial u'}{\partial \xi} \cos \phi + \frac{\partial u'}{\partial \eta} \sin \phi \right).\end{aligned}$$

Now we use the expressions given above for  $u'$  and  $w'$  which we got from the rotation. Then we obtain

$$\begin{aligned} & -\sin \phi \cos \phi \frac{\partial u}{\partial \xi} + \sin^2 \phi \frac{\partial w}{\partial \xi} + \cos^2 \phi \frac{\partial u}{\partial \eta} - \sin \phi \cos \phi \frac{\partial w}{\partial \eta} \\ &= -\sin \phi \cos \phi \frac{\partial u}{\partial \xi} - \cos^2 \phi \frac{\partial w}{\partial \xi} - \sin^2 \phi \frac{\partial u}{\partial \eta} - \sin \phi \cos \phi \frac{\partial w}{\partial \eta}, \\ & -\sin^2 \phi \frac{\partial u}{\partial \xi} - \sin \phi \cos \phi \frac{\partial w}{\partial \xi} + \sin \phi \cos \phi \frac{\partial u}{\partial \eta} + \cos^2 \phi \frac{\partial w}{\partial \eta} \\ &= -\frac{\lambda}{\lambda + 2\mu} \left\{ \cos^2 \phi \frac{\partial u}{\partial \xi} - \sin \phi \cos \phi \frac{\partial w}{\partial \xi} + \sin \phi \cos \phi \frac{\partial u}{\partial \eta} - \sin^2 \phi \frac{\partial w}{\partial \eta} \right\}. \end{aligned}$$

The first of these equations immediately leads to

$$\frac{\partial u}{\partial \eta} = -\frac{\partial w}{\partial \xi}.$$

The second equation leads to

$$\begin{aligned} & \left( \frac{\lambda}{\lambda + 2\mu} - \tan^2 \phi \right) \frac{\partial u}{\partial \xi} + \left( 1 - \frac{\lambda}{\lambda + 2\mu} \tan^2 \phi \right) \frac{\partial w}{\partial \eta} \\ &= \tan \phi \left( 1 + \frac{\lambda}{\lambda + 2\mu} \right) \frac{\partial w}{\partial \xi} - \tan \phi \left( 1 + \frac{\lambda}{\lambda + 2\mu} \right) \frac{\partial u}{\partial \eta}, \end{aligned}$$

after dividing by  $\cos^2 \phi$  and restructuring. This division requires the assumption  $\phi \neq \pm \pi/2$ , which means that the topography cannot have vertical subsections, i. e. the topography function must be single-valued. Given the condition of smoothness for  $z_0(\xi)$ , this is a reasonable assumption. Now we apply the first of these equations into the second one and use the equality  $\tan \phi = \partial z_0(\xi)/\partial \xi$ . Then we arrive at eqs. (20) and (21) as a possible set of free boundary conditions at a topography surface.

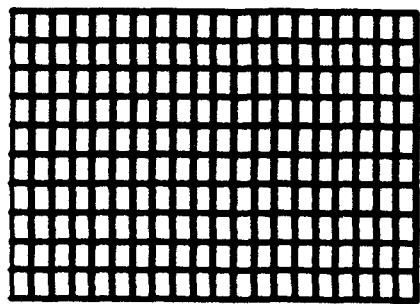


Figure 1: Rectangular grid.

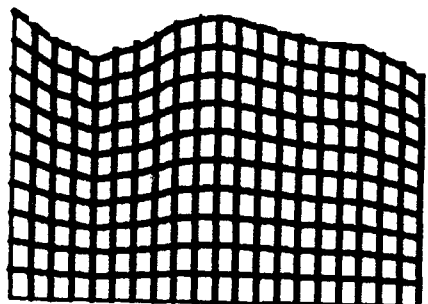
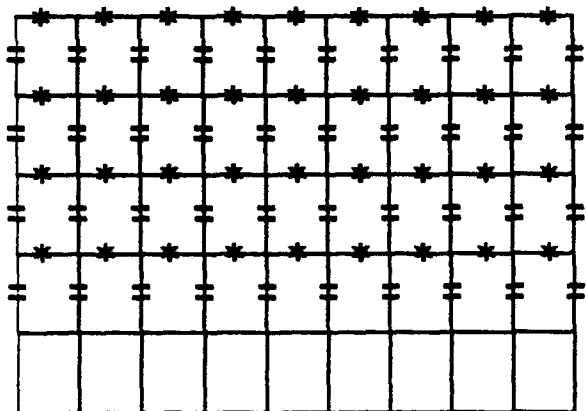


Figure 2: Curved grid.



1th velocity component u defined as \*.  
 2nd velocity component w defined as =.

Figure 3: Particle velocity definition on the numerical grid.

### Topography

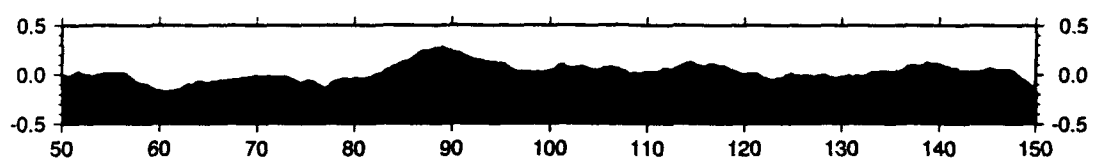


Figure 4: Surface topography used in the simulations.

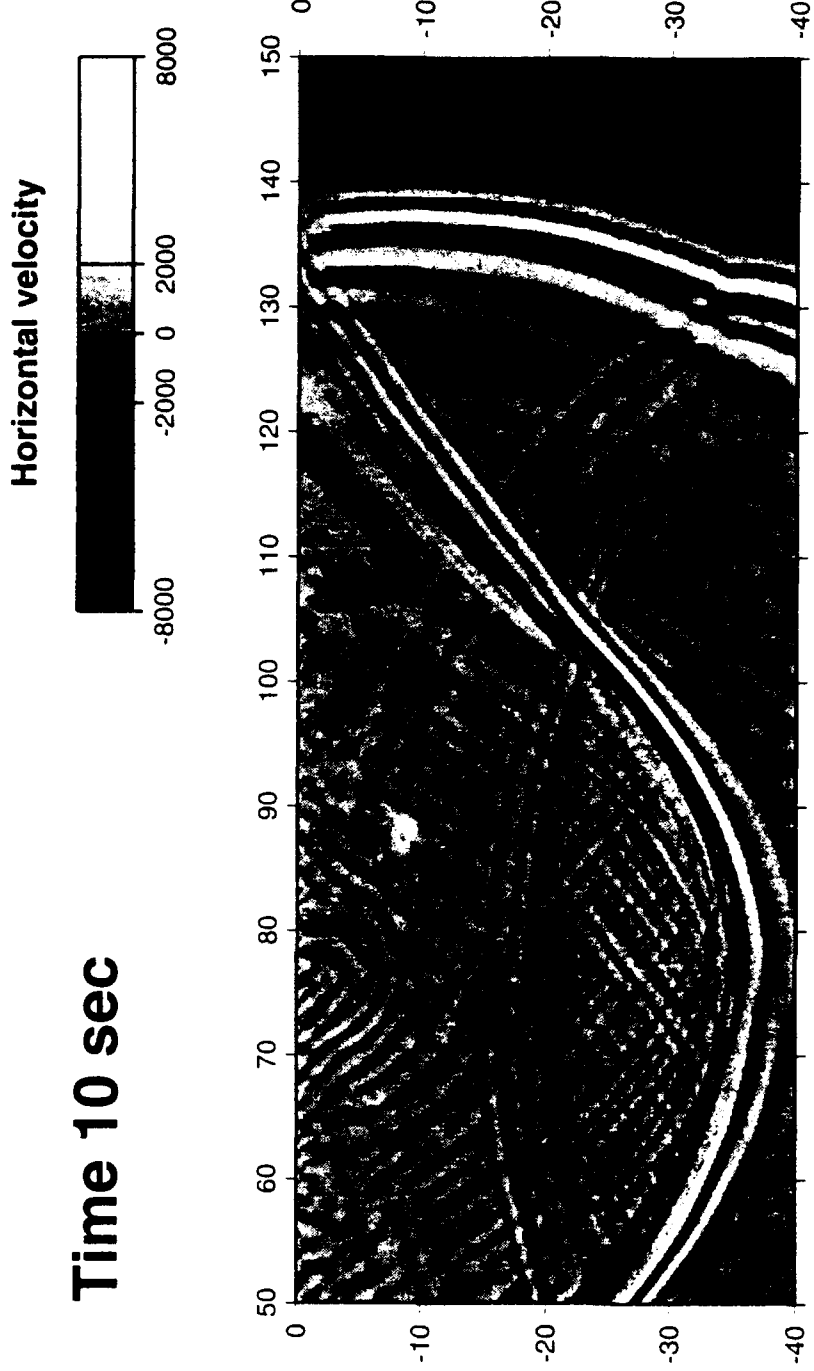


Figure 5: Snapshot of horizontal particle velocity 10 seconds after a pressure wave is initiated from a Gaussian point source with depth 2 km below the surface topography. The medium model is displayed in Fig. 9.

Vertical velocity

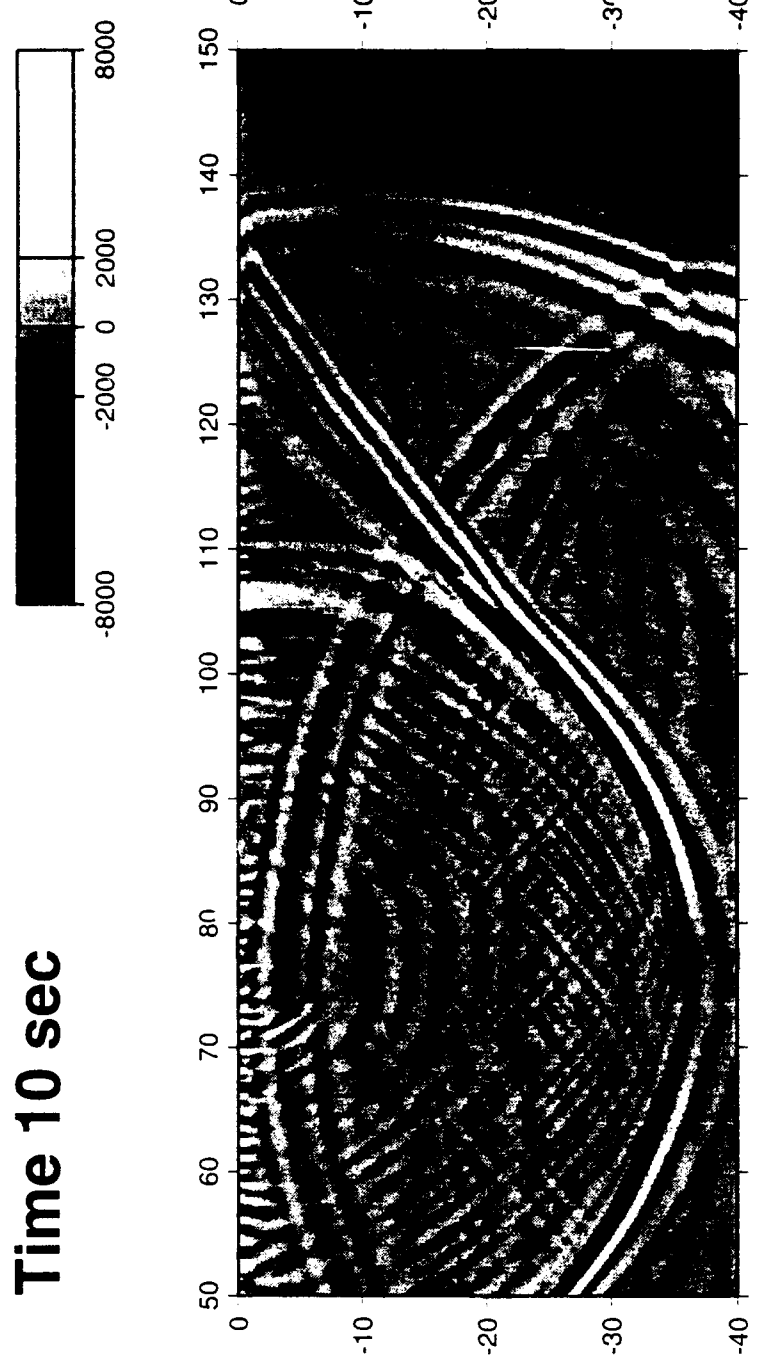


Figure 6. Snapshot of vertical particle velocity for the same situation as in Fig. 5.

$B = 23$

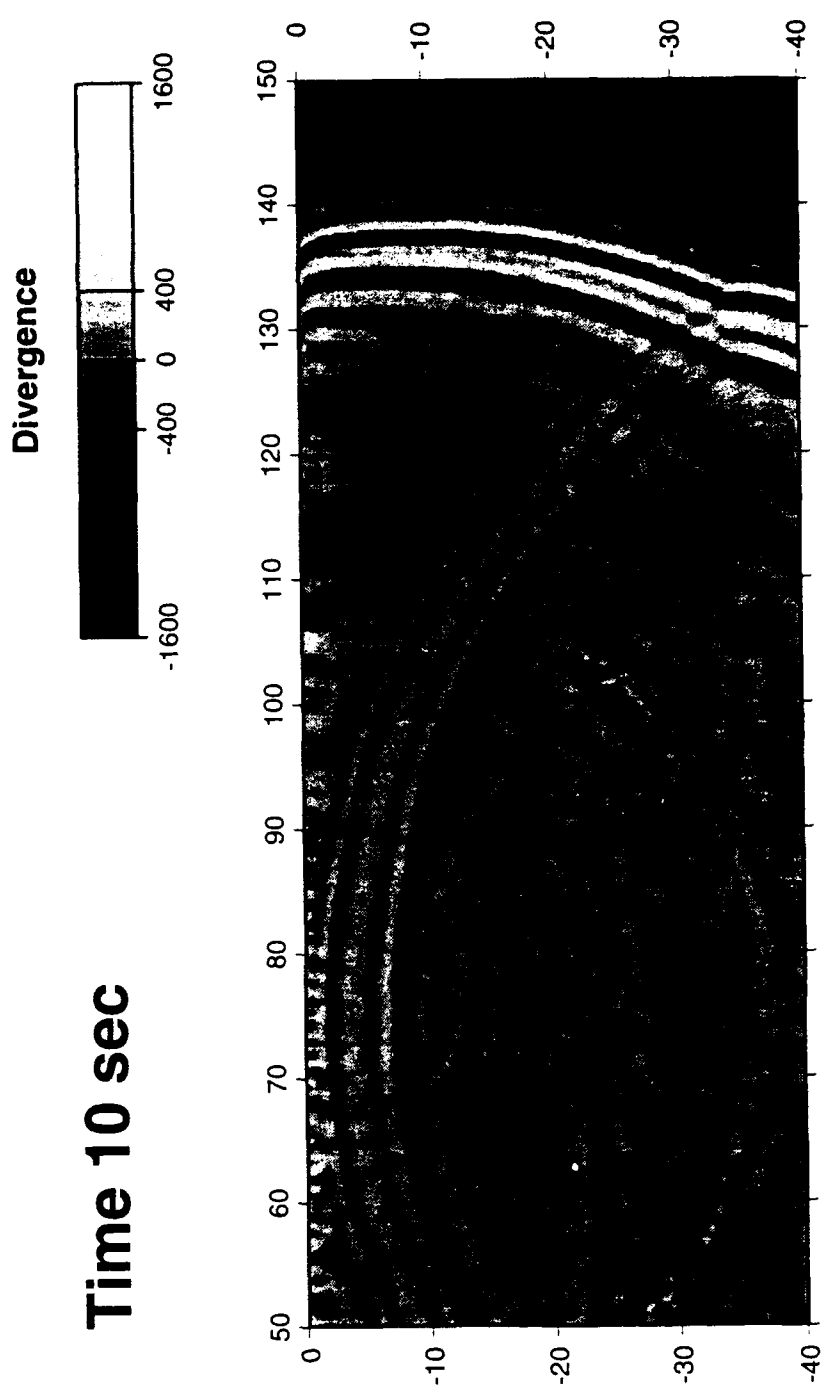


Figure 7: Snapshot of divergence for the same situation as in Fig. 5.

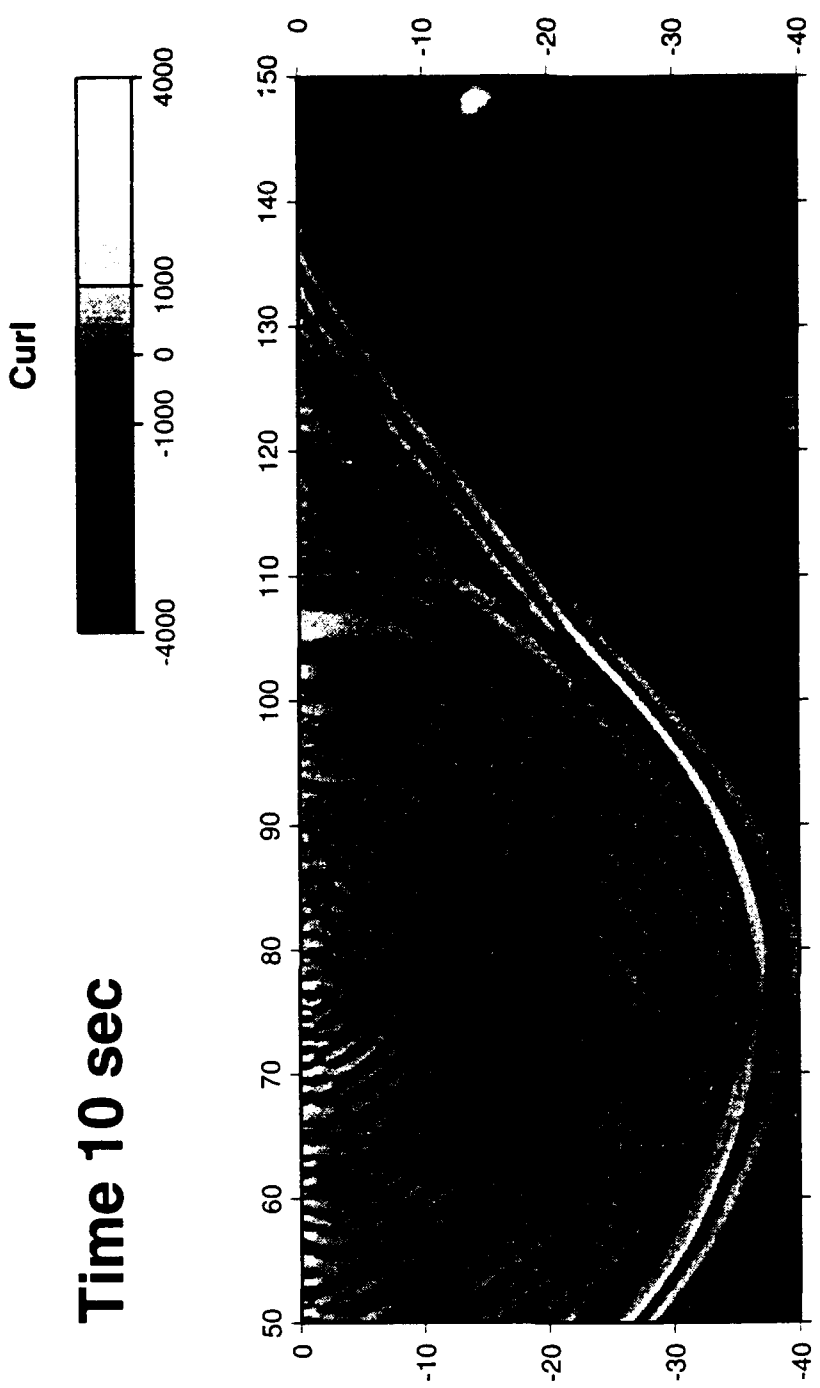


Figure 8: Snapshot of curl for the same situation as in Fig. 5.

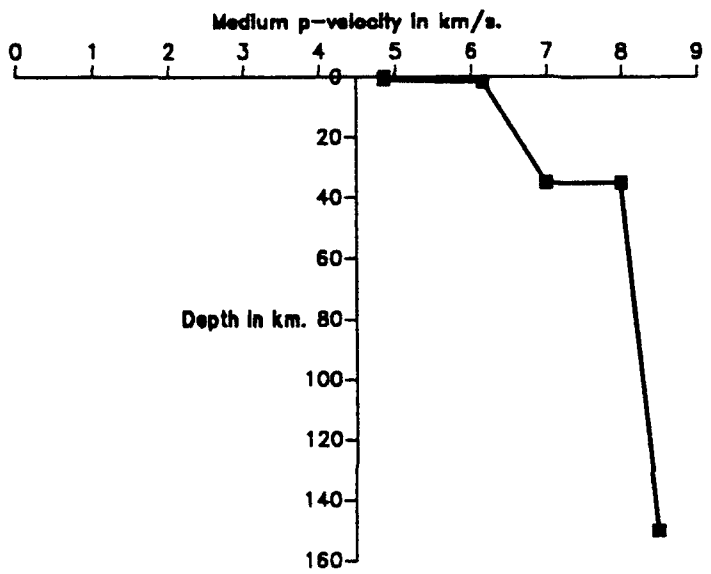


Figure 9: Medium model of pressure velocity used for the snapshots in Figs. 5 - 8.

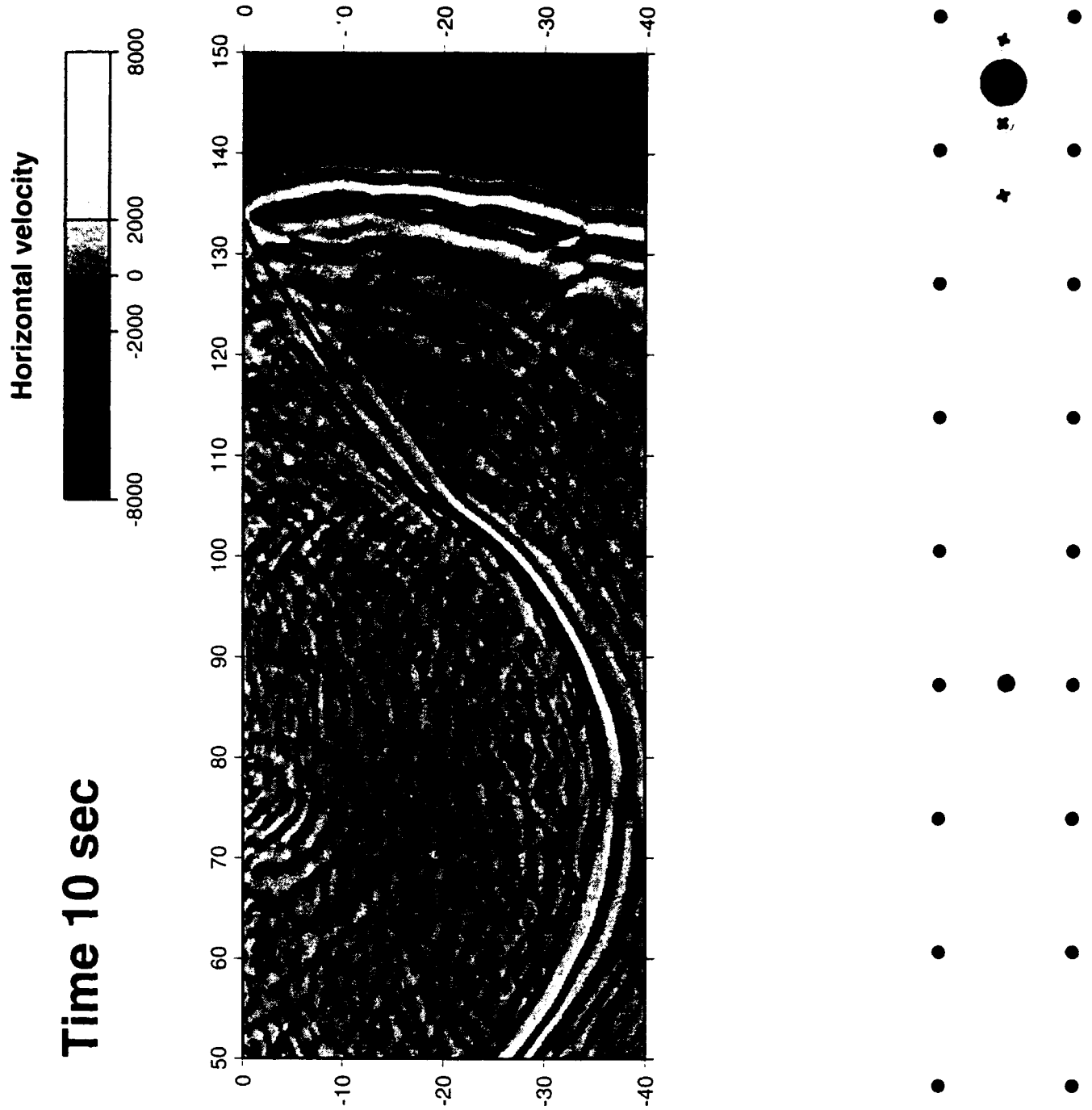


Figure 10: Snapshot of horizontal particle velocity 10 seconds after a pressure wave is initiated from a Gaussian point source with depth 2 km below the surface topography. The medium model is displayed in Fig. 14.

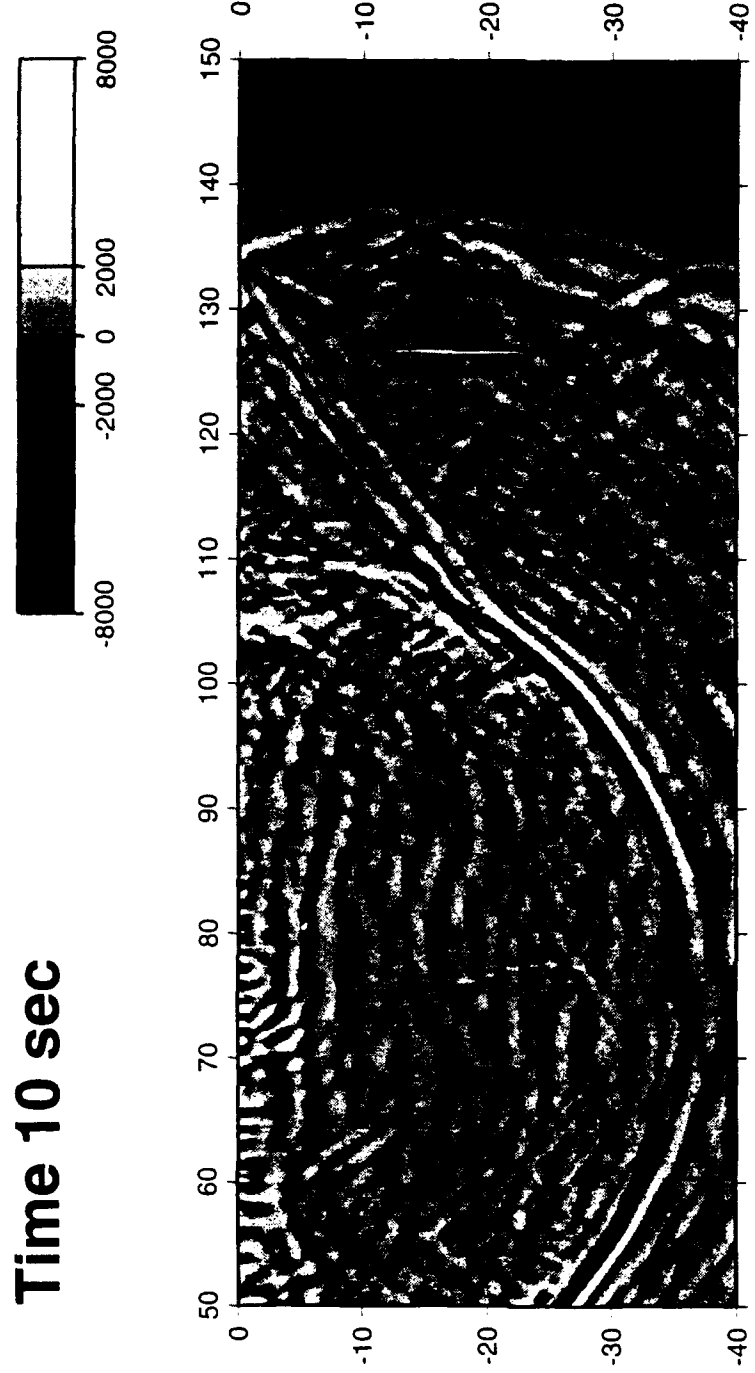


Figure 11: Snapshot of vertical particle velocity for the same situation as in Fig. 10.

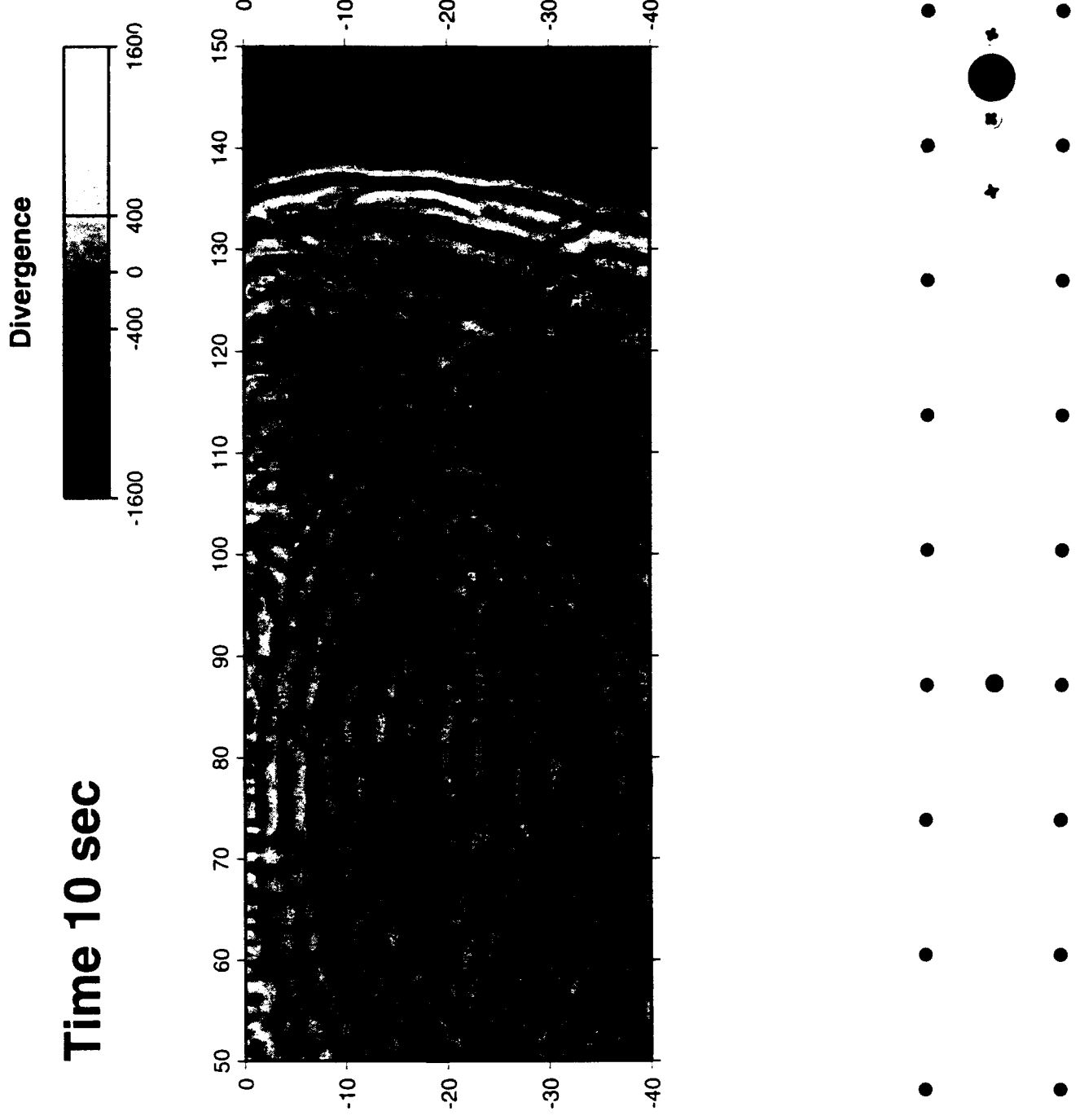


Figure 12: Snapshot of divergence for the same situation as in Fig. 10.

**Time 10 sec**

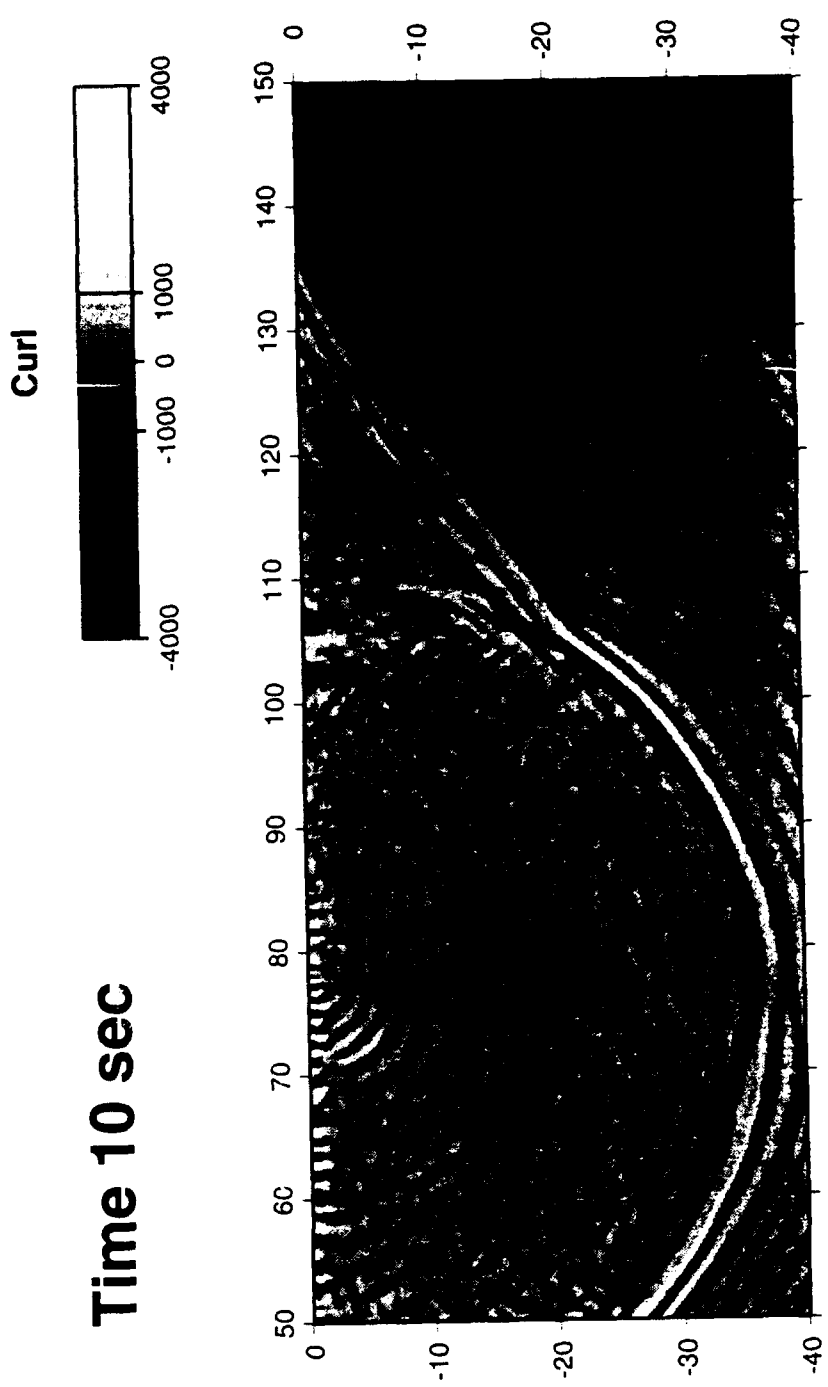


Figure 13: Snapshot of curl for the same situation as in Fig. 10.

$B = 30$

## Random model

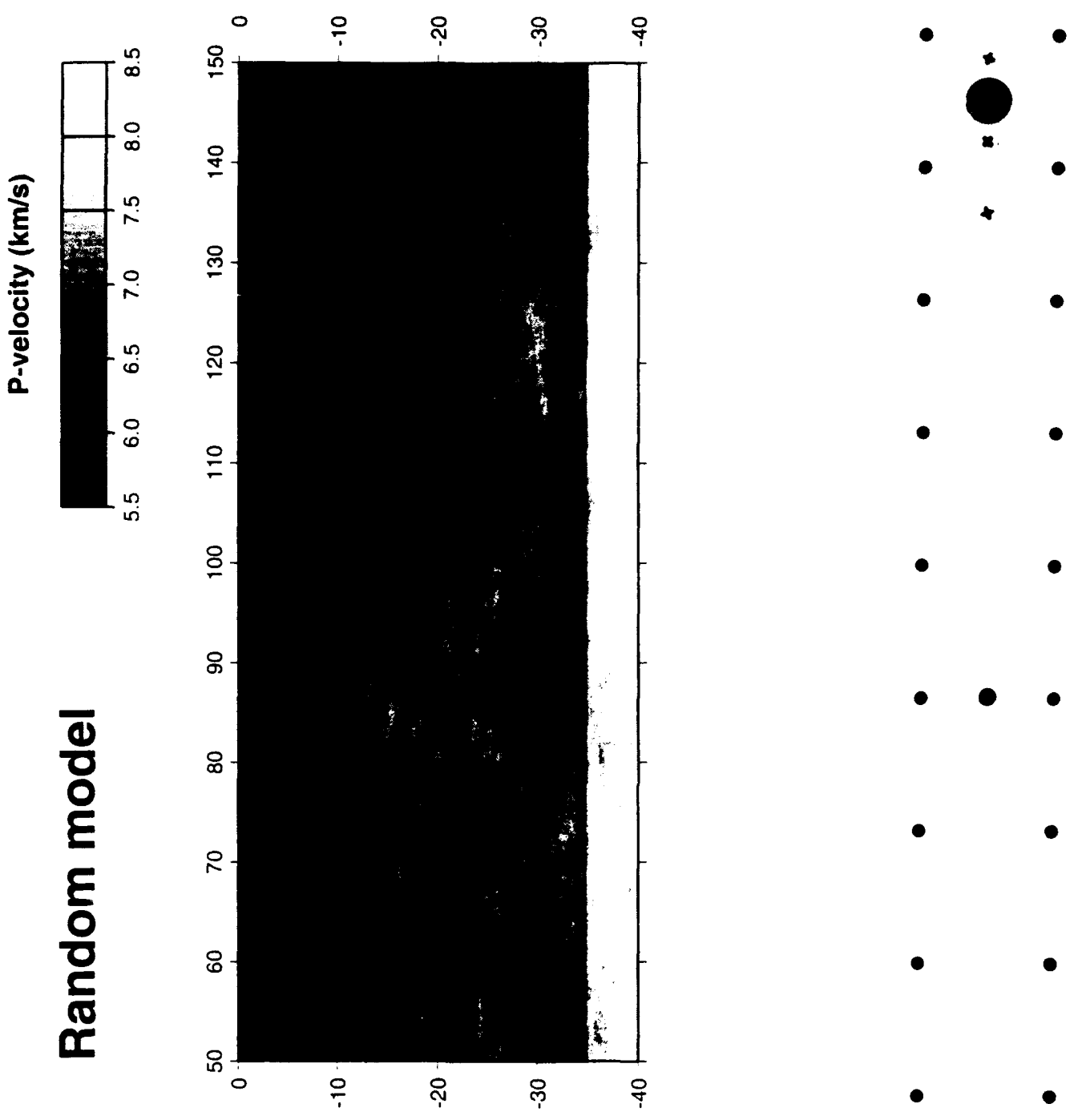


Figure 14: Random medium model of pressure velocity used for the snapshots in Figs. 10 – 13.

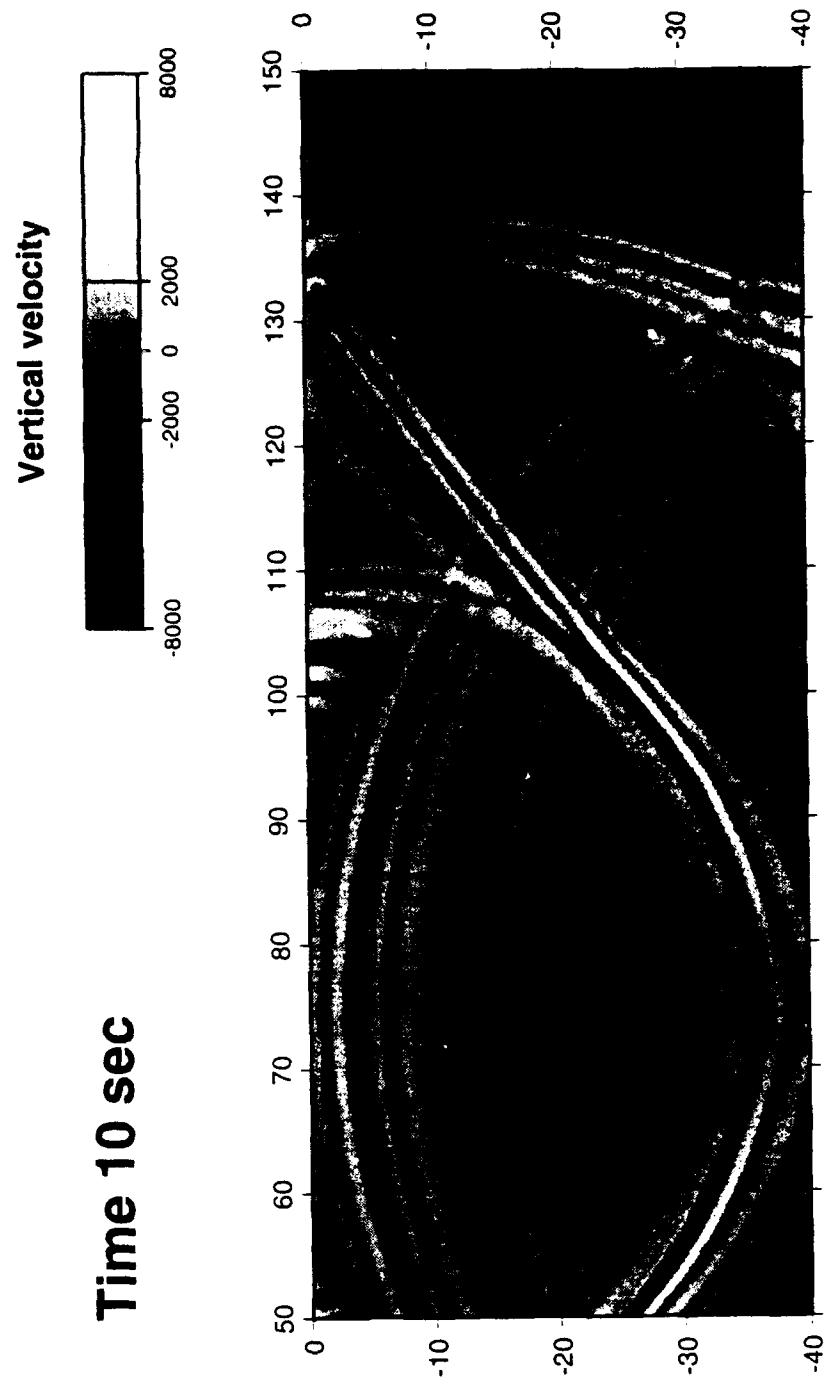


Figure 15: Snapshot of vertical particle velocity 10 seconds after a pressure wave is initiated from a Gaussian point source with depth 2 km below a plane surface. The medium model is displayed in Fig. 9.

**Time 10 sec**

**Vertical velocity**

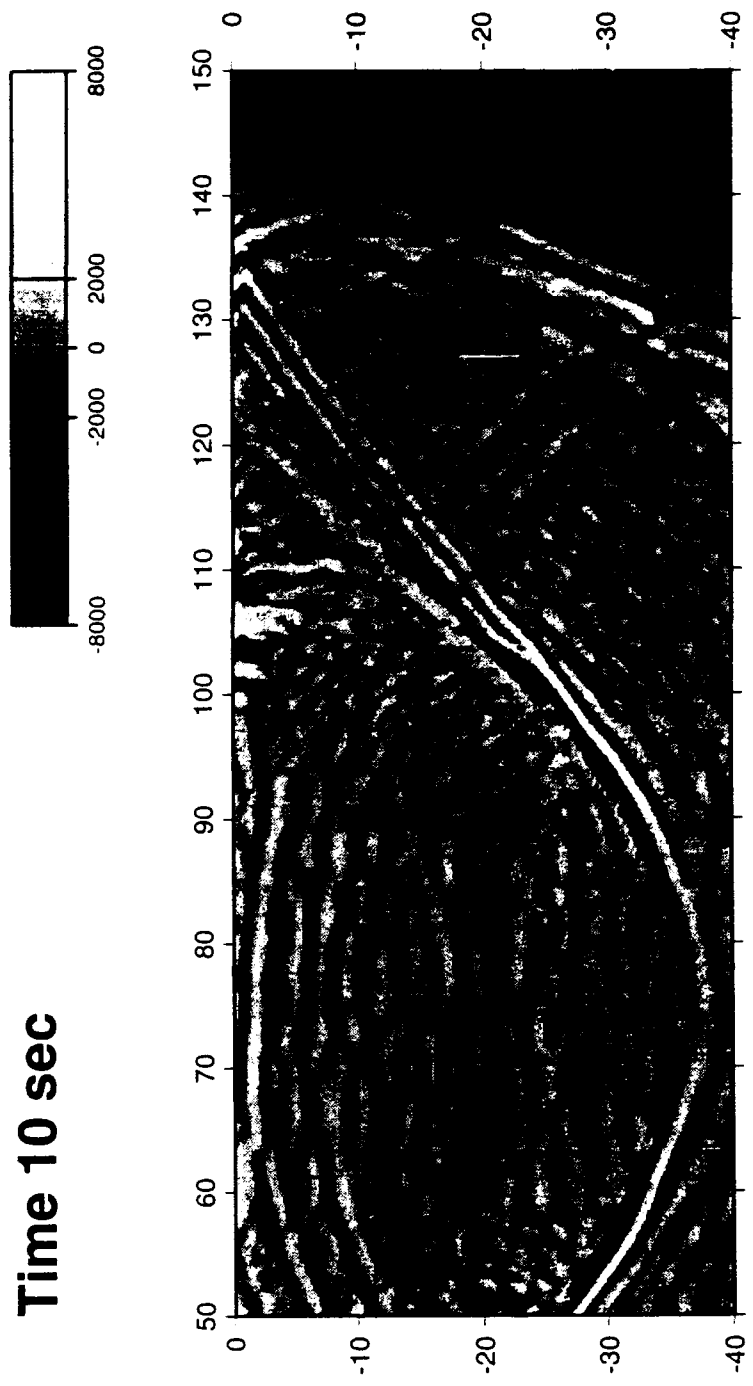


Figure 16: Same as Fig. 15, except that the medium model is now displayed in Fig. 14.

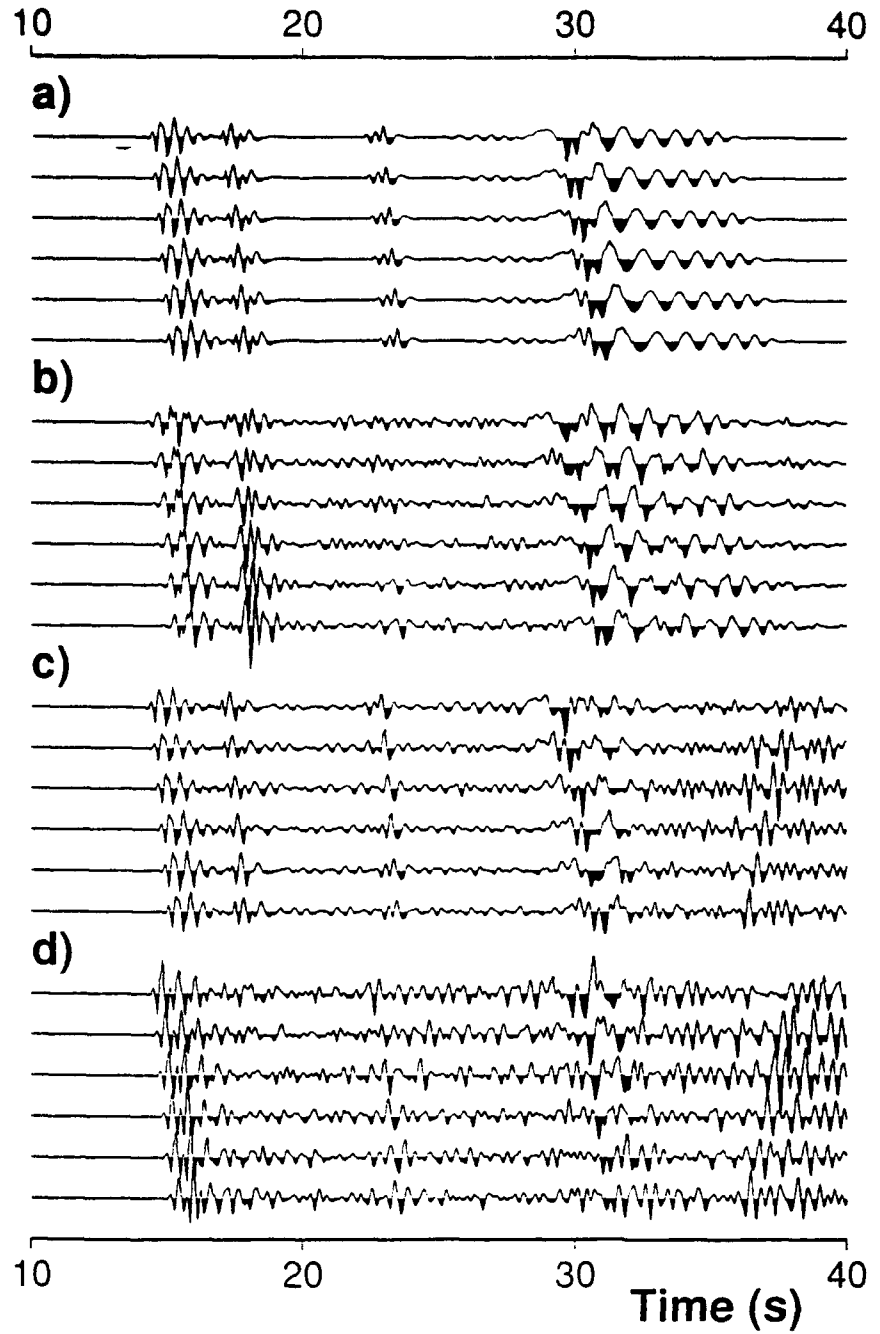


Figure 17: Seismograms for all four runs. In each section six traces with 800 m separation are given, starting at 90 km to the right of the horizontal position of the source. They display the vertical particle velocity at the free surface. The four sections represent: a) plane surface with no random velocity realization, b) plane surface with random velocity realization, c) topography surface with no random velocity realization and d) topography surface with random velocity realization.